INSTITUTO DE PESQUISAS ENERGÉTICAS E NUCLEARES

Autarquia Associada à Universidade de São Paulo

BINDER-FREE TEXTILE PAN-BASED ELECTRODES FOR AQUEOUS AND GLYCEROL-BASED ELECTROCHEMICAL SUPERCAPACITORS

INGRID ARIANI BELINELI BARBOSA

Dissertação apresentada como parte dos requisitos para obtenção do Grau de Mestre em Ciências na Área de Tecnologia Nuclear - Materiais

Orientador
Prof. Dr. Rubens Nunes de Faria Junior

São Paulo

2023

INSTITUTO DE PESQUISAS ENERGÉTICAS E NUCLEARES

Autarquia Associada à Universidade de São Paulo

BINDER-FREE TEXTILE PAN-BASED ELECTRODES FOR AQUEOUS AND GLYCEROL-BASED ELECTROCHEMICAL SUPERCAPACITORS

Versão corrigida

INGRID ARIANI BELINELI BARBOSA

Dissertação apresentada como parte dos requisitos para obtenção do Grau de Mestre em Ciências na Área de Tecnologia Nuclear - Materiais

Orientador
Prof. Dr. Rubens Nunes de Faria Junior

São Paulo

2023

Como citar:

BELINELI BARBOSA, I. A. **BINDER-FREE TEXTILE PAN-BASED ELECTRODES FOR AQUEOUS AND GLYCEROL-BASED ELECTROCHEMICAL SUPERCAPACITORS**. 2023. 135 f. Dissertação (Mestrado em Tecnologia Nuclear), Instituto de Pesquisas Energéticas e Nucleares, IPEN-CNEN, São Paulo. Disponível em: ‹http://repositorio.ipen.br/› (data de consulta no formato: dd/mm/aaaa)

Ficha catalográfica elaborada pelo Sistema de geração automática da Biblioteca IPEN, com os dados fornecidos pelo(a) autor(a).

ACKNOWLEDGEMENTS

RESUMO

BELINELI BARBOSA, I. A. **ELETRODOS À BASE DE PAN TÊXTIL SEM AGLUTINANTES PARA SUPERCAPACITORES ELETROQUÍMICOS EM ELETRÓLITOS AQUOSOS E À BASE DE GLICEROL**. 2023. 135 f. Dissertação (Mestrado em Tecnologia Nuclear), Instituto de Pesquisas Energéticas e Nucleares, IPEN-CNEN, São Paulo.

Dentre os vários tipos de dispositivos de armazenamento de energia, supercapacitores eletroquímicos têm ganhado destaque, pois, preenchem a lacuna entre os capacitores eletrolíticos e as baterias. Este trabalho aborda capacitores elétricos de dupla camada (EDLCs), um tipo de supercapacitor eletroquímico, sendo dividido em duas partes. Na primeira, foi fornecida a produção e caracterização dos eletrodos à base de feltro de fibra de carbono ativado (ACFF) derivados de fibra PAN têxtil. Na segunda, investigou-se a caracterização eletroquímica dos EDLCs em eletrólitos aquosos (ácidos e alcalinos) e em três tipos diferentes de eletrólitos à base de glicerol. Eletrodos ACFF são livres de aglutinantes e apresentam área superficial específica elevada ($1875 \ m^2 \ g^{-1}$), contendo 87% do volume total de poros como microporos (largura máxima de 3 nm) e distribuição modal de 1.2 nm. Técnicas de espectroscopia de impedância eletroquímica, voltametria cíclica e carga-descarga galvanostática foram realizadas em uma configuração simétrica de dois eletrodos à temperatura ambiente. Os resultados mostraram que os eletrodos ACFF são adequados para eletrólitos aquosos ácidos e alcalinos, bem como o eletrólito híbrido de cloreto de colina-glicerol (ChCl:GLY), em uma razão molar de 3:1. Dentre os eletrólitos aquosos, H_2SO_4 2 mol L^{-1} apresentou, em termos de potência e energia, o desempenho eletroquímico mais satisfatório, seguido por KOH 2 mol L^{-1} e H_2SO_4 1 mol L^{-1}. Entre os eletrólitos à base de glicerol, investigados neste trabalho, ChCl:GLY (3:1) tem o desempenho mais comparável aos eletrólitos aquosos. Embora a densidade de potência ainda seja baixa devido à alta resistência interna, ChCl:GLY (3:1) é resistente ao calor sendo uma alternativa promissora de eletrólito para aplicações em supercapacitores, visto que, o glicerol é um subproduto da produção de biodiesel feito por um processo de transesterificação.

Palavras-chave: Supercapacitores; EDLC; Fibra PAN têxtil; Glicerol; Cloreto de colina.

ABSTRACT

BELINELI BARBOSA, I. A. **BINDER-FREE TEXTILE PAN-BASED ELECTRODES FOR AQUEOUS AND GLYCEROL-BASED ELECTROCHEMICAL SUPERCAPACITORS**. 2023. 135 f. Dissertação (Mestrado em Tecnologia Nuclear), Instituto de Pesquisas Energéticas e Nucleares, IPEN-CNEN, São Paulo.

Amidst different types of energy storage devices, electrochemical supercapacitors have received considerable attention as they close the gap between electrolytic capacitors and batteries. This work addresses electric double-layer capacitors (EDLCs), a type of electrochemical supercapacitor, and has been divided into two parts. In the former, the production and characterization of activated carbon fiber-felt (ACFF) electrodes derived from textile PAN-based fiber have been provided. In the latter, the electrochemical characterization of EDLCs in aqueous electrolytes (acidic and alkaline) and in three types of glycerol-based electrolytes have been investigated. Binder-free ACFF electrodes have a high specific surface area of 1875 m^2 g^{-1}, containing 87% of the total volume of pores as micropores (maximum pore width of 3 nm), and a modal distribution of 1.2 nm. Electrochemical impedance spectroscopy, cyclic voltammetry, and galvanostatic charge-discharge techniques were carried out in a symmetric two-electrode setup at room temperature. The results showed that ACFF electrodes are suitable for acidic and alkaline aqueous electrolytes as well as the choline chloride-glycerol hybrid electrolyte (ChCl:GLY) at a molar ratio of 3:1. Among aqueous electrolytes, H_2SO_4 2 mol L^{-1} had the most satisfactory electrochemical performance in terms of power and energy, followed by KOH 2 mol L^{-1} and H_2SO_4 1 mol L^{-1}. Among the glycerol-based electrolytes investigated in this work, ChCl:GLY (3:1) has the most comparable performance to aqueous electrolytes. Although power density is still limited due to high internal resistance, ChCl:GLY (3:1) is heat-resistant and a promising alternative electrolyte for supercapacitors applications, especially given that glycerol is a by-product of FAME (fatty acid methyl ester) biodiesel.

Keywords: Supercapacitor; EDLC; Textile PAN-based fibers; Glycerol; Choline chloride.

LIST OF TABLES

LIST OF FIGURES

LIST OF ABBREVIATIONS, ACRONYMS, AND UNITS

Acronyms, abbreviations, and units	Description
€	Euro
Ω	Ohms
$\Omega \, cm^2$	Ohms - square centimeter
A	Ampere (the unit of electric current)
A1	Physical activation 1
A2	Physical activation 2
A3	Physical activation 3
AC	Activated carbon
ACF	Activated carbon fiber
ACFF	Activated carbon fiber-felt
ACN	Acetonitrile
$A \, g^{-1}$	Ampere per gram
Ar	Argon
ASTM	American Society for Testing and Materials
BRL	Brazilian currency or Brazilian real
C	Coulomb (the unit of electric charge)
°C	Celsius
$°C \, min^{-1}$	Celsius per minute
CAGR	Compound annual growth rate
C-C	Carbon-carbon covalent bond
$C_3H_8O_3$	Glycerol
$(C_3H_3N)_n$	Polyacrylonitrile (PAN)
$C_5H_{14}ClNO$	Choline chloride
CFF	Carbon fiber-felt
ChCl:GLY	Choline chloride-glycerol hybrid electrolyte
cm^{-1}	Reciprocal centimeter or wavenumber
cm^2	Square centimeter

cm^3	Cubic centimeter
cm^3 g^{-1}	Cubic centimeter per gram
CO$_2$	Carbon dioxide
CV	Cyclic voltammetry
DES	Deep eutectic solvent
DFT	Density functional theory
dtex	Decitex (the mass in gram per 10,000 m of fiber)
EDL	Electric double layer
EDLC	Electric double-layer capacitor
EIS	Electrochemical impedance spectroscopy
ESR	Equivalent series resistance
EPR	Equivalent parallel resistance
E$_D$	Specific energy density
F	Farad (the unit of capacitance)
F cm^{-3}	Farad per cubic centimeter
F g^{-1}	Farad per gram
F m^{-1}	Farad per meter
FAME	Fatty acid methyl ester (biodiesel)
g	Gram
g cm^{-3}	Gram per cubic centimeter
g m^{-2}	Gram per square meter
g mol^{-1}	Gram per mole
GAC	Granular activated carbon
GCD	Galvanostatic charge-discharge
h	Hour
H$^+$	Hydrogen ion
H$_2$SO$_4$	Sulfuric acid
HBA	Hydrogen bond acceptor
HBD	Hydrogen bond donor
HCl	Hydrochloric acid
Hz	Hertz (unit of frequency)

IHP	Inner Helmholtz plane
IR$_{drop}$	Voltage drop
ISO	International Organization for Standardization
IUPAC	International Union of Pure and Applied Chemistry
J	Joule
K_2CO_3	Potassium carbonate
K_2CO_3:GLY	Potassium carbonate-glycerol hybrid electrolyte
K	Kelvin (0 K = -273.15 °C)
K^+	Potassium ion
kg	Kilogram
kHz	Kilohertz
KOH	Potassium hydroxide
KOH:GLY	Potassium hydroxide-glycerol hybrid electrolyte
kV	Kilovolt
LaB6	Lanthanum hexaboride
M	Molarity (Mole per liter)
m^2	Square meter
$m^2\ g^{-1}$	Square meter per gram
MB	Methylene blue
mg	Milligram
mg cm^{-2}	Milligram per square centimeter
mg g^{-1}	Milligram per gram
min	Minute
ml	Milliliter
mm	Millimeter
mmol g^{-1}	Millimole per gram
mol L^{-1}	Mole per liter
mV	Millivolt
mV s^{-1}	Millivolt per second

mS cm^{-1}	Millisiemens per centimeter
N	Normality
N$_2$	Nitrogen gas
Na$_2$CO$_3$	Sodium carbonate
Na$_2$SO$_4$	Sodium sulfate
NaHCO$_3$	Sodium bicarbonate
NaOH	Sodium hydroxide
NaOEt	Sodium ethoxide
nm	Nanometer
nm^2	Square nanometer
O$_2$	Oxygen gas
OH	Hydroxyl group
OH$^-$	Hydroxide ion
OHP	Outer Helmholtz plane
OPFF	Oxidized textile-Pan fiber-felt
PAC	Powder activated carbon
Pa.s	Pascal-second (the unit of viscosity)
PAN	Polyacrylonitrile
PC	Propylene carbonate
pK$_a$	Negative logarithm of K$_a$ (acid dissociation constant)
pH	Potential hydrogen
P$_D$	Specific power density
P/P$_o$	Relative pressure
PZC	Point of zero charge
r	Correlation coefficient
R$_{ct}$	Charge-transfer resistance
Redox	Oxidation-reduction reaction
R$_e$	Bulk electrolyte resistance
RT	Room temperature
s	Second
sccm	Standard cubic centimeters per unit (flow rate of a fluid)

S cm^{-2}	Siemens per square centimeter
Scm^2 mol^{-1}	Siemens square centimeter per mole
SC	Supercapacitor
SE	Secondary electron
SEM	Scanning electron microscopy
sp^2	one s and two p atomic orbitals
SSA	Specific surface area
S$_{BET}$	Specific surface area (Brunauer, Emmett and Teller)
SO$_4^{-2}$	Sulfate ion
TEABF$_4$	Tetraethylammonium tetrafluoroborate
µm	Micron
µmHg	Micron of Mercury
USD	United States dollar
V	Volt (the unit of electrical potential difference)
VA	Volt-ampere
V s^{-1}	Volt per second
W	Watts
w/w	Weight by weight
W Kg^{-1}	Watts per kilogram
Wh Kg^{-1}	Watt-hour per kilogram
XRD	X-ray diffraction
XPS	X-ray photoelectron spectroscopy
Z$_{im}$	The imaginary part of Z
Z$_{re}$	The real part of Z

TABLE OF CONTENTS

1. INTRODUCTION

Due to the growing demand for energy consumption and the development of new energy sources, energy storage devices are needed for balancing the energy supply and demand on the electrical grid system. Among the different types of energy storage devices, electrochemical supercapacitors (SCs), also known as ultracapacitors, have drawn a lot of attention as they bridge the gap between electrolytic capacitors and batteries. SCs have high energy densities and can store more energy than electrostatic capacitors. In addition, SCs have high power densities and can store and release energy faster than batteries [1]. Other advantages of SCs include a long-life cycle (> 100,000 cycles), fast charge-discharge rates (from seconds to minutes), low maintenance, lightweight, and safe operations [2]. Due to its high self-discharge rate, SCs are not fitting for long-term energy storage [3]. In comparison to batteries, SCs have lower-energy storage capacity and are not well-suited for applications requiring high energy density [4]. Therefore, SCs can be used as a complement to other energy storage devices, such as batteries for electric vehicles, or for those applications requiring a lot of power in short bursts [5].

At an annual growth rate of 14.1%, the global market size for supercapacitors (SCs) is expected to reach USD 912 million (approximately BRL 5 billion) by 2027 [6]. Moreover, EDLC (electric double-layer capacitor), which is a type of electrochemical supercapacitor, accounted for over 65% of the market share in 2020 and is expected to increase by 14.5% in 2027 [7].

Electrodes and electrolytes are at the core of SCs research. Most research topics focus on electrode materials, with just a few types of research focusing on the study of electrolytes [8]. The electrochemical performance of electrodes depends on variables such as specific surface area (SSA), surface functional groups, pore size and pore distribution [9]. Due to high SSA, within a range of 500 - 2500 m^2 g^{-1}, activated carbons (ACs) are common examples of carbon-based electrodes for EDLCs [10]. Examples of ACs include granular activated carbon (GAC) and powder activated carbon (PAC). In AC-based electrodes, binders are utilized to provide strong adhesion between the electrode and the current collector. These binders cause pore blockage reducing the active surface area of the electrode and increasing resistance which impacts the electrochemical performance of the supercapacitor [11]. Among the different types of activated materials, activated carbon fibers (ACFs) can be converted into any fabric offering them self-supporting

characteristics [12]. ACF-based electrodes, which are binder-free electrodes, have drawn attention not only because of high SSA (mostly micropores), but also due to a well-defined porous structure, and high adsorption capacity [13]. An example of a synthetic precursor used to produce ACFs is Polyacrylonitrile (PAN); a thermoplastic polymer with a high melting point of 350°C [14]. Textile PAN-based fibers are low-cost and alternative raw materials used to produce ACFs. In order to obtain self-supporting characteristics, textile PAN-based fibers are converted into a felt [15].

Electrolytes for SCs should be relatively safe, non-toxic, environmentally friendly, and affordable, with low volatility and low flammability, high ionic conductivity, low internal resistance, wide operating temperature range and wide electrochemical stability window [16]. Carbon-based electrodes in organic electrolytes, which use acetonitrile (ACN) or propylene carbonate (PC) as solvents, are commonly used for commercial supercapacitors [17]. Although organic-based electrolytes can support a large potential window (~ 3 V), they are usually flammable and toxic [18]. Aqueous electrolytes are an alternative to organic-based electrolytes due to their advantages of high ionic conductivity (10^1 - 10^2 mS cm^{-1}), non-flammability, low cost, low internal resistance, and low viscosity [19]. One of the drawbacks of aqueous electrolytes is the limited cell voltage (~ 1 V) due to the narrow electrochemical stability window (~1.23 V). The development of alternative electrolytes focuses on increasing the potential window, also known as operating voltage, and consequently the energy density of the devices [20]. As the electrochemical performance of supercapacitors strongly relies on the electrode-electrolyte interaction, correlating the size of electrolyte ions and the pore size of carbon-based electrodes is necessary.

This work addresses electric double-layer capacitors (EDLCs), a type of energy storage device, and it has been divided into two parts, as follows:

    I.   Production and characterization of binder-free electrodes from textile PAN-based fiber.

    II.   Electrochemical characterization of the electrodes in aqueous (acidic and alkaline) and in three types of glycerol-based electrolytes.

2. AIM AND OBJECTIVES

2.1. Aim

Produce and characterize binder-free electrodes derived from textile PAN-based fiber to correlate the electrode-electrolyte interface of aqueous-based and glycerol-based EDLC devices.

2.2. Objectives

- Produce binder-free electrodes by means of oxidation, carbonization, and physical activation with three different parameters.
- Select the most relevant physical activation parameter.
- Characterize the electrodes through physical-chemical and textural characterizations.
- Elaborate room temperature (RT) setup and assemble EDLC cells.
- Characterize EDLC cells via electrochemical characterizations, such as cyclic voltammetry, electrochemical impedance spectroscopy, and galvanostatic charge-discharge techniques.
- Correlate the electrode-electrolyte interface of aqueous and glycerol-based EDLCs.
- Obtain a Ragone plot.
- Determine which aqueous and glycerol-based electrolytes are suitable for the electrode produced as part of this work.

3. LITERATURE REVIEW

Capacitors, supercapacitors, batteries, and fuel cells are examples of energy storage devices. As can be seen in Figure 1, a Ragone plot is used to compare the performance of these energy storage devices. The data is plotted as energy density (specific energy density) versus power density (specific power density). Owing to their characteristics, SCs bridge the gap between electrolytic capacitors and batteries. Energy density indicates how much energy can be stored in a device, whereas power density refers to how quickly this energy can be delivered. SCs have relatively high-power densities, but low-energy densities when compared to batteries or fuel cells. Several factors can influence the energy density and the power density of supercapacitors (Figures 2 and 3), and this section provides a brief explanation of the fundamentals of supercapacitors.

Figure 1 - Ragone plot for different energy storage devices
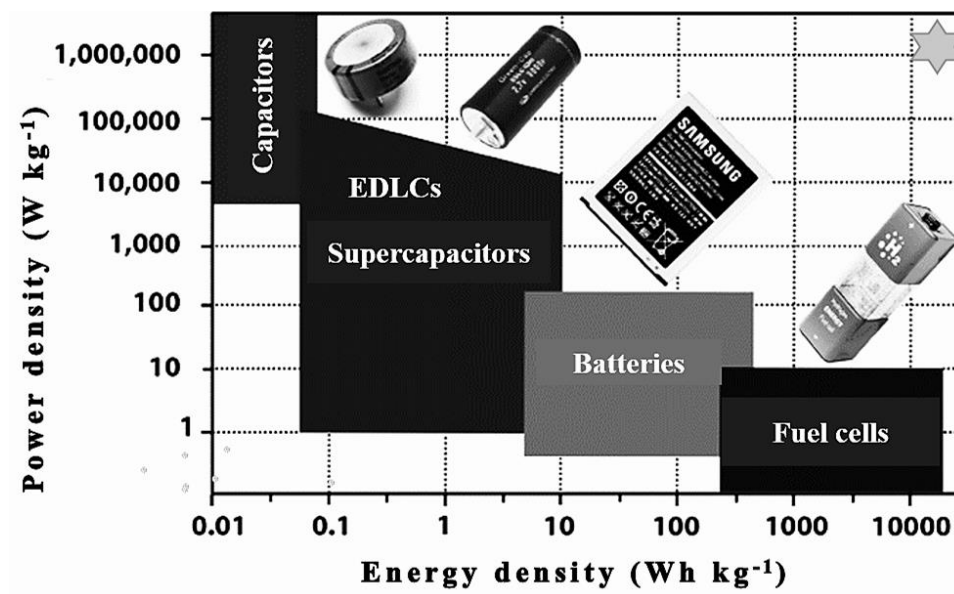
Source: Abhijith, P. P. et al. (2023) [21]

Figure 2 – Factors that impact the energy density of supercapacitors
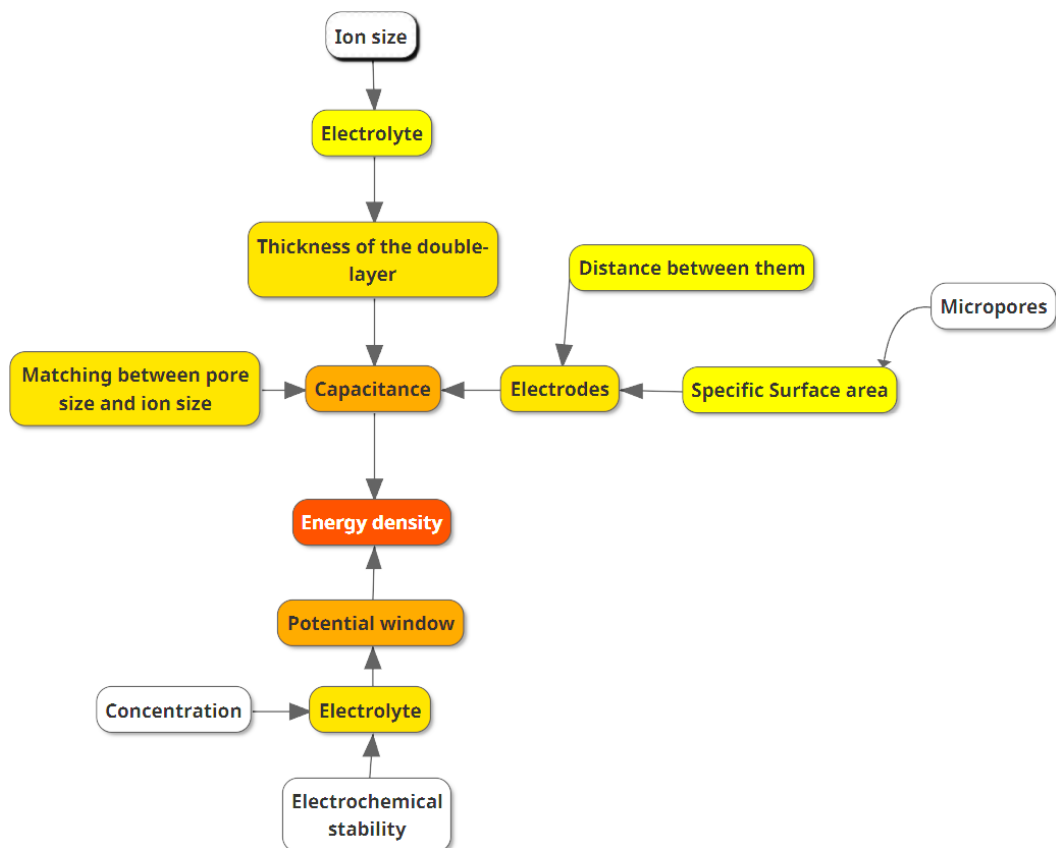
Source: author. Based on the data obtained from multiple sources [22,23,24,25,26,27]

Figure 3 - Factors that impact the power density of supercapacitors
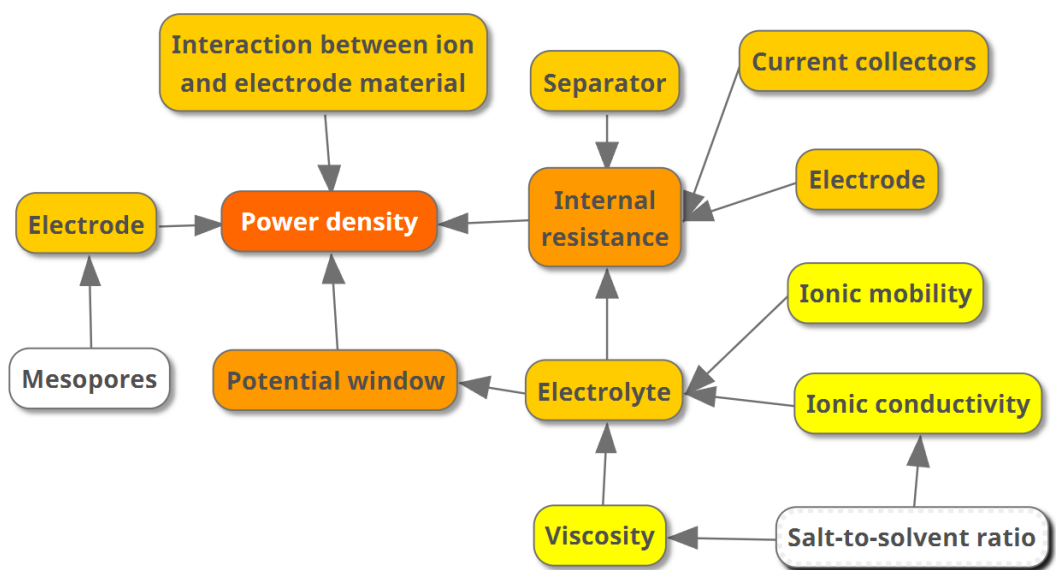
Source: author. Based on the data obtained from multiple sources [22,23,24,25,26,27]

3.1. Supercapacitors

A supercapacitor consists of two electrodes (symmetric or asymmetric) in contact with an aqueous or a non-aqueous electrolyte, as well as an ion-permeable separator that isolates the two electrodes and prevents a short circuit (Figure 4a) [28]. Based on the charge storage mechanism (faradaic and non-faradaic), supercapacitors are classified into three categories, namely electric double-layer capacitors (EDLCs), pseudocapacitors, and hybrid supercapacitors [29,23]. EDLCs store charge non-faradaically or electrostatically; a physical process. Therefore, no charge transfer (redox reaction) takes place across the electrode-electrolyte interface [30,31]. Pseudocapacitors store charge faradaically through fast and reversible redox reactions at the surface or near-surface of the electrode. Thus, there is a transfer of charges at the electrode-electrolyte interface due to a chemical process [32,31]. Hybrid supercapacitors are based on two different mechanisms of charge storage: faradaic e non-faradaic. The negative electrode material, commonly a carbon-based electrode, is responsible for the power source and it stores charge non-faradaically. Otherwise, the positive electrode material, commonly a metal oxide electrode, is responsible for the energy source and it stores charge faradaically [33,31].

3.1.1. Electric double-layer capacitors (EDLCs)

The basic principles of EDLCs are analogous to those of conventional capacitors. EDLCs store electrical charge in an electric double layer (EDL) at the electrode/electrolyte interface (Figure 4b) [23]. Since the charge storage mechanism is non-faradaic, electrical charge is stored through physical adsorption-desorption of charged electrolyte ions at the surface of porous carbon-based electrodes [30]. When voltage is applied between the electrodes, there is a build-up of charge on the electrode surface. Due to the difference in potential, opposite charges are attracted. As a result, the ions of the electrolyte diffuse over the separator and on the pores of the opposite-charged electrode to form an electric double layer that consists of the compact layer and the diffuse layer. Upon application of load, the ions return to the electrolyte [34].

Figure 4 - (a) Schematic of an electrochemical double-layer capacitor (EDLC), and (b) Electrode-electrolyte interface in EDLCs

(a)   (b)
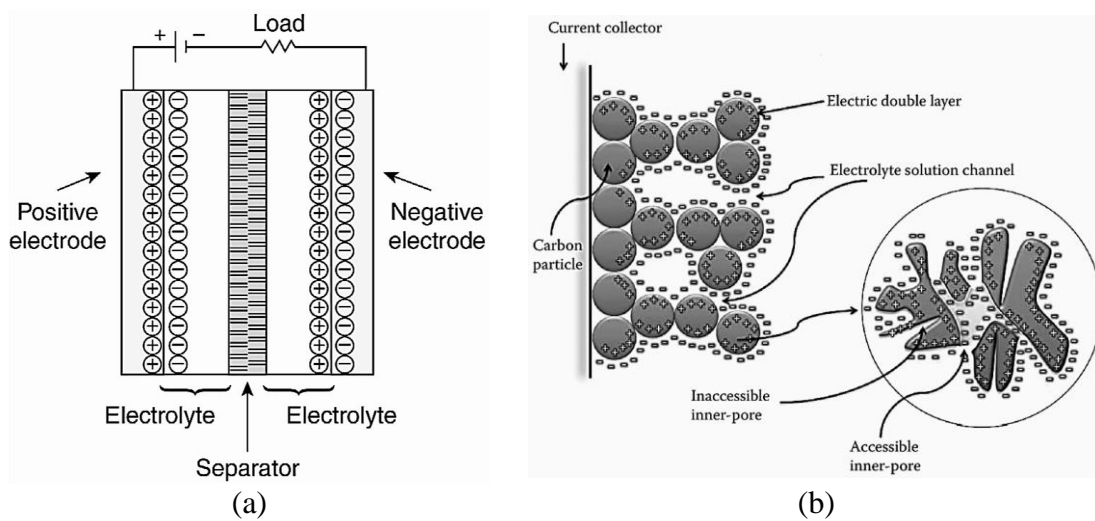
Source: (a) Scibioh, M. A. et al. (2023) [35] and (b) Aiping Y. et al. (2013) [36]

The concept of the EDL is based on the theories and models proposed by Helmholtz, Gouy-Chapman, and Stern. The Stern model of the EDL combines the concept of the earlier models proposed by Helmholtz and Gouy-Chapman (Figure 5). In the inner layer, also known as the Stern layer or the compact layer, ions are strongly adsorbed by the surface of the electrode. The compact layer is divided into the inner Helmholtz plane (IHP) and the outer Helmholtz plane (OHP). IHP refers to the distance from the surface to the center of specifically adsorbed ions whereas the OHP refers to non-specifically adsorbed counterions. In the outer layer, or the diffuse layer, ions are distributed through the bulk solution (Figure 6) [37,38,39].

Figure 5 - The Helmholtz and the Gouy-Chapman models of the electric double layer (EDL)
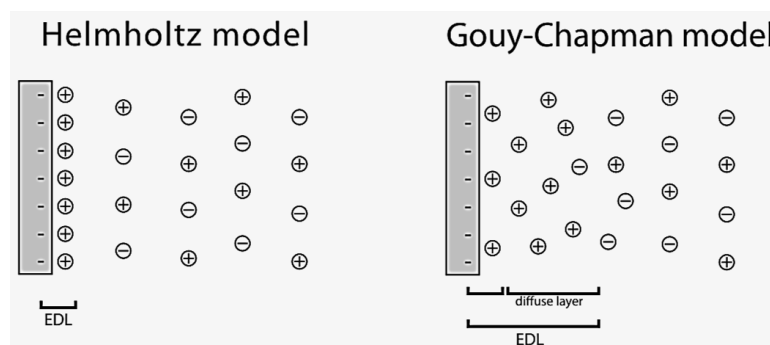
Source: Oberklein, D. (2012) [39]

Figure 6 – The Stern model of the electric double layer (EDL)
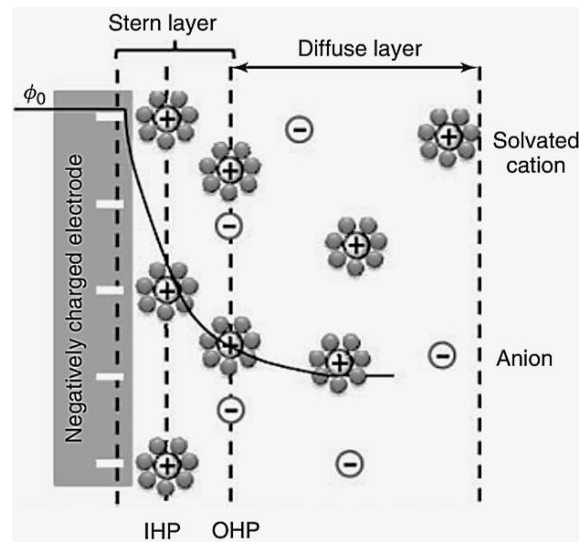
Source: Simon, P. et al. (2013) [40]

3.1.2. Electrochemical performance and materials for electric double-layer capacitors (EDLCs)

In a conventional capacitor, capacitance (C), which is the ability to store electric charge per volt, is directly proportional to the surface area of the electrodes and inversely proportional to the distance between them (Equation 1). As can be seen in Equation 2, the energy (E) stored in a capacitor is directly proportional to its capacitance. Thus, electrode materials with high specific surface area (particularly micropores) result in increased capacitance and, consequently, high energy density [24,23,41].

$$C = \frac{Q}{V} = \frac{\varepsilon_0 \varepsilon_r A}{d}$$

C = Capacitance (F)

Q = Electric charge (C)

V = Potential difference (V)

ε_0 = Vacuum permittivity (8.8 10^{-12} F m^{-1})

ε_r = Electrolyte relative permittivity (unitless)

A = Surface area of each electrode (m^2)

d = Distance between the electrodes (m)

(1)

$$E = \frac{1}{2}CV^2$$

E = Energy (J)

C = Capacitance (F)   (2)

V = Potential difference (V)

Due to their cost effectivity, porous structure, and high surface area, activated carbons (ACs) are common materials used for the fabrication of electrodes [23,42]. Examples of ACs include granular activated carbon (GAC), with particle sizes ranging from 0.5 mm to 4 mm, and powder activated carbon (PAC), with particle sizes ranging from 1 μm to 150 μm [13]. ACs employed as electrodes for EDLCs are mostly derived from biomass waste through physical activation process or chemical activation process [42]. Physical activation is carried out under high temperatures (700 – 1200° C) with oxidizing agents such as O_2 (oxygen), CO_2 (carbon dioxide), and steam. Chemical activation is performed at 400 – 700° C with activating agents such as NaOH and KOH [42]. Activation is the key process in the production of carbon-based electrodes due to the development of porosity which enhances both surface area and adsorption capacity [43]. Pore size can impact both energy density (smaller pore sizes) and power density (larger pore sizes). Therefore, when designing electrode materials for EDLCs, it is critical to control the pore size during the activation process [23,26,44].

Energy density is not only proportional to capacitance but also to the square voltage of the cell (Equation 2). Hence, increasing the potential window of the electrolyte enhances the energy density of EDLCs and expands their range of applications. The performance of an EDLC can be altered depending on the choice of the electrolyte [23]. Electrolytes, which provide ionic conductivity in a cell, are commonly classified as aqueous and non-aqueous. The most common aqueous electrolytes are solutions of sulfuric acid, potassium hydroxide, and sodium sulfate, and they are categorized as acidic, basic, and neutral, respectively [45]. Although aqueous electrolytes have high ionic conductivity, they are not interesting commercially due to their small electrochemical stability window which is intrinsically narrow (1.23 V) [42,45]. Due to a wide potential window (2.5 - 2.8 V), organic electrolytes, which are non-aqueous electrolytes, lead the commercial market [42,40]. Organic electrolytes used in EDLCs consist of a conductive salt like tetraethylammonium tetrafluoroborate (TEABF$_4$) dissolved in propylene carbonate (PC) or acetonitrile (ACN) solvents [46,42]. Flammability, toxicity, volatility,

and low conductivity are the drawbacks of organic electrolytes [42]. Ionic liquids and deep eutectic solvents (DES) are alternative and nonflammable electrolytes for EDLCs that provide a wide operating voltage range, as well as thermal and chemical stability [42]. The properties of DES, a class of green electrolytes, are analogous to ionic liquids. However, the synthesis of DES is more simplified and less costly as it occurs at conditions close to room temperature [47,48]. DES are mostly biodegradable, nontoxic, non-inflammable, and nonvolatile [47,48,49]. Moreover, DES are simple mixtures composed of a hydrogen bond acceptor (HBA), such as a salt, and a suitable hydrogen bond donor (HBD) [50,48]. Choline chloride ($C_5H_{14}CINO$), a quaternary ammonium salt, and potassium carbonate (K_2CO_3), a basic salt, are examples of HBA, whereas alcohols, carboxylic acids, amine, esters, and ethers are examples of HBD [51] [52] [53,49]. Most research aims not only to increase energy density but also to enhance the temperature range of supercapacitors in which batteries cannot work [41]. Previous studies [54,55,56] synthesized DES-based electrolytes that can withstand temperatures ranging from -40 °C to 115 °C, -40 °C to 80 °C, and -20 °C to 100 °C, respectively.

The electrochemical stability window of the electrolyte, which corresponds to the cell voltage of the device, is also an important variable in determining the maximum power (P_{max}). As can be seen in Equation 3, the maximum power of a capacitor is directly proportional to the square of voltage of the cell. Hence, increasing the potential window of the electrolyte enhances power density [40,25].

$$P_{max} = \frac{V^2}{4ESR}$$
P_{max}= Maximum power (W)
V= Maximum cell voltage (V)   (3)
ESR= Equivalent series resistance (Ω)

The power performance of a device is also limited by the equivalent series resistance (ESR) [23]. ESR, also known as internal resistance, consists of the bulk solution resistance of the electrolyte, the electrode-electrolyte interfacial resistance, the resistance of intra-particle pores, and the resistance of the internal components of the cell, such as the separator and the contact resistance between the current collector and the electrode [57,27,58]. For better electrochemical performance, low ESR is desired. Electrolytes with high ionic conductivity result in low ESR and, consequently, high-power density [45].

3.2. PAN (Polyacrylonitrile) fiber

Among numerous carbonaceous materials, activated carbons (ACs) are widely employed as electrode materials for EDLCs due to high electrical conductivity, high surface area, and low cost [10,59]. AC-based electrodes usually require binders to provide strong adhesion between the electrode and the current collector. These binders cause pore blockage reducing the active surface area of the electrode and increasing resistance, which is a drawback [11]. Textile materials, which are low-cost materials, can be used as precursors to produce ACs [13]. Among ACs, activated carbon fibers (ACFs), can be converted into fabrics such as woven (yarn interlacing process), knit fabrics (yarn inter-looping process), or felt (matted non-woven fabric) which offer them self-supporting characteristics [12]. Due to their self-supporting characteristics, ACF-based electrodes are generally flexible and binder-free. Polyacrylonitrile (PAN), a thermoplastic polymer with the formula $(C_3H_3N)_n$, is a synthetic precursor used to produce activated carbon fibers (Figure 7) [14,44]. PAN precursor fibers cost around $7 - $8 per kilogram, whereas textile PAN-based precursor fibers cost approximately $2 - $3 per kilogram [60].

The application of textile PAN-based fibers as electrodes for supercapacitors in aqueous electrolytes was reported in previous studies [61,62]. In the former, a volumetric capacitance of 104 $F\,cm^{-3}$ in H_2SO_4 2 mol L^{-1} was found. In the latter, electrodes decorated with silver particles exhibited gravimetric capacitance of 169 F g^{-1} in KOH 6 mol L^{-1}, and 138 F g^{-1} in H_2SO_4 2 mol L^{-1}. Another study about textile PAN-based fiber electrodes, with enhanced surface functional groups, reported a gravimetric capacitance of 230 F g^{-1} in H_2SO_4 2 mol L^{-1} (three-electrode setup) [63]. A high gravimetric capacitance of 302 F g^{-1} in H_2SO_4 2 mol L^{-1} (two-electrode setup) was reported in a previous study about a binary composite based on polypyrrole and textile PAN-based fiber electrodes [64]. A high gravimetric capacitance of 275 F g^{-1} in H_2SO_4 4 mol L^{-1} (three-electrode setup) was reported in a previous study about carbon powder derived from pulverized PAN-based carbon fibers [65]. In all previous studies, only aqueous electrolytes were investigated.

Figure 7 – Molecular structure of polyacrylonitrile (PAN)
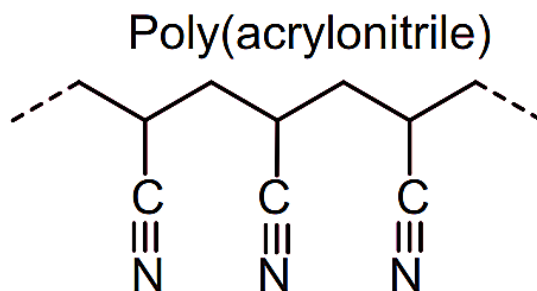
Source: Frank, E. et al. (2017) [66]

3.3. Sulfuric acid

Due to high ionic conductivity (0.8 S cm^{-2} for 1 M H_2SO_4 at 25°C) [67,42], several studies [43,61,64,63,65,68,69,70] investigated the use of sulfuric acid (H_2SO_4) as an acidic aqueous electrolyte for supercapacitors applications. A summary of the properties of the compound can be seen in Table 1, whereas the properties of hydrogen ion and sulfate ion can be seen in Table 2.

Table 1 - Properties of sulfuric acid (H_2SO_4)

Chemical Class	Inorganic acids
Molecular formula	H_2SO_4
Molecular weight (g mol^{-1})	98.08
Hydrogen bond donor count	2
Hydrogen bond acceptor count	4
Physical description	Colorless oily liquid
Boiling point (°C)	315 - 338
Melting point (°C)	10.35
Specific gravity (g cm^{-3})	1.84
Dissociation in water	$H_2SO_{4(aq)} \rightarrow H^+_{(aq)} + HSO^-_{4(aq)}$
	$HSO^-_{4(aq)} \rightarrow H^+_{(aq)} + SO^{2-}_{4(aq)}$
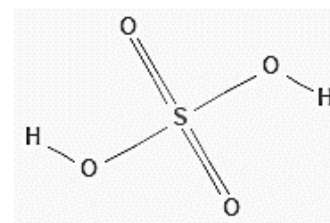
Source: author. Based on the data obtained from multiple sources [71,72]

Table 2 - Properties of hydrogen ion (H^+) and sulfate ion (SO_4^{2-})
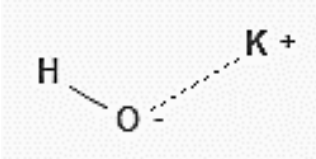
Ion	Ionic Conductivity (Scm^2 mol^{-1})	Bare ion size (nm)	Hydrated ion size (nm)
Hydrogen ion (H^+)	350	0.115	0.280
Sulfate ion (SO_4^{2-})	160	0.290	0.379

Source: author. Based on the data obtained from multiple sources [43,67].

3.4. Potassium hydroxide

Due to high ionic conductivity (0.6 S cm^{-2} for 6 M KOH at 25°C) [67], several studies [43,69,62,73,74,75,76,62,77,70] reported the use of potassium hydroxide (KOH), also known as caustic potash, as an alkaline aqueous electrolyte for supercapacitors applications. A summary of the properties of the compound can be seen in Table 3, whereas the properties of potassium ion and hydroxide ion can be seen in Table 4.

Table 3 - Properties of potassium hydroxide (KOH)

Chemical Class	Bases
Molecular formula	KOH
Molecular weight (g mol^{-1})	56.106
Hydrogen bond donor count	1
Hydrogen bond acceptor count	1
Physical description	Hygroscopic white solid
Boiling point (°C)	1327
Melting point (°C)	380 - 406
pH	13.5
Specific gravity (g cm^{-3})	2.04
Dissociation in water	$KOH_{(aq)} \rightarrow K^+_{(aq)} + OH^-_{(aq)}$

Source: author. Based on the data obtained from multiple sources [78,79]

Table 4 - Properties of potassium ion (K^+) and hydroxide ion (OH^-)

Ion	Ionic Conductivity ($Scm^2 mol^{-1}$)	Bare ion size (nm)	Hydrated ion size (nm)
Potassium ion (K^+)	74	0.133	0.331
Hydroxide ion (OH^-)	198	0.176	0.300

Source: author. Based on the data obtained from multiple sources [43,67].

3.5. Glycerol

Glycerol, commonly called glycerin, is the main byproduct of a transesterification reaction (Figure 8) used to produce a biodiesel fuel called FAME (fatty acid methyl ester) [80]. Accounting for 60% of the global glycerol market, FAME biodiesel is the major source of glycerol. It is estimated that 1 kg of crude glycerol is produced per 10 kg of biodiesel produced. Moreover, at a CAGR (compound annual growth rate) of 6.1%, the global glycerol market is expected to reach €2.92 billion by 2026 [81].

Figure 8 - Transesterification reaction of a triglyceride with methanol
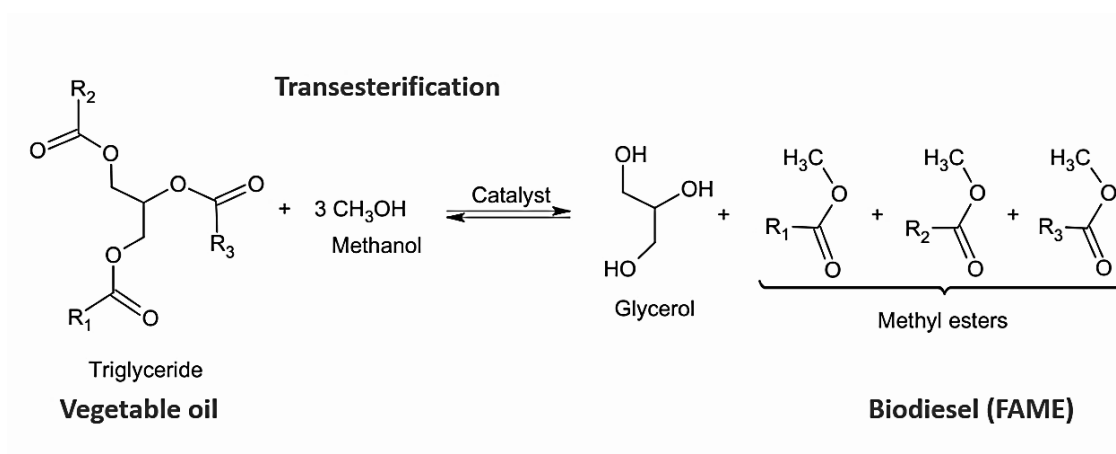
Source: Adapted from Pagliaro, M. (2017) [80].

Glycerol is an odorless, colorless, nontoxic, and nonirritating liquid with high viscosity (1.5 Pa.s), a high boiling point of 290 °C, a low melting point of 18 °C, and a specific gravity of 1.26 g cm^{-3} at 20° C (Table 5). Glycerol monomer has a hydroxyl-rich

structure with three hydroxyl functional groups (alcohol group), also known as trihydric alcohol. Due to its hydroxyl-rich structure, glycerol is highly hygroscopic and miscible in water [80]. Moreover, the degradation of glycerol can provide a variety of compounds [82,83]: dihydroxyacetone (oxidation), acrolein (dehydration), 1,2-propanediol (hydrogenolysis), H_2 + CO (reforming), acetaldehyde, acrolein, and allyl alcohol (hydrothermal process), and 1,3-propanediol (dismutation).

Table 5 - Properties of glycerol ($C_3H_8O_3$)

Chemical class	Alcohols and polyols	
Molecular formula	$C_3H_8O_3$ or $C_3H_5(OH)_3$	
Molecular weight (g mol^{-1})	92.09	
Hydrogen bond donor count	3	
Hydrogen bond acceptor count	3	
Physical description	Hygroscopic viscous colorless liquid.	
Boiling point (°C)	290	
Melting point (°C)	18.2	
Viscosity (Pa.s)	1.5	
Specific gravity (g cm^{-3})	1.26 at 20° C	
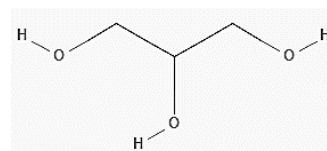
Source: author. Based on the data obtained from multiple sources [84,53,48,80]

Previous studies [47,48,49,85,86] proposed the use of glycerol as a hydrogen bond donor in deep eutectic solvents (DES), although they were not focused on supercapacitors. Glycerol was also investigated as a green solvent for organic synthesis [87,88]. Early studies on EDLCs [10,89] reported the use of glycerol as a plasticizer in solid polymer electrolytes. The addition of glycerol increased salt dissociation and decreased the bulk resistance of the electrolyte [10]. Another study proposed the use of glycerol as one of the components of anhydrous gel electrolytes for flexible supercapacitor applications [90]. Glycerol was also investigated in a study about ionic liquid-based electrolytes for supercapacitors applications [74]. Due to high viscosity and hygroscopic properties, the use of glycerol as an alternative electrolyte for supercapacitors is still very limited, and there have not been many studies in this regard.

3.6. Choline chloride

Previous studies [85,91,49,54] investigated the application of choline chloride, a quaternary ammonium salt, as a hydrogen bond acceptor in deep eutectic solvents (DES). A study [85] about DES for the electrochemical synthesis of silver nanoparticles stated that the addition of choline chloride to glycerol decreased viscosity and increased the conductivity of the eutectic mixture. Another study [54] about an alternative electrolyte for supercapacitors operating over a wide temperature range, reported a high gravimetric capacitance of 362 F g^{-1} at 115 °C and a gravimetric capacitance of 102 F g^{-1} at -40 °C. A study [74] about ionic liquid-based electrolytes also reported the use of choline chloride for supercapacitors operating at room temperature and at 80 °C. A summary of the properties of choline chloride can be seen in Table 6, and the structure of choline chloride-glycerol as a DES is presented in Figure 9.

Table 6 - Properties of choline chloride ($C_5H_{14}ClNO$)

Chemical class	Quaternary ammonium salts	
Molecular formula	$C_5H_{14}ClNO$	
Molecular weight (g mol^{-1})	139.62	
Hydrogen bond donor count	1	
Hydrogen bond acceptor count	2	
Physical description	Hygroscopic white crystals	
Melting point (°C)	302 - 305	
pH	4.7	
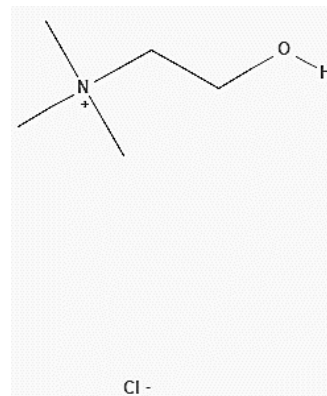
Source: author. Based on the data obtained from multiple sources [51,49]

Figure 9 - Structure of choline chloride-glycerol DES
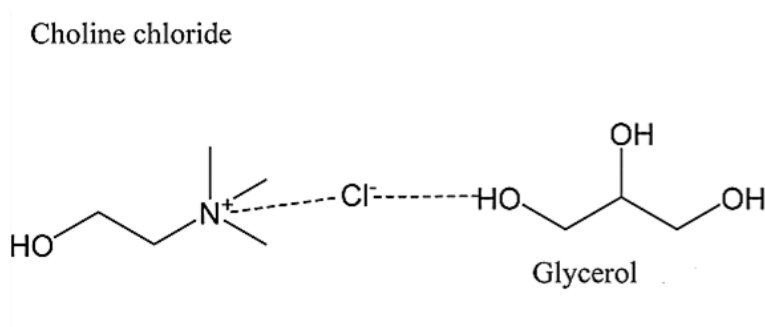
Source: Adapted from Mahto, A. et al. (2017) [92].

3.7. Potassium carbonate

Previous studies [48,86] investigated the application of potassium carbonate, also known as pearl ash, as a hydrogen bond acceptor in deep eutectic solvents (DES). A study by Manurung et al. [47] reported the purification of red palm biodiesel using a deep eutectic solvent (DES) based on K_2CO_3 and glycerol at a molar ratio of 1:5. A study [74] about ionic liquid-based electrolytes reported the use of potassium carbonate for supercapacitors operating at room temperature and at 80 °C. A summary of the properties of potassium carbonate can be seen in Table 7, and the structure of potassium carbonate-glycerol as a DES is presented in Figure 10.

Table 7 - Properties of potassium carbonate (K_2CO_3)

Chemical Class	Basic salts
Molecular formula	K_2CO_3
Molecular weight (g mol^{-1})	138.205
Hydrogen bond donor count	0
Hydrogen bond acceptor count	3
Physical description	Hygroscopic white powder
Boiling point (°C)	Decomposes
Melting point (°C)	891
pH	11.6
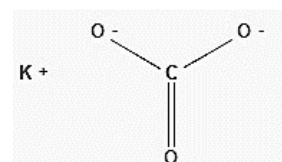
Source: author. Based on the data obtained from multiple sources [52,93]

Figure 10 - Structure of potassium carbonate-glycerol DES
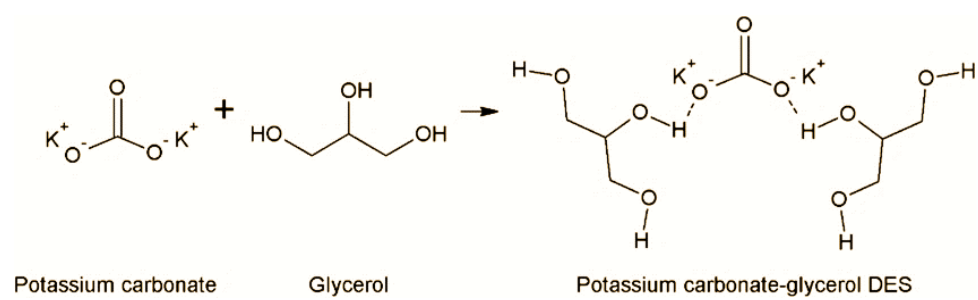
Source: Wei Lun, L. et al. (2017) [94]

4. MATERIALS AND METHODS

Materials & methods are divided into five sections. Sections 1-2 address the production and characterization of the electrodes, respectively. Section 3 addresses the selection and preparation of the electrolytes. Section 4 addresses the assembly of EDLC cells. The final section focuses on the electrochemical characterization of the EDLC cells.

4.1. Production of activated carbon fiber-felt (ACFF) electrodes from textile PAN-based fiber

The production of activated carbon fiber-felt (ACFF) electrodes was based on the methodology proposed in previous studies [63,95,96] and comprised three fundamental processes: oxidation, carbonization, and physical activation (Figure 11) [97].

Figure 11 - Production of activated carbon fiber-felt (ACFF) electrodes from textile PAN-based fiber
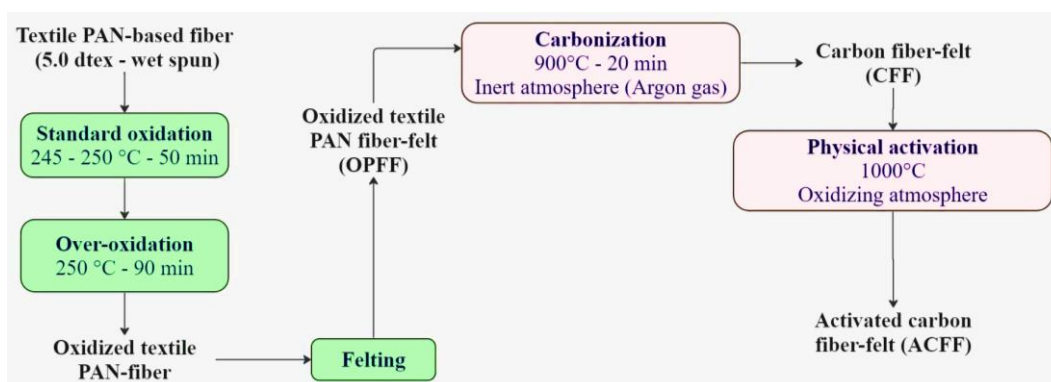
Source: author (2021)

A wet-spun tow of textile PAN-based fiber (5.0 dtex) with a bean-type cross-section was supplied by JMHP Carbon (Figure 12) and used as the raw material for producing the felt. The fiber was converted into a thermoset material through a two-step oxidation process, namely, standard and over-oxidation. The purpose of oxidation is to provide a structure that can withstand high temperatures and to prevent degradation and melting of the fiber in the subsequent carbonization process [44,97]. Standard oxidation was performed in two steps over 50 minutes: pre-oxidation at 245 °C and subsequent oxidation at 250 °C. According to the method introduced by Rodrigues et al. [63], oxidation

time affects the surface chemistry of carbon-based materials and leads to the development of nitrogen groups. These nitrogen compounds, particularly the pyrrolic (C_4H_5N) and the pyridinic (C_5H_5N) functional groups, contribute to increased capacitance. Over-oxidation was carried out for 90 min at 250 °C: totaling 140 min for the entire oxidation process (Figure 13). Oxidized textile PAN-fiber was converted into a felt of 200 g m^{-2} [63] (Figure 14) through a standard needle felting process (non-woven) and designated as oxidized textile Pan fiber-felt (OPFF).

Figure 12 - Textile PAN-based fiber (5.0 dtex) supplied by JMHP Carbon

Source: author (2021)

Figure 13 - Oxidized textile PAN-fiber

Source: author (2021)

Figure 14 - Oxidized textile PAN fiber-felt (OPFF)
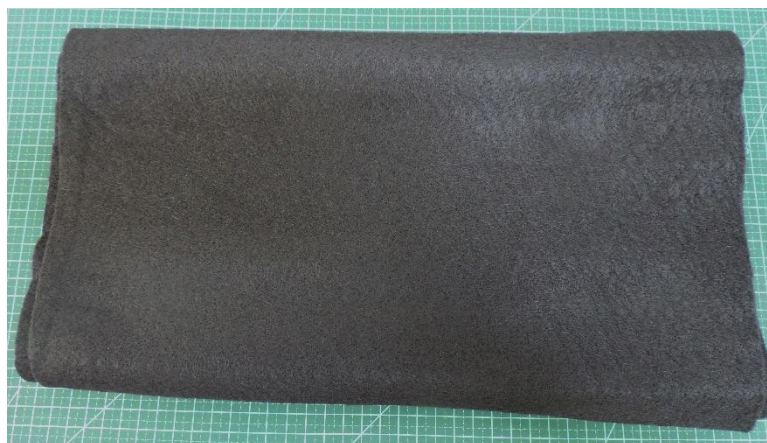
Source: author (2021)

OPFF was carbonized and physically activated in a horizontal tube furnace (Figure 15) in a single step process. The OPFF sample, with a size of 0.27 m², a weight of 48 g, and approximately 3 mm in thickness, was cut and placed in an appropriate sample holder. The carbonization of the OPFF was carried out under an inert atmosphere using argon (Ar). The sample was heated from room temperature to 900 °C at a heating rate of 30 °C min^{-1} and 20 min of residence time. Subsequent carbonization and prior physical activation, the argon gas flow was switched off and replaced with carbon dioxide (200 sccm).

Figure 15 – Schematic diagram of the horizontal tube furnace (carbonization-activation process)
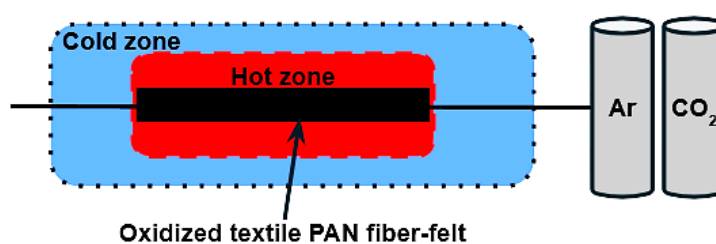
Source: author (2021)

Physical activation was carried out under an oxidizing atmosphere at 1000 °C. Three distinct parameters designated as A1, A2, and A3 were used (Figure 16). The residence time of physical activation processes A1, A2, and A3 was 120 min, 120 min, and 60 min, respectively. Carbon dioxide (CO_2) was the oxidizing agent of physical activation A1. A combination of two oxidizing agents was used during physical activation

processes A2 and A3. Carbon dioxide was the major oxidizing agent and deionized water was the minor oxidizing agent. A syringe was used to introduce a total of 12 ml of deionized water during physical activation processes A2 and A3. Subsequent physical activation, the gas flow was switched off and replaced with argon, and the furnace was turned off. The inert atmosphere was kept through the cooling process until room temperature. The activated carbon fiber-felt sample was designated as ACFF (Figure 17). The yield, which is the efficiency of the carbonization-activation process was calculated by Equation 4.

$$yield\ (\%) = \frac{m_{ACFF}}{m_{OPFF}}\ x\ 100$$

$yield$= carbonization-activation efficiency (%)

m_{ACFF}= mass of ACFF sample (g) (4)

m_{OPFF}= mass of OPFF sample (g)

The burn-off, which is the degree of activation, was estimated by weighing the sample before and after the activation process. During the carbonization process, non-fixed carbon and noncarbon elements, such as nitrogen, hydrogen, and oxygen are removed and released as volatile gases resulting in weight loss and shrinkage [97]. As the carbonization-activation process was carried out in the same furnace, it was considered that during the carbonization process, oxidized PAN lost about 50% in mass [96,98].

Figure 16 - Three distinct physical activation parameters for the production of activated carbon fiber-felt (ACFF) electrodes
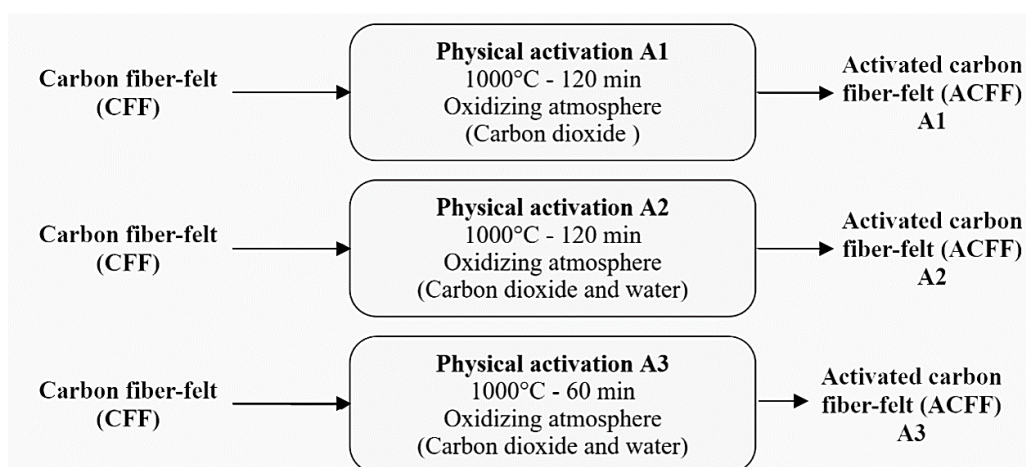
Source: author (2021)

Figure 17 - Activated carbon fiber-felt (ACFF)

Source: author (2021)

4.2. Characterization of activated carbon fiber-felt (ACFF) electrodes

Activated carbon fiber-felt (ACFF) electrodes underwent physical-chemical, textural, morphological, and structural characterizations. Figure 18 shows an overview of the techniques used for the characterization of the ACFF electrodes. Prior to any measurements or characterizations, ACFF samples underwent a grinding process and subsequently a drying process for 2 hours at 110 °C.

Figure 18 - Overview of the techniques used for the characterization of the ACFF electrodes

Physical	Chemical	Textural	Morphological	Structural
Moisture content	Boehm titration	Nitrogen adsorption desorption	Scanning electron microscopy	Raman spectroscopy
Methylene blue number	pH			X-ray diffraction
Iodine number	Point of zero charge			
Apparent density				
Absolute density				
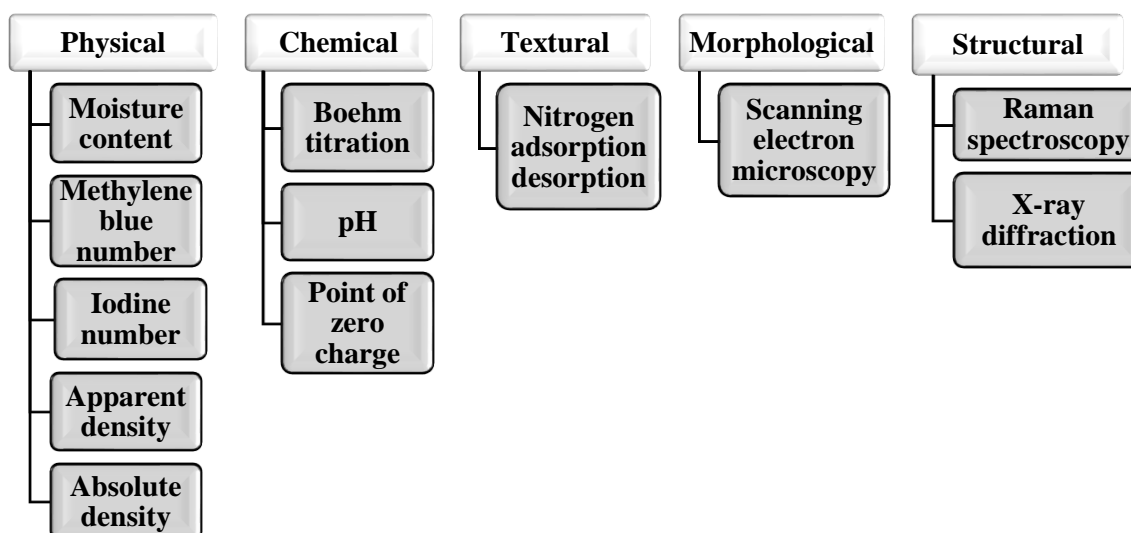
Source: author (2023)

4.2.1. Physical characterization of ACFF electrodes

Moisture content, methylene blue number, and iodine number were performed to confirm the presence of a hydrophilic surface and the presence of porosity developed during the physical activation.

The water adsorption capacity of ACFF samples was determined by moisture content, also known as water content. Analyses were carried out according to the ASTM D2867 method [99]. A Petri dish containing 2 g of fine-powder ACFF sample was placed in a desiccator and reweighed after three days. The moisture content was determined according to Equation 5 and the result was expressed as a percentage of the total weight.

$$M_C = m_f - m_i \; x \left(\frac{100}{m_i}\right)$$

M_C = Moisture content (%)

m_f = Final mass (g)   (5)

m_i = Initial mass (g)

Methylene blue (MB) and iodine solutions were used as adsorbates to deduce the adsorption capacity of the ACFF samples. Based on the methodology proposed in previous studies [100,101], the adsorption capacity was determined by the total volume in ml of standard MB and iodine solutions adsorbed on ACFF samples until no further discoloration occurs. Accurately 0.1 g of the fine-powder ACFF sample was placed in contact with 1 ml additions of methylene blue solution (1000 mg L^{-1}) at room temperature. A magnetic stirrer was used for the homogenization of the sample until discoloration occurred. The same procedure was used for iodine number with 1 ml additions of 0.1 N iodine solution. The total volume in ml of MB and iodine solutions adsorbed, until no further discoloration occurs, was recorded. The results were expressed in milligrams of MB and iodine adsorbed per gram of activated carbon material. Equations 6 and 7 were used to calculate MB_N and I_N, respectively. It is important to note that 0.1 N iodine solution indicates that 12.69 mg of iodine is present in 1 ml of the solution. Moreover, after applying a correction factor, standard MB solution indicates that 0.94 mg of MB is present in 1 ml of the solution.

$$MB_N = \frac{m_{mb}}{m_s}$$

MB_N= Methylene blue number (mg g⁻¹)

m_{mb}= Mass of MB adsorbed on the sample (mg)

m_s= Mass of the activated-carbon sample (g)

(6)

$$I_N = \frac{m_i}{m_s}$$

I_N= Iodine number (mg g⁻¹)

m_i= Mass of iodine adsorbed on the sample (mg)

m_s= Mass of the activated-carbon sample (g)

(7)

Based on the methodology proposed in a previous study [101], methylene blue number (MB_N) and the iodine number (I_N) were also used to estimate the value of the surface area of the ACFF samples through multiple regression, as per Equation 8. According to the size of a methylene blue molecule (area of $\approx$ 2.08 nm²), MB is mostly adsorbed in the small mesopores (2-50 nm) and in a small portion of larger micropores (< 2 nm). Alternatively, iodine molecule is smaller (area of $\approx$ 0.4 nm²) and it is adsorbed in smaller micropores [101].

$$S = 2.28 \; x \; 10^2 - 1.01 \; x \; 10^{-1} \; MB_N + 3.00 \; x \; 10^{-1} \; I_N + 1.05 \; x \; 10^{-4} \; MB_N{}^2 + 2.00 \; x \; 10^{-4} \; I_N{}^2 + 9.38 \; x \; 10^{-4} \; MB_N I_N$$

I_N= Iodine number (mg g⁻¹)

MB_N= Methylene blue number (mg g⁻¹)

S= Estimated surface area (m² g⁻¹)

(8)

The apparent density and the absolute density of ACFF samples were determined according to ISO 10119:2020 methods B (float-and-sink) and D (gas displacement pycnometer), respectively [102]. The apparent density, also known as bulk density, was determined by simply observing the state of equilibrium of the sample in a liquid mixture that has the same density as the sample. If the sample is denser than the liquid mixture, it will sink. Otherwise, if the sample is less dense than the liquid mixture, it will float. Approximately 1000 μg of fine-powder ACFF samples were immersed in a series of liquid mixtures of known densities to cover a specific range: from 1.59 g cm⁻³ (carbon tetrachloride) to 2.17 g cm⁻³ (dibromoethane). Absolute density, also known as true density, was carried out in a gas displacement pycnometer by Micromeritics AccuPyc II 1340 in accordance with the directions given by the manufacturer of the instrument [103].

Helium, an inert gas, was used as the displacement medium. A 10 cm^3 nominal cell volume containing 1.0 cm^3 and 3.5 cm^3 cups was also used. Prior to any measurements, the pycnometer cell volume and expansion volume were calibrated. Empty sample cups were weighed. Accurately 0.20 g and 0.15 g of the ACFF samples were weighed to obtain the maximum sample weight in the 3.5 cm^3 and 1.0 cm^3 cups, respectively. The loaded sample cup was placed in the sample chamber and the analysis started.

4.2.2. Chemical characterization of ACFF electrodes

The pH and the point of zero charge (PZC) of ACFF samples were measured according to ASTM D3838-05(2017) method [104] using a portable pH meter model pH-1900 by Instrutherm. Standard pH buffer solutions were used for calibrating the pH meter. The determination of pH values was carried out by gently boiling 50 ml of deionized water in an Erlenmeyer flask containing 0.5 g of the sample for 5 minutes. The pH was measured after the solution was cooled down to room temperature, diluted to 100 ml, and filtered. Determination of the PZC values was carried out by stirring, for 7 days, 100 ml of deionized water in an Erlenmeyer flask containing 0.5 g of the sample. The pH (PZC) was measured after the solution was filtered.

Boehm titration method (Figure 19) was used for the quantification of oxygen-containing surface functional groups on ACFF samples. The methodology proposed was based on previous works [105,106]. The quantification of the basic functional group was calculated according to Equation 9. Acid-base direct titration of HCl (hydrochloric acid) was carried out with NaOH (sodium hydroxide) as the titrant. A blank titration (absence of analyte) was also performed. The quantification of the basic group was carried out by stirring for 24 hours, in a magnetic stirrer, 25 ml of HCl (0.1 mol L^{-1}) in an Erlenmeyer flask containing 0.5 g of the sample. Three filtered aliquots with a volume of 10 ml were taken. Phenolphthalein indicator was added to the aliquots before titration with NaOH (0.1 mol L^{-1}). The total volume in ml of NaOH added during titration was recorded.

Figure 19 - Quantification of surface functional groups by Boehm titration method
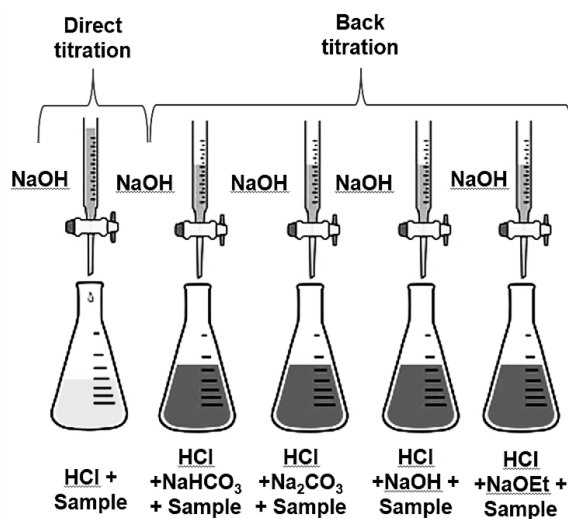
Source: author (2021)

$$Q_{basic} = \frac{V_{HCl} \; x \; C_{HCl} \; x \; \left(\frac{V_b - V_{NaOH}}{V_a}\right)}{m}$$

Q_{basic} = basic functional group (mmol g^{-1})

V_{HCl} = volume of HCl (ml)

C_{HCl} = concentration of HCl (mol L^{-1})

V_b = volume of blank (ml)

V_{NaOH} = volume of NaOH added (ml)

V_a = volume of aliquot (ml)

m = mass of sample (g)

(9)

The quantification of acidic functional groups was carried out using a back-titration method, also known as the indirect method. Blank titrations (absence of analyte) were also performed. Four bases with different strengths were used (Figure 20): sodium bicarbonate (NaHCO$_3$), sodium carbonate (Na$_2$CO$_3$), sodium hydroxide (NaOH), and sodium ethoxide (NaOEt). The pK$_a$ values of these bases are 6.4, 10.3, 15.7, and 20.6, respectively. Titration with NaOH neutralizes carboxylic (pK$_a$ = 3-6), lactonic (pK$_a$ = 7-9), and phenolic groups (pK$_a$ = 8-11), while titration with Na$_2$CO$_3$ neutralizes carboxylic and lactonic groups, and titration with NaHCO$_3$ neutralizes carboxylic groups. Moreover, titration with NaOEt neutralizes the carbonyl group (pK$_a$ = 16-20)[107]. The quantification of acidic functional groups was calculated according to Equation 10.

Figure 20 - Neutralization of oxygen-containing surface functional groups
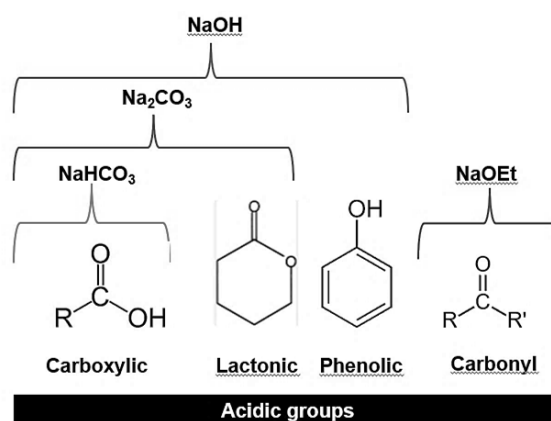
Source: author (2021)

$$Q_{acidic} = \frac{V_{base} \; x \; C_{base} \; x \; \left(\frac{V_{NaOH} - V_b}{V_a}\right)}{m}$$

Q_{acidic} = acidic functional group (mmol g⁻¹)

V_{base} = volume of base (ml)

C_{base} = concentration of base (mol L⁻¹)

V_b = volume of blank (ml)

V_{NaOH} = volume of NaOH added (ml)

V_a = volume of aliquot (ml)

m = mass of sample (g)

(10)

The quantification of the carboxylic group was carried out by stirring for 24 hours, in a magnetic stirrer, 25 ml of $NaHCO_3$ (0.1 mol L⁻¹) in an Erlenmeyer flask containing 0.5 g of the sample. Three filtered aliquots with a volume of 10 ml were taken. Phenolphthalein indicator and 20 ml of HCl (0.1 mol L⁻¹) were added to the aliquots. Prior to titration with NaOH (0.1 mol L⁻¹), aliquots were gently boiled and cooled down. The total volume in ml of NaOH added during titration was recorded.

The quantification of the carboxylic and lactonic groups was carried out by stirring for 24 hours, in a magnetic stirrer, 25 ml of Na_2CO_3 (0.05 mol L⁻¹) in an Erlenmeyer flask containing 0.5 g of the sample. Three filtered aliquots with a volume of 10 ml were taken. Phenolphthalein indicator and 15 ml of HCl (0.1 mol L⁻¹) were added to the aliquots. Prior to titration with NaOH (0.1 mol L⁻¹), aliquots were gently boiled and cooled down. The total volume in ml of NaOH added during titration was recorded. As the back titration

with NaHCO$_3$ only neutralizes carboxylic groups, the value for the quantification of lactonic groups can be calculated by subtracting the result of back titration with NaHCO$_3$ from Na$_2$CO$_3$.

The quantification of the carboxylic, lactonic, and phenolic groups was carried out by stirring for 24 hours, in a magnetic stirrer, 25 ml of NaOH (0.1 mol L^{-1}) in an Erlenmeyer flask containing 0.5 g of the sample. Three filtered aliquots with a volume of 10 ml were taken. Phenolphthalein indicator and 15 ml of HCl (0.1 mol L^{-1}) were added to the aliquots before titration with NaOH (0.1 mol L^{-1}). The total volume in ml of NaOH added during titration was recorded. The value for the quantification of phenolic groups can be calculated by subtracting the result of back titration with NaHCO$_3$ and Na$_2$CO$_3$ from the back titration with NaOH.

The quantification of the carbonyl group was carried out by stirring for 24 hours, in a magnetic stirrer, 25 ml of NaOEt (0.1 mol L^{-1}) in an Erlenmeyer flask containing 0.5 g of the sample. Three filtered aliquots with a volume of 10 ml were taken. Phenolphthalein indicator and 15 ml of HCl (0.1 mol L^{-1}) were added to the aliquots before titration with NaOH (0.1 mol L^{-1}). The total volume in ml of NAOH added during titration was recorded.

4.2.3. Textural characterization of ACFF electrodes

The surface textural properties of the ACFF samples were analyzed by Nitrogen (N$_2$) adsorption–desorption isotherms at 77 K using an ASAP 2020 Plus adsorption analyzer by Micromeritics. Specific surface area (S$_{BET}$), average pore size, pore volume, pore size distribution, and micropore volume were analyzed. Sample analysis and sample preparation were performed in accordance with the directions given by the manufacturer of the instrument. Prior to the measurements, degasification of the sample was performed at 120 °C for 12 h under vacuum pressure of 5 μmHg.

4.2.4. Morphological characterization of ACFF electrodes

Scanning electron microscopy (SEM) analysis was used to investigate the surface morphology and the surface topography of the ACFF samples, such as geometrical shape, surface orientation, edges, roughness, and texture [108]. SEM images of the samples were characterized by Philips XL30 SEM with a LaB6 (lanthanum hexaboride) source electron gun. The instrument was operated at an accelerating voltage of 20 kV, using a secondary electrons (SE) detector, and various magnifications. Sample analysis and sample preparation were performed in accordance with the directions given by the manufacturer of the instrument.

4.2.5. Structural characterization of ACFF electrodes

The structural characterization of ACFF samples was carried out by Raman-scattering spectroscopy technique using Horiba Scientific model Labram HR Evolution. Sample analysis and sample preparation were performed in accordance with the directions given by the manufacturer of the instrument. Ar ion laser operating at 512 nm and scan mode of 1000 - 2500 cm^{-1} were employed to collect Raman spectra. In addition to the Raman technique, X-ray diffraction (XRD) was used to characterize the crystalline structure of the ACFF samples.

4.3. Selection and preparation of electrolytes

In order to understand the electrochemical behavior of the ACFF electrodes in aqueous and glycerol-based electrolytes, the following electrolytes were selected:

I. Potassium hydroxide (KOH) solutions with molar concentrations of 1 mol L^{-1} and 2 mol L^{-1} were used as examples of conventional and strong alkaline electrolytes.

II. Sulfuric acid (H$_2$SO$_4$) solutions with molar concentrations of 1 mol L^{-1} and 2 mol L^{-1} were used as examples of conventional and strong acidic electrolytes.

III. Aiming to investigate green electrolytes, three distinct glycerol-based electrolytes with various molar ratios were used: potassium hydroxide-glycerol hybrid electrolytes (KOH:GLY), potassium carbonate-glycerol hybrid electrolyte (K_2CO_3:GLY), and choline chloride-glycerol hybrid electrolyte (ChCl:GLY). KOH:GLY was prepared with variations of viscosity and molar ratios of 3:1, 2:1, 1:1, 1:2, and 1:3 (Figure 21). ChCl:GLY and K_2CO_3:GLY were prepared at a molar ratio of 3:1 instead (Figure 22).

Figure 21 - KOH:GLYs (Potassium hydroxide-glycerol hybrid electrolytes) with variations of viscosity and molar ratios of 3:1, 2:1, 1:1, 1:2, 1:3
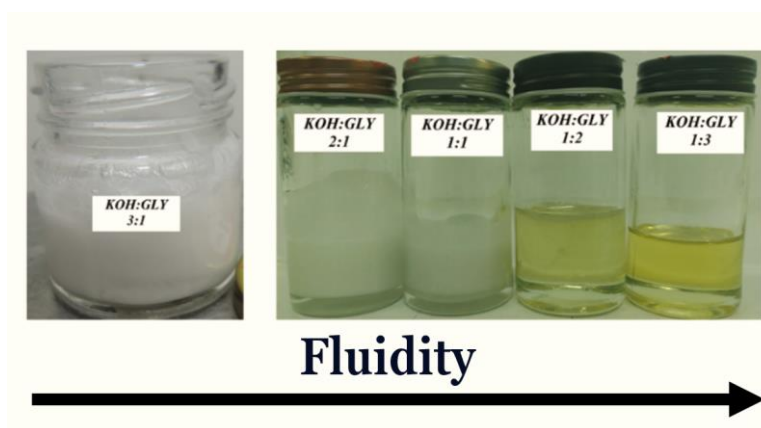
Source: author (2022)

Figure 22 - ChCl:GLY (Choline chloride-glycerol hybrid electrolyte) and K_2CO_3:GLY (Potassium carbonate-glycerol hybrid electrolyte) at a molar ratio of 3:1

Source: author (2023)

The selection of glycerol-based electrolytes was based on previous studies: (a) a study [90] carried out in anhydrous gel electrolytes for flexible supercapacitor applications

over a broad temperature domain, and (b) a study [74] carried out in ionic liquid-based electrolytes for supercapacitors operating at room temperature and at 80 °C.

H_2SO_4 solutions with molar concentrations of 1 mol L^{-1} and 2 mol L^{-1} were prepared by diluting 55.62 ml and 111.24 ml, respectively, of the stock solution (sulfuric acid 96%) to a final volume with deionized water. The solutions were stirred at room temperature for 20 min, transferred to a dry storage bottle, and labeled. KOH solutions with molar concentrations of 1 mol L^{-1} and 2 mol L^{-1} were prepared by dissolving 56.11 g and 112.21 g, respectively, of the solid compound (KOH 100% purity) in deionized water. Once the solid is completely dissolved, the solutions were diluted to a final volume with deionized water. The solutions were stirred at room temperature for 20 min, transferred to a dry storage bottle, and labeled.

The purity and the proportion of the solid compound and the stock solution used to prepare the glycerol-based electrolytes can be seen in Table 8. The electrolytes were prepared by dissolving the solid compound (KOH, K_2CO_3, or $C_5H_{14}CINO$) in the stock solution ($C_3H_8O_3$) by stirring for 6 – 8 hours at a constant temperature of 80°C. The electrolytes were labeled and stored in a vacuum desiccator for 24 - 48 hours to remove possible moisture content.

Table 8 - Purity and proportion of the solid compound and the stock solution used to prepare the glycerol-based electrolytes.

Molar ratio	Solid compound (g)	Stock solution (g)
KOH:GLY	**KOH (100% purity)**	**$C_3H_8O_3$ (95% purity)**
3:1	16.83	9.70
2:1	11.22	9.70
1:1	5.61	9.70
1:2	5.61	19.38
1:3	5.61	29.08
ChCl:GLY	**$C_5H_{14}CINO$ (100% purity)**	**$C_3H_8O_3$ (95% purity)**
3:1	41.88	9.70
K_2CO_3:GLY	**K_2CO_3 (99% purity)**	**$C_3H_8O_3$ (95% purity)**
3:1	41.87	9.70

Source: author (2021-2022)

4.4. Assembly of electric double-layer capacitor (EDLC) cells

The ACFF sample was cut into small disks with a diameter of 8 mm and a footprint area of 0.5 cm^2. In order to remove moisture, ACFF electrodes underwent a drying process for 2 hours at 110 °C. Subsequent drying, the electrodes were weighed and stored in a vacuum desiccator. Before assembling the symmetric EDLC cell, ACFF electrodes were immersed in aqueous-based electrolytes for 24 hours (Figure 23).

Figure 23 - Activated carbon fiber-felt (ACFF) electrodes immersed in acidic and alkaline aqueous electrolytes

Source: author (2021)

Due to the high viscosity of glycerol-based electrolytes, particularly at molar ratios of 3:1, 2:1, and 1:1, and to improve electrolyte diffusion, electrode-electrolyte contact for approximately 2 - 3 hours, at room temperature (RT), is recommended (Figure 24). After electrolyte diffusion at RT (Figure 25), ACFF electrodes, impregnated with glycerol-based electrolytes, were stored in vacuum desiccators for 48 hours to remove moisture.

Figure 24 - Activated carbon fiber-felt (ACFF) electrodes and a qualitative filter paper (separator) impregnated with potassium hydroxide-glycerol hybrid electrolyte (KOH:GLY) before the diffusion process at room temperature

Source: author (2022)

Figure 25 - Activated carbon fiber-felt (ACFF) electrodes impregnated with potassium hydroxide-glycerol hybrid electrolyte (KOH:GLY) after the diffusion process at room temperature
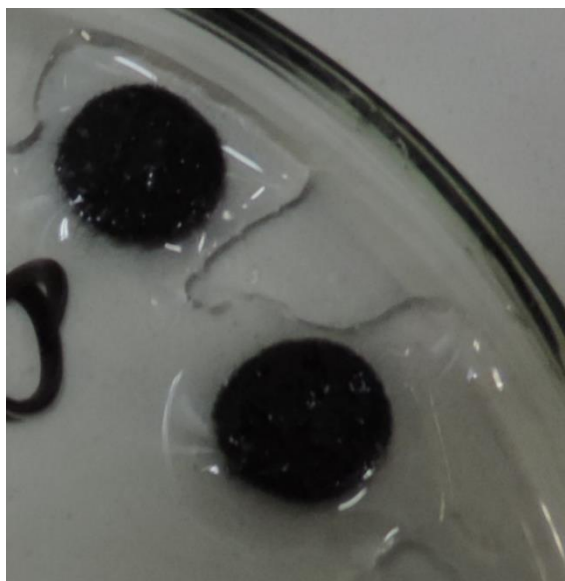
Source: author (2022)

A qualitative cellulose filter paper (0.2 mm in thickness) was cut into small disks with a diameter of 10 mm and used as a separator to keep the two electrodes apart and prevent a short circuit (Figure 26). Due to the self-supporting characteristics of the ACFF electrodes, binders are not required. Symmetric EDLC was assembled in a two-electrode Swagelok®-cell with a Teflon case and two high-density fine-grain graphite rods as current collectors (Figure 27). A Faraday cage was used to avoid external interferences (Figure 28).

Figure 26 - Interior view of Swagelok®-type cell containing two symmetric activated carbon fiber-felt (ACFF) electrodes impregnated with the electrolyte and a qualitative filter paper as the separator
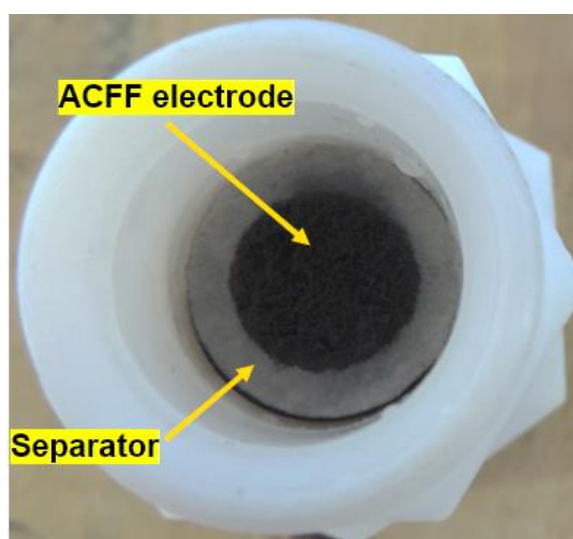
Source: author (2022)

Figure 27 - A two-electrode Swagelok®-type cell with a Teflon® case and two high-density fine-grain graphite rods as current collectors
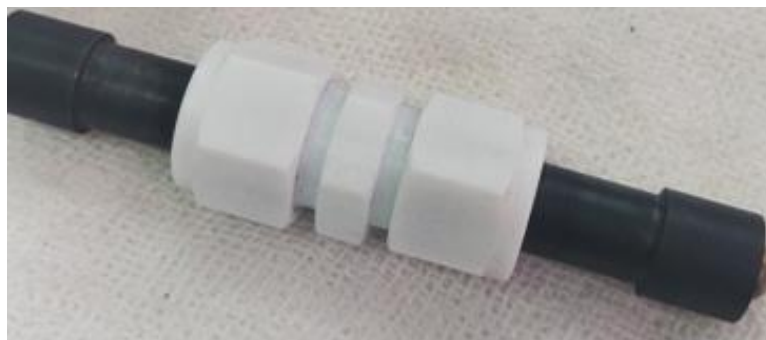
Source: author (2022)

Figure 28 - Assembled electric double-layer capacitor (EDLC) cell in a Faraday cage

Source: author (2022)

4.5. Electrochemical characterization of the electric double-layer capacitor (EDLC) cells

Electrochemical impedance spectroscopy (EIS), cyclic voltammetry (CV), and galvanostatic charge-discharge (GCD) techniques were conducted to evaluate the performance and the electrochemical characteristics of ACFF electrodes in aqueous and glycerol-based electrolytes (Figure 29). Electrochemical measurements were carried out in a symmetric two-electrode cell (Swagelok®-type) at room temperature (RT) in a multichannel potentiostat (Parstat MC) by Princeton Applied Research. Origin software version 9.70 was used for data analysis and graphing. Good practice for electrochemical characterization of supercapacitors, as those reported in previous works [109,110], and an error of $\pm 10\%$ in the values were taken into consideration.

Figure 29 - Overview of the techniques used for the electrochemical characterization of the ACFF-based EDLC cells in aqueous and glycerol-based electrolytes
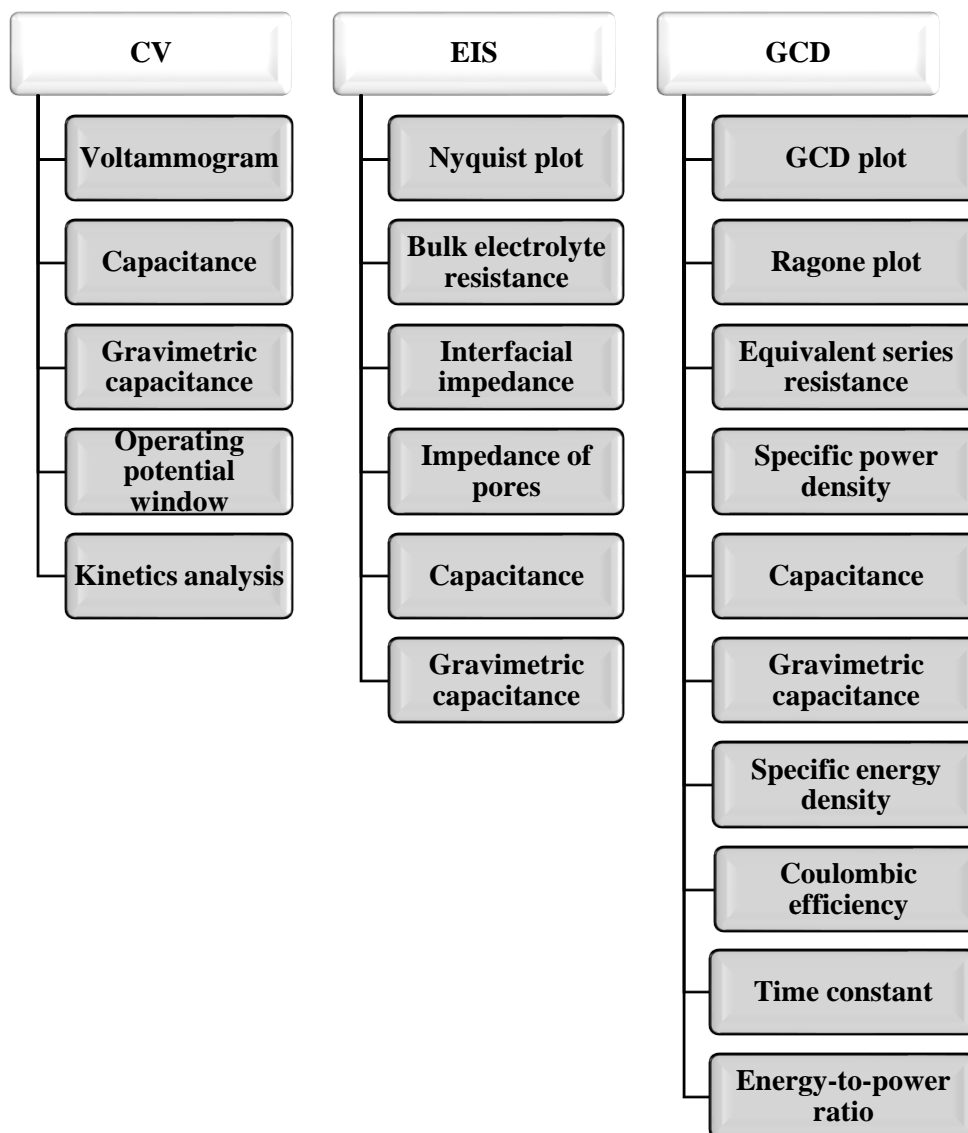
Source: author (2023)

4.5.1. Cyclic voltammetry (CV)

Cyclic voltammetry, a transient technique, enables the determination of the operating potential window of electrolytes, the measurement of capacitance and its corresponding gravimetric capacitance, as well as kinetic analysis by scanning at a diverse range of scan rates [111,112,113]. The principle of the CV technique is to measure the resultant current by applying a linear voltage ramp between the two voltage limits [111]. The data is plotted in a voltammogram as current (A) vs. potential (V). Capacitance (C), which is the ability to store charge per volt, is given in units of Farads (F). As capacitance is constant over an acknowledged potential window, rectangular CV curves are expected in the cyclic voltammogram for an ideal capacitive behavior (Figure 30a) [110,111]. Nevertheless, actual EDLCs exhibit nearly rectangular CV curves with blunt corners (Figure 30b) due to the equivalent series resistance of the cell (ESR), also known as internal resistance [114,112,113]. Slanted rectangular CV curves (Figure 30c) occur due to the equivalent parallel resistance (EPR), which is related to the leakage effect and results in self-discharge characteristics [115,112]. Although it deviates from a desired CV profile, a mix of blunt and slanted CV curves may occur (Figure 30d).

Figure 30 – Schematic CV curves for electric double-layer capacitor (EDLC) (a) ideal CV profile, (b) presence of equivalent series resistance (ESR), (c) presence of equivalent parallel resistance (EPR), and (d) presence of both ESR and EPR.

(a) (b) (c) (d)
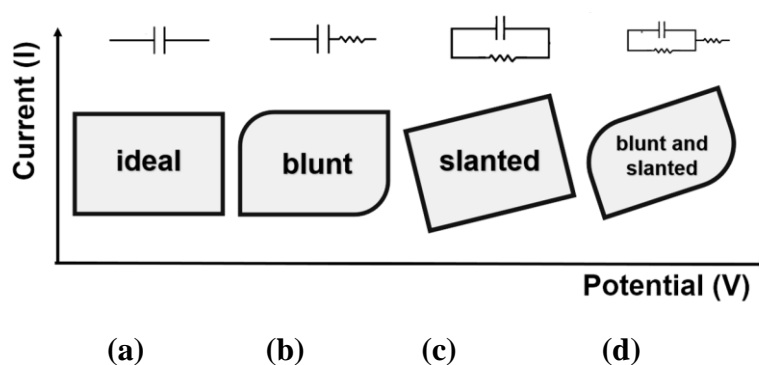
Source: author (2023)

Capacitance ($C_{(CV)}$) was estimated from the integration of the area under the CV curve according to Equation 11 [112,116]:

$$C_{(CV)} = \left(\frac{\int_{V_1}^{V_2} i(V)d(V)}{2v(V_2 - V_1)}\right) \qquad$$

$C_{(CV)}$ = capacitance (F)

$\int_{V_1}^{V_2} i(V)d(V)$ = area under the curve (V A)

v = scan rate (V s^{-1})

$V_2 - V_1$ = potential difference (V)

(11)

The gravimetric capacitance of the cell C_g was calculated according to Equation 12 [117]. It was considered the capacitance for the two-electrode cell.

$$C_g = \frac{4C}{m}$$

C_g = gravimetric capacitance of the cell (F g^{-1})

C = capacitance (F)

m = total active mass of the electrodes (g)

(12)

CV measurements were conducted at a scan rate of 1 mV s^{-1} at room temperature (RT) for both aqueous and glycerol-based electrolytes. Due to water electrolysis (decomposition at 1.23 V) [118,119], CV measurements of aqueous electrolytes were carried out within a potential window of 0 - 1 V. As the electrochemical stability window of glycerol-based electrolytes (up to 2.1 V) [74] is greater, CV measurements were carried out within a potential window of 0 – 2.1 V.

4.5.2. Electrochemical impedance spectroscopy (EIS)

EIS, a stationary technique, measures the impedance response as a function of frequency. The impedance response recorded by the instrument was expressed graphically in a Nyquist plot. A schematic Nyquist plot of real impedance versus imaginary impedance for EDLCs can be seen in Figure 31. The real part (Z_{re}), which is resistive, is plotted on the x-axis of the Nyquist plot while the imaginary part (Z_{im}), which is capacitive, is plotted on the y-axis. A Nyquist plot comprises three main frequency regions ranging from higher to lower frequency: a high-frequency region that is higher than 10 kHz, a medium-frequency region ranging from 10 kHz to 1 Hz, and a low-frequency region that is lower than 1 Hz [120]. Moreover, three distinct components of the

total impedance can be seen in the Nyquist: bulk resistance, interfacial impedance, and impedance of pores [121].

At high frequencies, supercapacitors exhibit a resistive behavior that is related to the bulk resistance [122]. Bulk electrolyte resistance (R_e), which is the contact resistance outside the pores (Figure 32), was estimated at the point where the imaginary capacitance tends to zero and the plot intercepts the x-axis (Z_{re}) at high frequencies [123,121]. The interfacial impedance between the bulk solution (electrolyte) and the electrode can be observed at medium frequencies through a semicircle [121]. A semicircle can occur due to interfacial contact resistance at the current collector / active material or due to charge transfer resistance (R_{ct}) because of the presence of functional groups on the surface of the carbon materials [123,114]. Following the semicircle, a 45° line, or slope, at low frequency region is associated with the intra-particle pores (impedance of pores) [121]. The longer the line, the more difficult it becomes for the electrolyte to access the entire surface of the electrode [116]. Thus, a gradual slope suggests that the ion diffusion into the pores occurs laboriously. On the contrary, a steep slope suggests that ion penetration into pores occurs efficiently due to the formation of the electric double-layer (EDL) [124,114]. At low frequencies, a vertical line (90°) parallel to the y-axis (Z_{im}) indicates that capacitance is constant over the applied frequency range, thus the electrode surface is entirely impregnated [125,121,116,124]. The more the vertical line leans towards the y-axis (Z_{im}), the better the capacitive behavior [126]. While R_e relies upon the electrolyte solution, 45° and 90° lines depend on both the electrode and electrolyte [121].

Capacitance $C_{(EIS)}$ was determined using the imaginary part (Z_{im}) of the Nyquist plot at the lowest frequency applied (or frequencies < 1 Hz), according to Equation 13 [120,127]:

$$C_{(EIS)} = -\frac{1}{2\pi f Im(Z)} \qquad \begin{array}{l} C_{(EIS)} = \text{capacitance (F)} \\ f = \text{lowest frequency applied or frequencies} < 1 \text{ (Hz)} \\ Im(Z) = \text{imaginary impedance } (\Omega) \end{array} \qquad (13)$$

The gravimetric capacitance of the cell (C_g) from EIS was calculated according to Equation 12, which was presented in the preceding section. EIS measurements for aqueous and glycerol-based electrolytes were carried out under the same condition at

room temperature, over a frequency range of 10^{-3} Hz - 10^6 Hz, at an applied signal amplitude of 5 mV, and at an applied potential of 0 V.

Figure 31 - Schematic Nyquist plot for an electric double-layer capacitor (EDLC)
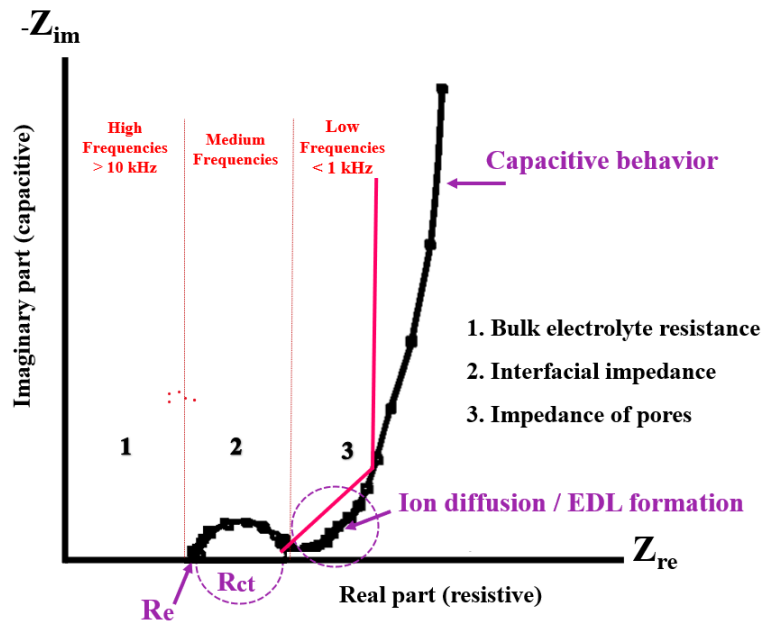
Source: author (2023)

Figure 32 - Schematic diagram of a cylindrical pore. Each pore is represented by an equivalent circuit model with capacitors connected in parallel and resistance connected in series as a function of pore depth
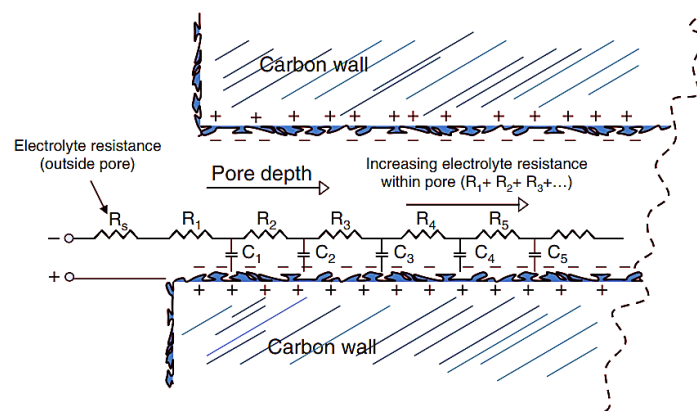
Source: Pandolfo, T. et al. (2013) [128]

4.5.3. Galvanostatic charge-discharge (GCD)

Galvanostatic charge-discharge (GCD), a transient technique, was used to evaluate the electrochemical performance of the cell. In this technique, the applied current is constant while the response, or voltage, is measured as a function of time [116,129]. As can be seen in Figure 32, the data is plotted in a GCD plot as voltage (V) vs. time (s).

Figure 33 - Schematic GCD plot for an electric double-layer capacitor (EDLC)
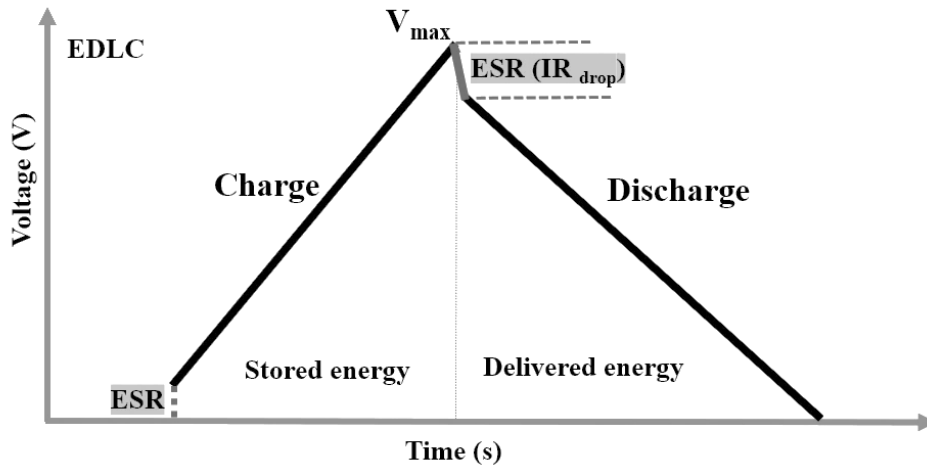
Source: author (2023)

GCD was used to determine the equivalent series resistance (ESR) of the cell, also known as internal resistance. As the voltage drop (IR_{drop}) is related to the internal resistance of the cell when the current is interrupted or inversed, the value of ESR was deduced according to Equation 14 [127] [129]:

$$ESR = \left| \frac{IR_{drop}}{2I} \right|$$

ESR = equivalent series resistance (Ω)

IR_{drop} = voltage drop (V)

I = applied current (A)

(14)

Specific power density (P_D), which is the maximum power output per unit of mass, depends on the voltage and on the internal resistance of the cell. P_D was calculated according to Equation 15 [27]:

$$P_D = \frac{V_{max}^2}{4ESRm}$$

P_D = specific power density (W kg^{-1})

ESR = equivalent series resistance (Ω)   (15)

V_{max} = maximum potential (V)

m = total active mass of the electrodes (kg)

The Coulombic efficiency of the cell (η), which is the ratio of the discharging time and the charging time, was calculated using equation 16 [130]:

$$\eta = \frac{T_d}{T_c} \, 100$$

η = Coulombic efficiency of the cell (%)

T_d = discharging time (s)   (16)

T_c = charging time (s)

Capacitance $C_{(GCD)}$ was calculated using the slope of the discharge curve and Equation 17. Specific energy density (E_D), which is the amount of energy stored per unit of weight, was calculated according to Equation 18 [129,114].

$$C_{(GCD)} = \frac{(I_{(discharge)}(t_i - t_f))}{(V_{max} - IR_{drop})}$$

$C_{(GCD)}$ = capacitance (F)

$I_{(discharge)}$ = discharging current (A)   (17)

$(t_i - t_f)$ = time difference (s)

V_{max} = maximum potential (V)

IR_{drop} = voltage drop (V)

$$E_D = \frac{1}{2} \frac{C_{(GCD)}V_{max}^2}{3600m}$$

E_D = specific energy density (Wh kg^{-1})

$C_{(GCD)}$ = capacitance (F)   (18)

V_{max} = maximum potential (V)

m = total active mass of the electrodes (kg)

The gravimetric capacitance of the cell (C$_g$) from GCD was calculated according to Equation 12, which was presented in section 4.5.1.

The product of capacitance (C) and equivalent series resistance (ESR) results in the time constant (τ) of the supercapacitor device. The time constant (τ) was determined according to Equation 19 [127]:

$$\tau = \text{time constant (s)}$$

$$\tau = ESR \; C_{(GCD)} \qquad ESR = \text{equivalent series resistance } (\Omega) \qquad (19)$$

$$C_{(GCD)} = \text{capacitance (F)}$$

GCD measurements for aqueous and glycerol-based electrolytes were carried out under the same condition at room temperature and at a potential window of 0 - 1 V, under various current densities. A Ragone plot was used to compare the overall electrochemical performance of the EDLC cells in comparison to other energy storage devices. The data was plotted as specific energy density versus specific power density.

5. RESULTS AND DISCUSSION

Results and discussion are divided into ten sections. Sections 1-4 address the production and characterization of the electrodes. Section 5 addresses the assembly of EDLC cells. Sections 6-10 focus on the electrochemical characterization of the EDLC cells.

5.1. Influence of physical activation on the production of activated carbon fiber-felt (ACFF) electrodes from textile PAN-based fiber

The results in Table 9 summarize the efficiency of the carbonization-activation process. Activation parameters, such as oxidizing agents and residence time, influenced the yield, mass loss, shrinkage, and burn-off percentage of the samples. Physical activation A1, which was carried out with a single oxidizing agent resulted in higher yield percentage. In contrast, physical activation A2 and A3, which were carried out with two oxidizing agents, resulted in higher mass loss, shrinkage, and burn-off percentages.

Table 9 - Efficiency of the carbonization-activation process on the production of activated carbon fiber-felt (ACFF) electrodes from textile PAN-based fiber

ACFF samples	A1	A2	A3
Oxidizing agent	CO_2	$CO_2 + H_2O$ *	$CO_2 + H_2O$ *
Residence time (min)	120	120	60
Yield (%)	44	36	21
Mass loss (%)	56	64	79
Shrinkage (%)	28	41	43
Burn-off (%)	6	14	29

*12 ml of H_2O and 200 sccm CO_2

Source: author (2021)

5.2. Physical and chemical properties of activated carbon fiber-felt (ACFF) electrodes

5.2.1. Physical properties of ACFF electrodes

Tables 10 and 11 summarize the physical properties of ACFF samples. The moisture content, which is the amount of water adsorbed by the ACFF samples, is in the range of 3 – 41% w/w. The moisture content of ACFF sample A3 is about three times and thirteen times greater than that of samples A1 and A2, respectively. As water fills accessible pores, it is assumed that the volumetric porosity of the ACFF sample A3 is relevant for aqueous-based electrolytes.

The iodine adsorption capacity of common activated carbon is about 1000 mg g^{-1}, whereas methylene-blue adsorption capacity commonly ranges from 100 to 350 mg g^{-1} [95]. The iodine adsorption capacity of ACFF sample A3 (1006 mg g^{-1}) is eight times greater than that of samples A1 and A2, indicating high microporosity. Additionally, the methylene-blue adsorption capacity of ACFF sample A3 (509 mg g^{-1}) is about fifty times greater than that of samples A1 and A2, indicating the presence of larger micropores and mesopores. The sum of iodine number (I_N) and methylene blue number (MB_N) was used to estimate the value of the surface area through multiple regression [101]. Due to high microporosity, the estimated surface area of sample A3 (1189 $m^2 g^{-1}$), is four times greater than that of samples A1 and A2. While CO_2 leads to the development of new microporosity, water helps to widen the existing micropores. Although the physical activation of samples A2 and A3 was carried out with both oxidizing agents, it is suggested that the decrease in the residence time by 50% resulted in the enhanced adsorption capacity of sample A3. The development of mesopores (2 – 50 nm) may occur by burning off the wall bordering the micropores (> 2 nm) due to an overextended residence time during the activation process [131].

The results show that the parameters of the activation process, such as residence time and oxidizing agents, impacted the overall adsorption capacity of the samples. As a result of the high estimated surface area and high microporosity, ACFF sample A3 should be relevant for applications as electrodes for supercapacitors.

Table 10 - Moisture content, methylene blue number, iodine number, and estimated surface area of activated carbon fiber-felt (ACFF) samples.

ACFF samples	A1	A2	A3
Moisture content (% w/w)	15	3	41
Volume of Methylene blue adsorbed in 100 mg of the sample (ml)	1	1	55
Methylene blue number (mg g^{-1})	9	9	509
Volume of iodine adsorbed in 100 mg of the sample (ml)	1	1	8
Iodine number (mg g^{-1})	117	123	1006
Estimated surface area (m^2 g^{-1}) *	266	268	1189

* Value estimated through multiple regression [101].

Source: author (2021-2022)

Pore volume (cell cavities) is included in the calculation of apparent density. In the case of absolute density (specific mass), the volume of open pores is excluded from the calculation, which means that the absolute density corresponds to the solid carbon skeleton. Similar values for both apparent density and absolute density can be found in samples A1 and A2. Among the ACFF samples, A3 has the highest packing density of 1.87 g cm^3. The absolute density of activated carbons using helium as a displacement fluid provides values ranging from 1.8 to 2.1 g cm^3 [132]. The absolute densities of samples A1 and A2 fall within the specified range. However, the absolute density of sample A3 is the same as the theoretical density of graphite (2.26 g cm^3 at 20 °C) [133], which suggests a measurement error due to a highly porous carbon material.

Table 11 - Apparent and absolute densities of activated carbon fiber-felt (ACFF) samples

ACFF electrodes	A1	A2	A3
Apparent density by float-and-sink method (g cm^{-3})	1.69	1.71	1.87
Absolute density by Pycnometer method (g cm^{-3})	1.82	1.81	2.26

Source: author (2021-2022)

5.2.2. Chemical properties of ACFF electrodes

Tables 12 and 13 summarize the chemical properties of ACFF samples. The pH value, which is a measure of alkalinity or acidity, indicated that the ACFF samples are weak alkalis. The condition at which the electric charge density on the surface is equal to zero (neutral surface) is known as the point of zero charge (PZC), and it is related to the process of adsorption under certain pH conditions [134]. The ACFF samples will have a negatively charged surface and preferably adsorb cations at solutions with pH values greater than the PZC. On the contrary, the ACFF samples will have a positively charged surface and preferably adsorb anions at solutions with pH values less than the PZC. The results demonstrated that the parameters of the activation process, such as residence time and oxidizing agents, do not influence the pH value of the samples. The PZC of the samples were influenced by the activation process, though.

Table 12 - The pH and the point of zero charge (pH PZC) of activated carbon fiber-felt (ACFF samples)
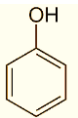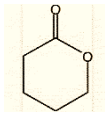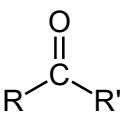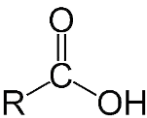
ACFF electrodes	pH	pH PZC
A1	7.9	8.2
A2	7.9	7.4
A3	7.4	7.6

Source: author (2021-2023)

The Boehm titration method was used to quantify the surface basicity and acidity of the samples, as well as the oxygen-containing functional groups. The sum of phenolic, lactonic, carbonyl and carboxylic groups results in the total surface acidity of the sample. The total surface acidity of ACFF samples A1, A2, and A3 are 0.59 mmol g^{-1}, 0.46 mmol g^{-1}, and 1.33 mmol g^{-1}, respectively. In addition, physical activation A3, which had carbon dioxide and water as oxidizing agents, led to an increase by three to four times in the carbonyl groups on the surface of ACFF samples. Physical activation A3 also led to a change in the surface basicity of the samples, as only ACFF sample A3 showed surface basicity (0.75 mmol g^{-1}). According to the Boehm titration method, ACFF sample A3 has more functional groups on its surface and has an acidic behavior for aqueous application (Table 13). The total surface acidity of ACFF sample A3 is six times greater than that of

a PAN-based activated-carbon material reported in a previous study [95], whereas the surface basicity is 1.5 times greater. For a more comprehensive quantitative analysis of surface functional groups, X-ray photoelectron spectroscopy (XPS) is recommended.

Table 13 - Quantification of surface functional groups on activated carbon fiber-felt (ACFF) samples

		Acidic groups (mmol g^{-1})				
		Phenolic	Lactonic	Carbonyl	Carboxylic	
ACFF electrodes	Basic group (mmol g^{-1})	OH	O	O = C, R, R'	O = C, R, OH	Acidic group (mmol g^{-1})
A1	0.00	0.17	0.00	0.42	0.00	0.59
A2	0.00	0.17	0.00	0.29	0.00	0.46
A3	**0.75**	0.18	0.00	1.15	0.00	**1.33**

Source: author (2021-2022)

5.3. Textural, morphological, and structural analyses of activated carbon fiber-felt (ACFF) electrodes

Among the ACFF samples, only sample A3 underwent textural, morphological, and structural characterization by reason of its superior adsorption capacitive and surface functional groups in comparison to samples A1 and A2.

5.3.1. Textural properties of ACFF electrodes

Figures 34 and 35 show the nitrogen gas adsorption-desorption isotherm at 77 K and the pore size distribution of ACFF sample A3, respectively. According to the IUPAC classification of adsorption isotherms for gas-solid equilibria [135], N$_2$ adsorption-desorption isotherm of ACFF sample is classified as Type I with gas saturation occurring at 0.25 P/P$_o$, which indicates a microporous character (Figure 34). Moreover, hysteresis is absent, indicating that the size of the pores measured on both adsorption and desorption branches coincides well due to a regular pore geometry [136,137]. The isotherm of ACFF

sample is analogous to that of PAN-based activated-carbon materials reported in previous studies [95,96,63,65]. ACFF sample has a high specific surface area (S_{BET}) of 1875 m^2 g^{-1} and a correlation coefficient (r) of 0.999918 (Table 14). In comparison to previous studies [95,96,65], the S_{BET} of the ACFF electrodes, produced in this work, is about 1.5 times higher. The microporosity developed particularly during the activation process contributed to high specific surface area.

Figure 34 - Nitrogen adsorption-desorption isotherm of activated carbon fiber-felt (ACFF) sample A3
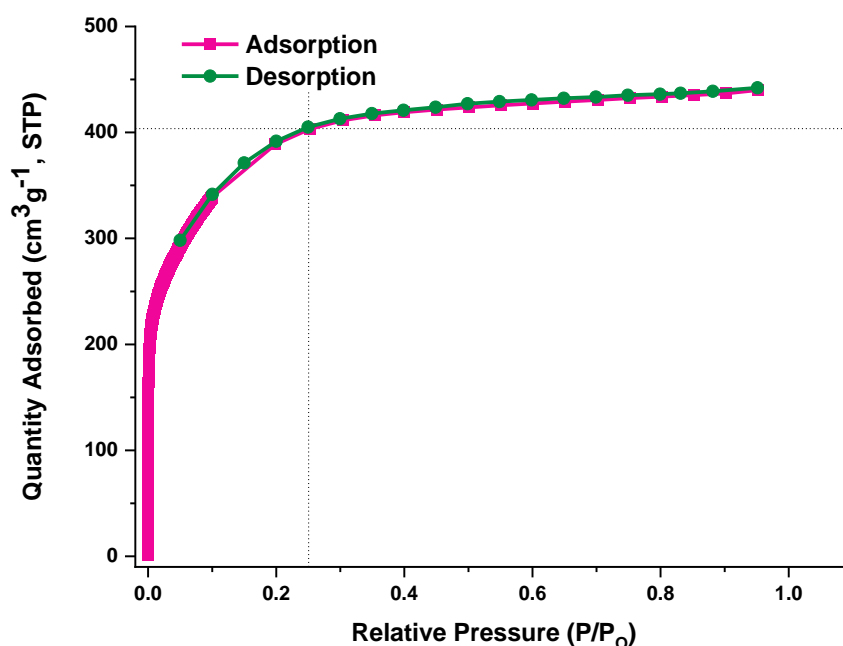
Source: author (2022)

The diffusion of the ions in the pores depends on the pore size. Thus, inaccessible pores do not contribute to both double-layer capacitance and energy density [138]. Previous studies suggested that pore size smaller than 0.5 nm is inaccessible to hydrated ions [139,41]. The technique applied for pore size distribution (Figure 35) does not show any information about pores smaller than 1 nm due to the penetration limit of N_2. Regardless of the limitation, an ascending line in the region of pore width smaller than 1 nm possibly indicates the presence of said micropores [61]. The pore size distribution curve, determined by the density functional theory (DFT) method, shows a maximum pore width of 3.15 nm. As reported in the literature, a small number of pores, wider than 2 nm, increase the

power density of SCs [140]. These small mesopores facilitate the access of electrolyte ions into the electrode surface. Furthermore, most pores of the ACFF sample vary in size from 1 to 2 nm with a modal distribution of 1.2 nm. The pore size distribution of ACFF sample is analogous to that of PAN-based activated-carbon materials reported in previous studies [96,95,63]. Additionally, the volume of micropores (0.69 cm^3 g^{-1}) in the ACCF sample is equivalent to 87% of the total volume of pores (0.79 cm^3 g^{-1}), confirming high microporosity (Table 14). In comparison to previous works [96,65,95], the volume of micropores and the total volume of pores are about 1.3 times greater.

Figure 35 - Pore size distribution of activated carbon fiber-felt (ACFF) sample A3
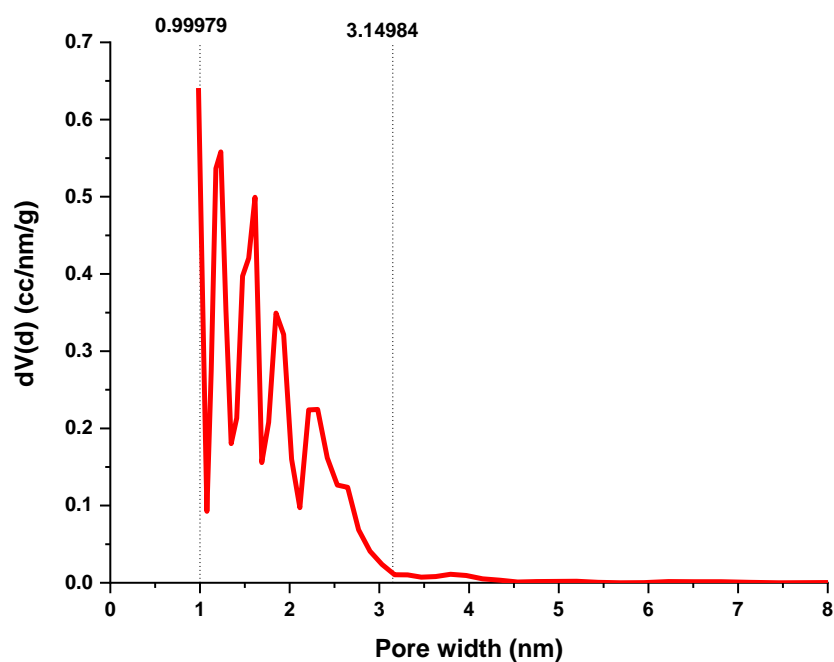
Source: author (2022)

Table 14 - Textural properties of activated carbon fiber-felt (ACFF) sample A3

Specific surface area (S$_{BET}$)	1875 m^2 g^{-1}
Pore volume (V$_{0.98}$)	0.79 cm^3 g^{-1}
Micropore volume (V$_{DFT}$)	0.69 cm^3 g^{-1}

Source: author (2022)

5.3.2. Morphological properties of ACFF electrodes

Secondary electrons SEM images of ACFF sample A3, with four different magnifications, can be seen in Figures 36 – 39. Figure 36 shows an overview of the ACFF sample A3. The filaments of the sample are continuous and laid in a random manner, which are common properties of a matted non-woven fabric, such as felt [141]. The filaments have a nearly cylindrical shape with a solid bean-type cross-section and a diameter of approximately 15 µm (Figure 37). The absence of cracks, macropores, longitudinal grooves, or major defects on the surface of the sample suggests homogeneity of the surface (Figure 38). The overall surface of the filaments is relatively smooth, apart from slight imperfections distributed randomly, as can be seen in Figure 39. Even though the ACFF sample A3 has high microporosity (pores < 3 nm) and a high adsorption capacity, surface porosity could not be observed in the SEM image due to the resolution limitations of SEM [142]. The secondary electron SEM image of ACFF sample is analogous to that of PAN-based activated-carbon materials reported in previous studies [95,96].

Figure 36 - Secondary electron SEM image of activated carbon fiber-felt (ACFF) sample A3. Image magnifications at 150x.
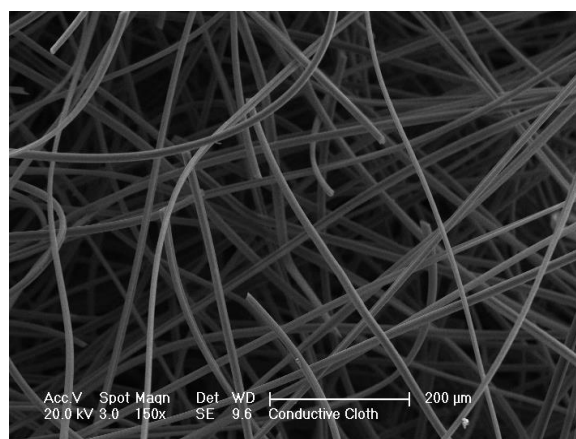
Source: author (2022)

Figure 37 - Secondary electron SEM of activated carbon fiber-felt (ACFF) sample A3. Image magnifications at 1000x.
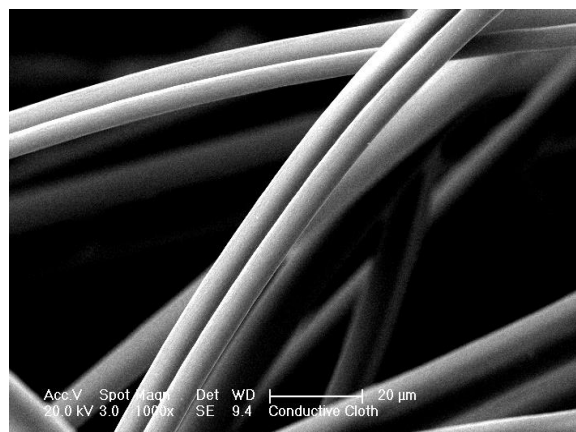
Source: author (2022)

Figure 38 - Secondary electron SEM image of activated carbon fiber-felt (ACFF) sample A3. Image magnifications at 2000x.
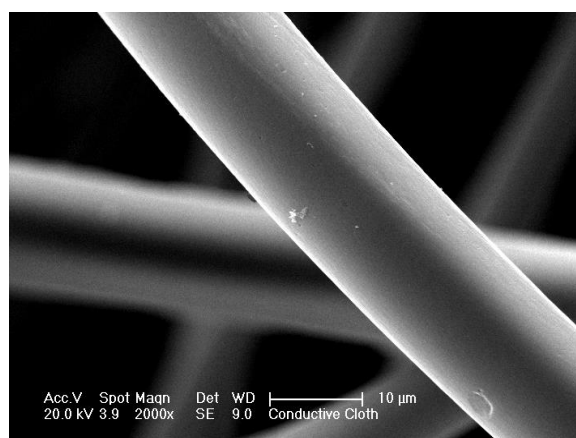
Source: author (2022)

Figure 39 - Secondary electron SEM image of activated carbon fiber-felt (ACFF) sample A3. Image magnifications at 16000x.
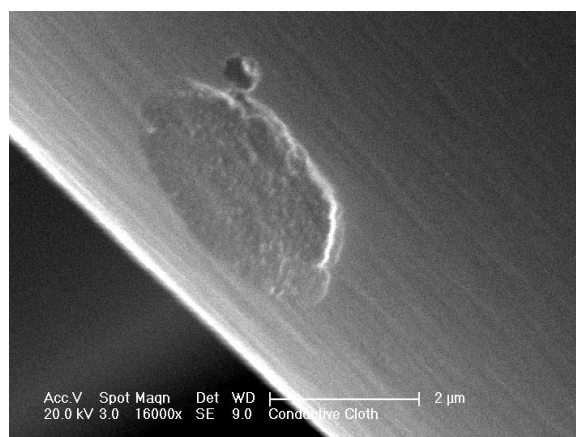
Source: author (2022)

5.3.3. Structural properties of ACFF electrodes

The Raman spectrum for carbon-based materials, amorphous or crystalline, exhibits two well-defined peaks commonly assigned as D and G bands. The D band, also known as the disorder/defect band, exhibits a peak at nearly 1380 cm^{-1}. The G band, crystalline graphite, exhibits a peak at nearly 1580 cm^{-1} due to the C-C bond-stretching of all pairs of sp^2 atoms in both rings and chains [143]. The Raman spectra of ACFF sample A3, in five different regions, are shown in Figure 38. In all regions, the spectra exhibited the same appearance. There are two very broad peaks located in the range of 1244 – 1710 cm^{-1}. The first peak, located at 1342 cm^{-1}, is referred to "D". The second peak, located at 1598 cm^{-1} is referred to "G". The spectra of ACFF sample A3 are very similar to that of PAN-based activated-carbon materials reported in previous studies [63,96,64].

Figure 40 - Raman spectra obtained in five different regions of the activated carbon fiber-felt (ACFF) sample A3.
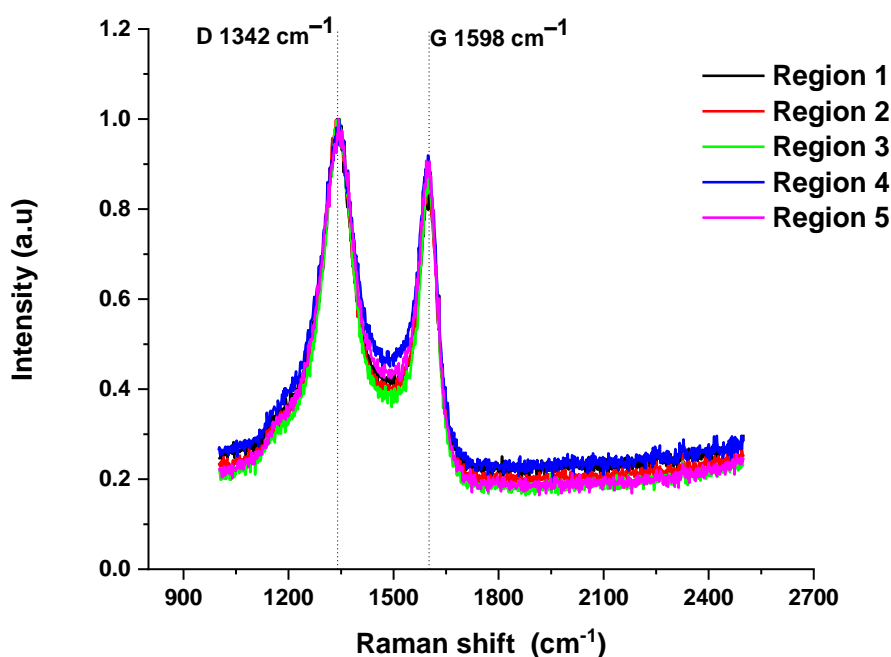
Source: author (2022)

X-ray diffraction (XRD) diffractograms of ACFF sample A3 can be seen in Figure 41 (powdered sample) and Figure 42 (felt sample). Two broad humped peaks that suggest

a carbon material with low crystallinity can be seen in both XRD diffractograms. The first peak, which is the most intense, is observed at approximately 2θ=17,6° and 2θ=18,4°, respectively. The second peak, which is a peak of weak intensity, is observed at approximately 2θ=42,6° and 2θ=43,4°, respectively. The diffractograms of ACFF sample A3 are analogous to that of PAN-based activated-carbon materials reported in previous studies [96,64,95].

Figure 41 - X-ray diffraction (XRD) diffractograms of the activated carbon fiber-felt (ACFF) sample A3 as a powder.
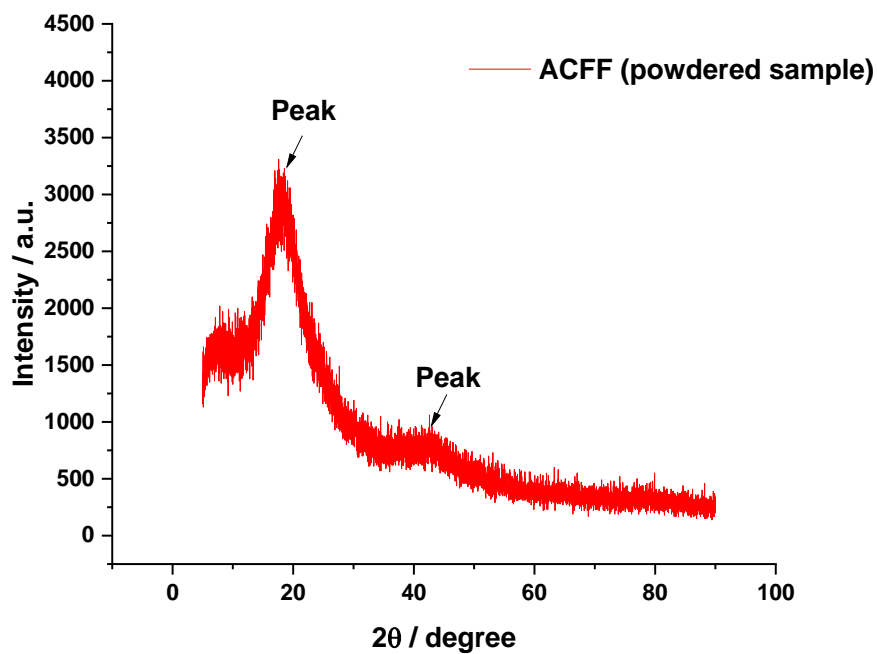
Source: author (2022)

Figure 42 - X-ray diffraction (XRD) diffractograms of the activated carbon fiber-felt (ACFF) sample A3 as a felt.
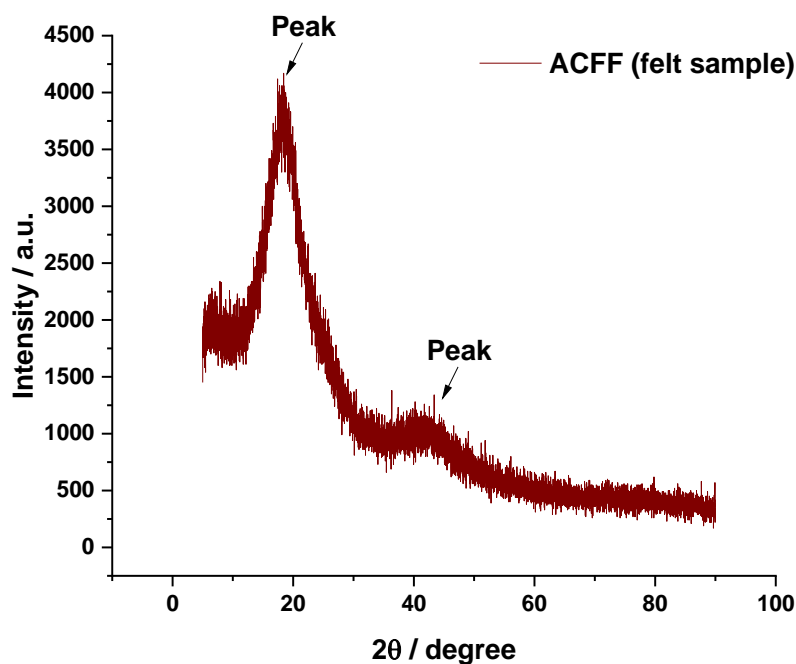
Source: author (2022)

5.4. Production and properties of ACFF-based electrodes: highlights

- The parameters of physical activation (residence time and oxidizing agents) influenced the yield, mass loss, shrinkage, burn-off percentage, moisture content, adsorption capacity, packing density, the PZC, and surface functional groups of the samples.

- The parameters of physical activation did not influence the pH value.

- Physical activation A3, carried out in CO_2 (200 sccm) + H_2O (12ml) and 60 min of residence time, resulted in high burn-off percentage, high shrinkage, high mass loss, and low yield.

- All samples are weak alkalis.

- Sample A3 had the highest moisture content percentage, packing density, adsorption capacity, microporosity, and estimated surface area.

- Sample A3 has an adsorption-desorption isotherm classified as Type I (microporous character), a high specific surface area of 1875 m^2 g^{-1}, a

maximum pore width of 3.15 nm, and most pores vary in size from 1 to 2 nm with a modal distribution of 1.2 nm.

- The volume of micropores in the ACCF sample A3 is equivalent to 87% of the total volume of the pores.

- Sample A3 has more functional groups on its surface (basic and acidic groups such as phenolic and carbonyl) and an acidic behavior for aqueous application.

- Sample A3 has low crystallinity.

- Sample A3 is relevant for supercapacitors applications as electrodes in aqueous electrolytes.

- The filaments of the fiber-felt sample are continuous and laid in a random manner. In addition, the filaments have a nearly cylindrical shape with a solid bean-type cross-section and a diameter of approximately 15 µm. The surface is homogeneous and smooth without major defects.

5.5. Properties of ACFF-based EDLC cells

As discussed in the previous section, ACFF sample A3 seems relevant for application as electrodes. The active mass of two parallel electrodes and the active mass loading for all ACFF-based EDLC cells can be seen in Table 15. It was reported in the literature that the mass loading of commercialized activated carbon electrodes is approximately 10 mg cm^{-2} [110]. Furthermore, a mass loading of at least 5 mg cm^{-2} is suggested for evaluating the performance of supercapacitors [127]. In this work, all ACFF-based EDLC cells have an active mass loading greater than 5 mg cm^{-2}. As capacitance arises from each electrode, a mass balance between the two electrodes was taken into consideration.

Table 15 - Active mass of two parallel electrodes and active mass loading of the electrodes for different ACFF-based EDLCs.

ACFF-based EDLC cell		Active mass (mg)	Active mass loading (mg cm^{-2})
Aqueous electrolytes	1 M H$_2$SO$_4$	5.8 ± 0.6	11.6 ± 1.2
	2 M H$_2$SO$_4$	5.3 ± 0.5	10.6 ± 1.1
	1 M KOH	8.4 ± 0.8	16.8 ± 1.7
	2 M KOH	6.6 ± 0.7	13.2 ± 1.3
Glycerol-based electrolytes	KOH:GLY (1:3)	6.4 ± 0.6	12.8 ± 1.3
	KOH:GLY (1:2)	5.3 ± 0.5	10.6 ± 1.1
	KOH:GLY (1:1)	6.0 ± 0.6	12.0 ± 1.2
	KOH:GLY (2:1)	6.9 ± 0.7	13.8 ± 1.4
	KOH:GLY (3:1)	8.3 ± 0.8	16.6 ± 1.7
	ChCl:GLY (3:1)	4.6 ± 0.5	9.2 ± 0.9
	K$_2$CO$_3$:GLY (3:1)	5.0 ± 0.5	10.0 ± 1.0

Source: author (2022-2023)

5.6. Electrochemical performance of ACFF-based EDLC cells: Voltammograms

The voltammograms for acidic and alkaline aqueous electrolytes are shown in Figures 43 - 44, respectively, whereas the voltammograms for glycerol-based electrolytes are shown in Figures 45 - 46. The variation of gravimetric capacitance in acidic and alkaline aqueous electrolytes as a function of the scan rate can be seen in Figure 47. In Figures 48 - 49, capacitance, and gravimetric capacitance of ACFF-based EDLCs in aqueous and glycerol-based electrolytes are shown.

The response of all voltammograms indicates that the charge storage mechanism of ACFF electrodes in aqueous electrolytes and in glycerol-based electrolytes is primarily electrostatic (non-faradaic). At the beginning of the CV curve (0.0 V) in acidic and alkaline aqueous electrolytes (Figures 43 - 44), the sharp increase in the current occurs due to the rapid formation of the electric double-layer (EDL) and possibly due to a negligible equivalent series resistance (ESR) [116]. As a result, nearly rectangular CV

curves with slight blunt corners are shown. Current seems constant over the whole potential window in acidic aqueous electrolytes (Figure 43). In the case of alkaline aqueous electrolytes (Figure 44), current seems constant over the potential window until the peak at the edge of the CV curve at high potentials (0.6 - 1V) due to electrolyte degradation [116,113]. The narrow potential window of aqueous electrolytes ($\approx$ 1 V), due to water electrolysis, is a drawback since it limits energy density and restricts the amount of energy stored [144].

Figure 43 - CV curves of ACFF-based EDLC cells at room temperature and at a scan rate of 1 mV s^{-1} in acidic aqueous electrolytes
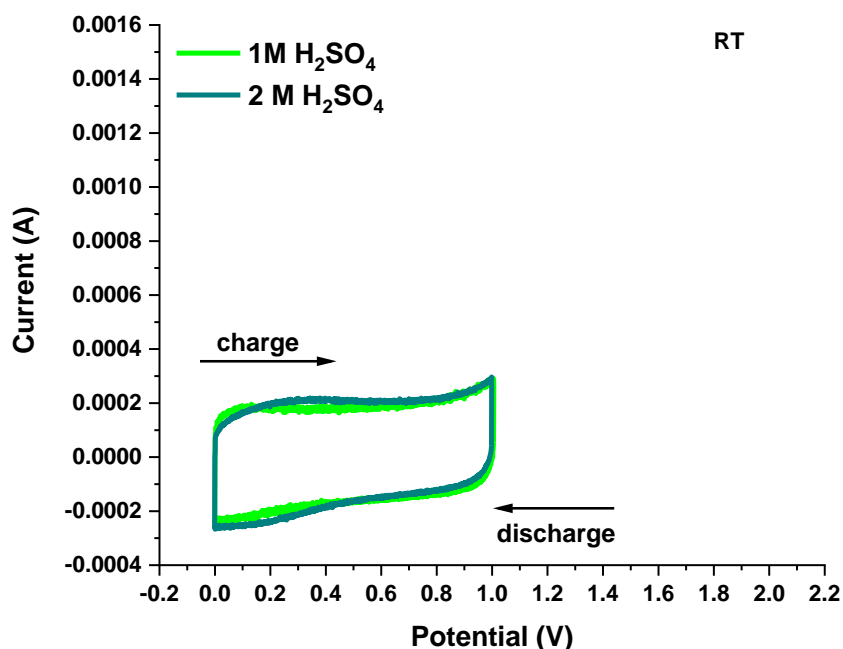
Source: author (2021-2022)

Figure 44 - CV curves of ACFF-based EDLC cells at room temperature and at a scan rate of 1 mV s^{-1} in alkaline aqueous electrolytes
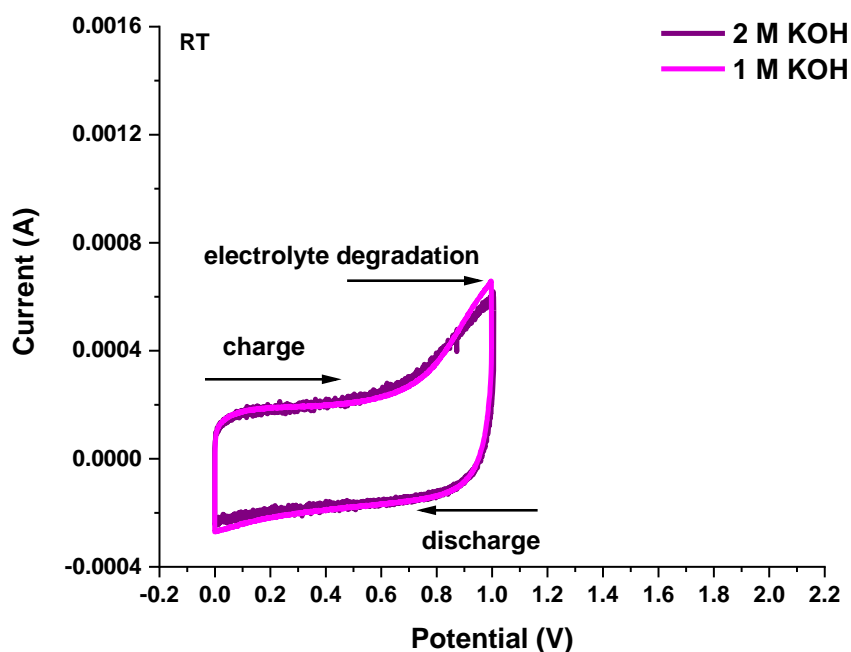
Source: author (2021-2022)

The voltammogram for KOH:GLYs with variation in molar ratio can be seen in Figure 45. Due to a less distorted CV curve in the increase in the current at the potential of 0.0 V, the formation of the electric double-layer seems to occur faster in KOH:GLY (3:1). Current appears constant over the whole potential window in KOH:GLY (3:1), resulting in nearly rectangular CV curves with slight blunt corners. The increase in the current at the potential of 0.0 V in the CV curves of KOH:GLY (2:1) and KOH:GLY (1:1) are not as sharp as the CV curve of KOH:GLY (3:1), suggesting a more resistive behavior. Furthermore, electrolyte degradation occurs at high potential (1.2 – 2.1 V) in KOH:GLYs at molar ratios of 2:1 and 1:1. Electrolyte degradation may have occurred due to water content as both components of the glycerol-based electrolytes are hygroscopic. The CV curves of KOH:GLY at molar ratios of 1:2 and 1:3 deviate from the CV profile expected in addition to smaller CV areas, resulting in low capacitance.

Figure 45 - CV curves of ACFF-based EDLC cells at room temperature and at a scan rate of 1 mV s^{-1} in glycerol-based electrolytes: KOH:GLYs with variation in molar ratio
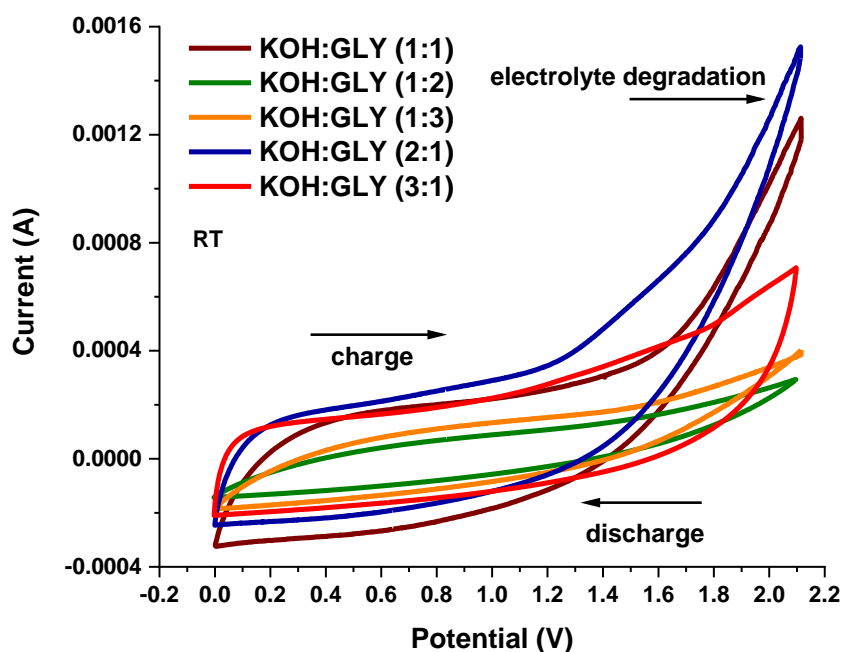
Source: author (2022)

The voltammogram for glycerol-based electrolytes K_2CO_3:GLY (3:1) and ChCl:GLY (3:1) can be seen in Figure 46. Due to the sharp increase in the current at the beginning of the CV curve (0.0 V), it is inferred that the formation of the electric double-layer occurs more rapidly in ChCl:GLY (3:1) in comparison to KOH:GLYs and K_2CO_3:GLY (3:1). The CV curves of K_2CO_3:GLY (3:1) are more distorted and the CV area is much smaller than that of ChCl:GLY (3:1), suggesting that K_2CO_3:GLY (3:1) has a more resistive than capacitive behavior. Moreover, electrolyte degradation at high potential (1.3 – 2.1 V) may have occurred due to the hygroscopic properties of glycerol and both solid compounds (K_2CO_3 and $C_5H_{14}ClNO$).

Figure 46 - CV curves of ACFF-based EDLC cells at room temperature and at a scan rate of 1 mV s^{-1} in glycerol-based electrolytes: K_2CO_3:GLY (3:1) and ChCl:GLY (3:1)
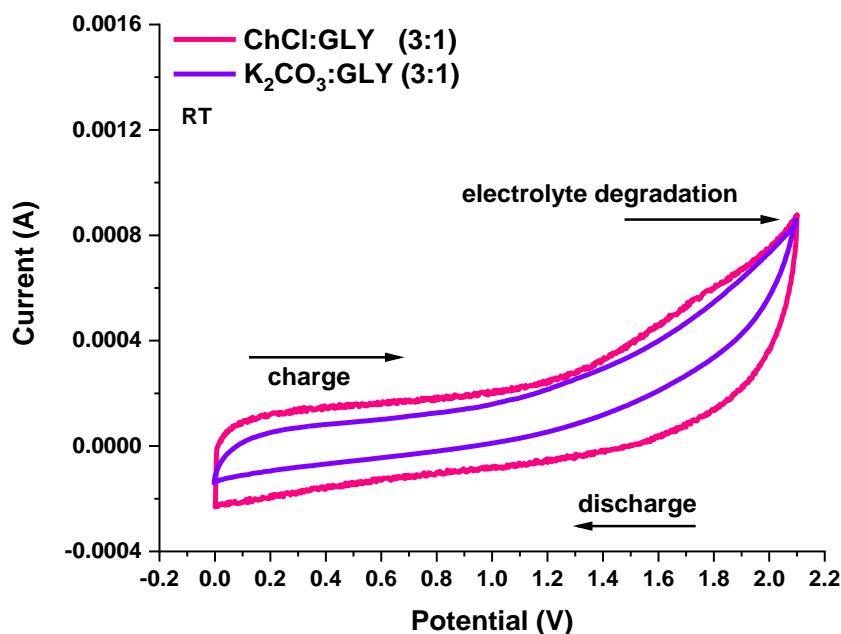
Source: author (2022-2023)

The absence of oxidative and reductive (redox) peaks in the CV curves of ACFF-based EDLCs, in aqueous electrolytes, and in glycerol-based electrolytes, suggests that there is no significant contribution from faradaic reactions [145]. Nevertheless, previous literature reported that carbon-based electrodes possibly exhibit 1 – 5 % of their capacitance as surface-redox pseudocapacitance due to reversible faradaic-redox reactions of active surface functional groups [146]. A previous work [63], produced a similar electrode material through a two-step oxidation process. The results of the XPS analysis showed that the oxygen and the nitrogen groups found in the textile PAN-based electrode are 3.86 % and 1.36 % in mass, respectively. As explained previously, oxidation time affects the surface chemistry of activated carbon-based materials leading to enhanced capacitance. A Previous study mentioned that in addition to EDL capacitance, limited pseudocapacitance may arise from carbon-based electrodes in H_2SO_4 electrolytes [45]. In this work, the occurrence of a minor surface-redox pseudocapacitive behavior could be verified and better investigated with a three-electrode cell, at a low scan rate, instead of a two-electrode cell [113].

As can be seen in Figure 47, gravimetric capacitance increases as the scan rate decreases. At fast scan rates (> 10 mV s^{-1}), there is not enough time for the electrolyte ions to move into accessible pores decreasing the size of the diffusion layer and resulting in decreased gravimetric capacitance [147]. For a better understanding of the electrochemical behavior and to acquire increased gravimetric capacitance, slow scan rates are suggested. At scan rates ranging from 1 mV s^{-1} to 100 mV s^{-1}, gravimetric capacitance deviation is lower in H_2SO_4 electrolytes (22 % – 24%) and in KOH 2 mol L^{-1} (27%). The results highlight that said electrolytes have satisfactory capacitance stability as a function of the scan rate. Even though the highest capacitance deviation was found in KOH 1 mol L^{-1} (47%), its capacitance stability is superior to that of a previous study about activated carbon electrodes derived from Areca catechu husk [43]. The gravimetric capacitance in KOH 1 mol L^{-1} reduced by around 70.4% at scan rates ranging from 1 mV s^{-1} to 10 mV s^{-1}, while in this study, it reduced by only 17%.

Figure 47 - Variation of gravimetric capacitance in acidic and alkaline aqueous electrolytes as a function of the scan rate
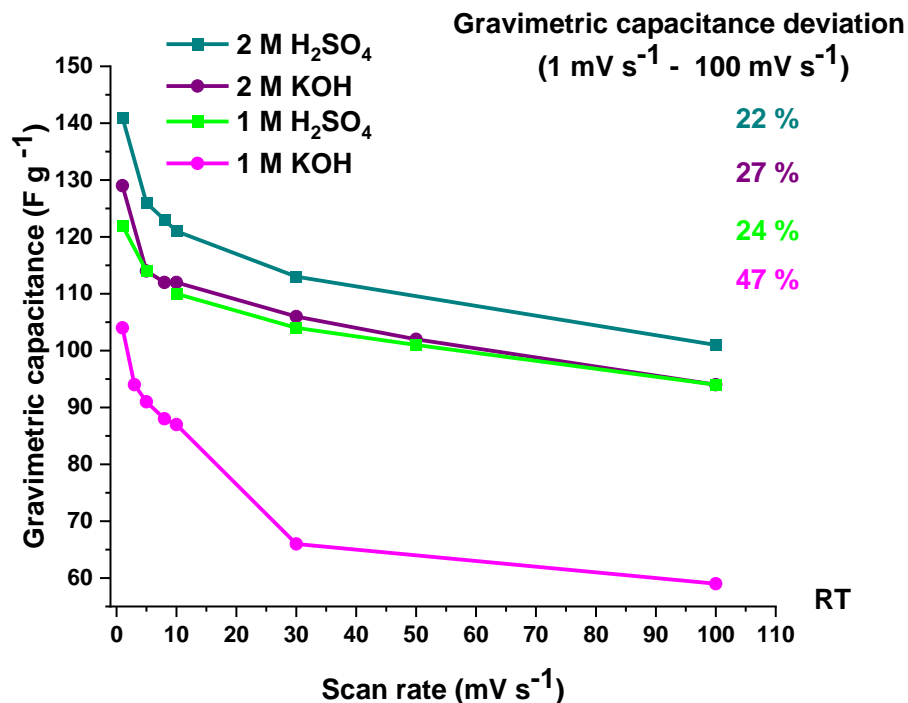
Source: author (2021-2022)

Figure 48 shows the capacitance value and the corresponding gravimetric capacitance of ACFF electrodes in acidic and in alkaline aqueous electrolytes, while Figures 49 and 50 shows the capacitance value and the corresponding gravimetric capacitance in glycerol-based electrolytes. The gravimetric capacitance of commercial SCs, which consists of activated carbon electrodes in organic electrolytes, is commonly 100 F g^{-1} [127]. All ACFF-based EDLC cells in aqueous electrolytes have a gravimetric capacitance exceeding 100 F g^{-1} (Figure 48). Among glycerol-based electrolytes, KOH:GLY (2:1), KOH:GLY (1:1), and ChCl:GLY (3:1) have a gravimetric capacitance that is greater than 100 F g^{-1} (Figures 49 - 50).

In acidic electrolytes, the highest gravimetric capacitance of 141 ± 14 F g^{-1}, at a scan rate of 1 mV s $^{-1}$, was found in H_2SO_4 2 mol L^{-1} (Figure 48). The results demonstrated that capacitance and its corresponding gravimetric capacitance increased as a function of the molarity in acidic aqueous electrolytes. In alkaline aqueous electrolyte, the highest gravimetric capacitance of 129 ± 13 F g^{-1}, at a scan rate of 1 mV s $^{-1}$, was found in KOH 2 mol L^{-1}. Although the highest capacitance of 0.22 ± 0.02 F was found in KOH 1 mol L^{-1}, it resulted in a lower gravimetric capacitance of 104 ± 10 F g^{-1} when normalized by the active mass of both electrodes.

The application of textile PAN-based fibers as electrodes for supercapacitors is still very limited and there have not been many studies on this subject, making it difficult to find sufficient data to compare. The gravimetric capacitance of ACFF-based EDLC in H_2SO_4 2 mol L^{-1} is analogous to that of a previous study about activated carbon derived from Areca catechu husk [43]. Nevertheless, the gravimetric capacitance is smaller than that of a study about PAN-based fibers in H_2SO_4 4 mol L^{-1} using a three-electrode cell setup [65]. The gravimetric capacitance of ACFF-based EDLC in KOH 1 mol L^{-1} is greater than those of commercial activated carbon [74] and activated carbon without vacuum heat treatment [73]. However, the gravimetric capacitance is smaller than those of activated carbon with vacuum heat treatment [73] and activated carbon derived from Areca catechu husk [43]. Moreover, the gravimetric capacitance of ACFF-based EDLC in KOH 2 mol L^{-1} is greater than that of commercial activated carbon [74].

Figure 48 - Capacitance and its corresponding gravimetric capacitance of ACFF-based EDLC cells in acidic and alkaline aqueous electrolytes at room temperature and at a scan rate of 1 mV s^{-1}
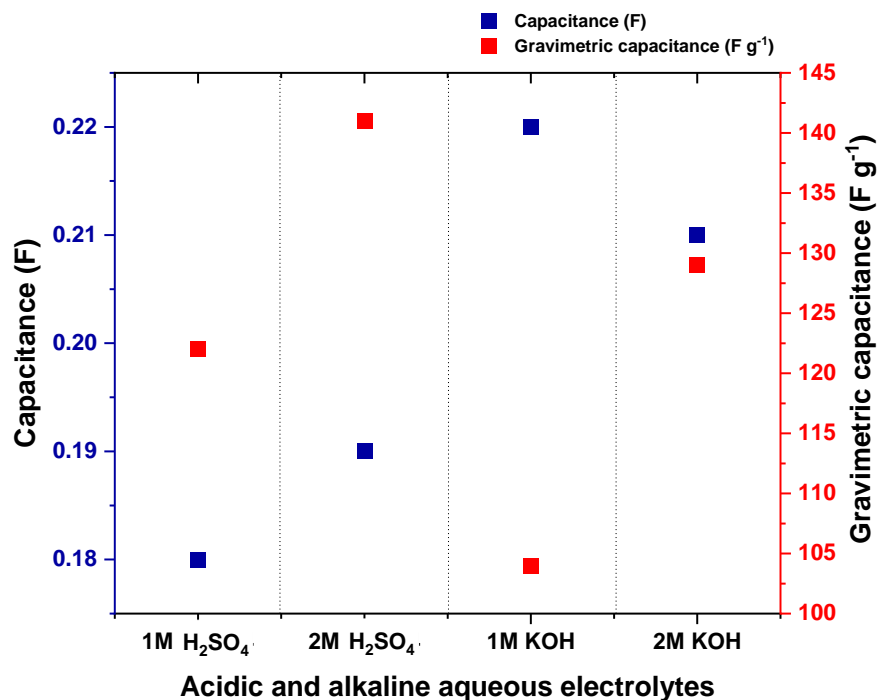
Source: author (2021-2022)

The influence of the salt-to-solvent ratio in glycerol-based electrolytes can be seen in Figure 49. Although KOH:GLY (1:2) and KOH:GLY (1:3) are less viscous and more wettable (Figure 21), it resulted in low capacitance (< 0.02 F) and low gravimetric capacitance (< 50 F g^{-1}). The process of electrolyte diffusion at room temperature, developed for the cell assembly, helped to decrease the viscosity and to improve the wettability of KOH:GLYs at molar ratios of 3:1, 2:1, and 1:1, resulting in higher capacitance (> 0.15 F) and higher gravimetric capacitance (> 80 F g^{-1}). The capacitance of KOH:GLY (3:1), KOH:GLY (2:1), and KOH:GLY (1:1) is similar: 0.17 F, 0.18 F, and 0.16 F, respectively. When normalized by the active mass of both electrodes, gravimetric capacitance varies from 82 F g^{-1} to 104 F g^{-1}. Taking into consideration the response of the CV profiles shown in the voltammogram in Figure 45, KOH:GLY (3:1) has rectangular CV curves that are less distorted, resulting a better capacitive behavior. Capacitance was overestimated in both KOH:GLY (2:1) and KOH:GLY (1:1) due to the contribution of the additional long tail in the CV profile (electrolyte degradation) as the whole area under the curve was used in the calculation.

Figure 49 - Capacitance and its corresponding gravimetric capacitance of ACFF-based EDLC cells in glycerol-based electrolytes: KOH:GLYs with variation in molar ratio
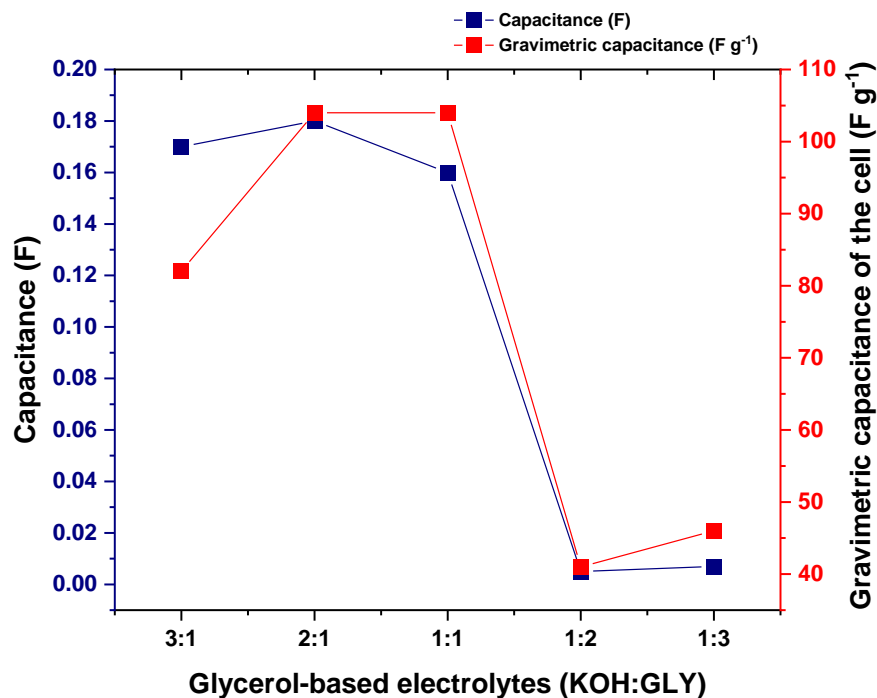
Source: author (2022)

Among all glycerol-based electrolytes, the highest gravimetric capacitance of 142 $\pm$ 14 F g^{-1} (Figure 50) was found in ChCl:GLY (3:1). The result is analogous to that of H$_2$SO$_4$ 2 mol L^{-1}. Due to a smaller CV area, a gravimetric capacitance of 76 $\pm$ 8 F g^{-1} was found in K$_2$CO$_3$:GLY (3:1).

In terms of gravimetric capacitance, all ACFF-based EDLCs in glycerol-based electrolytes outperformed the gravimetric capacitance of an EDLC in polymer electrolyte plasticized with glycerol [10]. Nevertheless, ACFF-based EDLCs in KOH:GLYs at molar ratios of 3:1, 2:1, and 1:1 did not outperform the EDLCs in glycerol-based ionic-liquid electrolytes reported in previous work [74]. In comparison to the findings of a previous study [74], the gravimetric capacitance of ACFF-based EDLCs in ChCl:GLY (3:1) is twice greater, whereas it is about thirty-eight times greater in K$_2$CO$_3$:GLY (3:1).

Figure 50 - Capacitance and its corresponding gravimetric capacitance of ACFF-based EDLC cells in glycerol-based electrolytes: K_2CO_3:GLY (3:1) and ChCl:GLY (3:1)
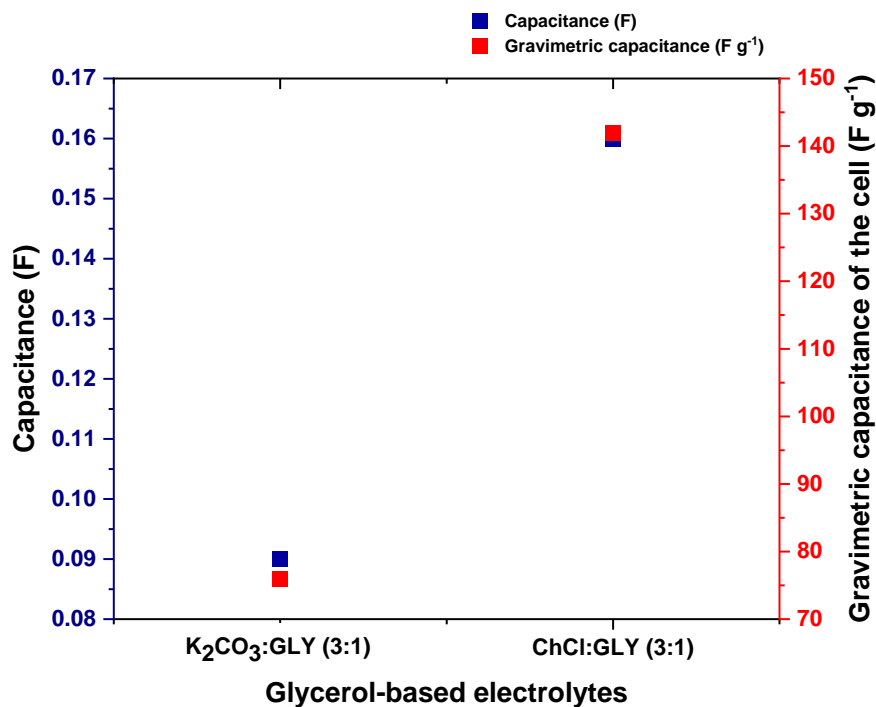
Source: author (2023)

5.7. Electrochemical performance of ACFF-based EDLC cells: Nyquist plots

The zoom-in view of the Nyquist plots for ACFF-based EDLCs in acidic and alkaline aqueous electrolytes can be seen in Figures 51 - 52, respectively, whereas the zoom-in view of the Nyquist plots for glycerol-based electrolytes can be seen in Figures 53 - 57. The variation of gravimetric capacitance as a function of frequency can be seen in Figures 58 (aqueous electrolytes) and in Figure 59 (glycerol-based electrolytes). The overview of Nyquist plot for ACFF-based EDLCs in acidic and alkaline aqueous electrolytes is shown in Figure 60, whereas the Nyquist plots for glycerol-based electrolytes are shown in Figures 61 and 62. All Nyquist plots are represented in a one-to-one ratio.

Bulk electrolyte resistance, interfacial impedance, and impedance of pores can be observed in the zoom-in view of the Nyquist plots for ACFF-based EDLCs. As can be seen in Figure 51, the bulk electrolyte resistance (R_e) of 1.7 ± 0.2 Ω found in H_2SO_4 1

mol L^{-1} is analogous to that of H$_2$SO$_4$ 2 mol L^{-1} (1.8 ± 0.2 Ω). However, the difference in molarity influenced the bulk electrolyte resistance (R$_e$) of alkaline aqueous electrolytes (Figure 52). The lowest bulk electrolyte resistance (R$_e$) in aqueous electrolytes was found in KOH 2 mol L^{-1} (0.9 ± 0.1 Ω), while the highest R$_e$ was found in KOH 1 mol L^{-1} (4.0 ± 0.4 Ω).

The difference in molarity seems to influence the interfacial impedance and impedance of pores in acidic and alkaline aqueous electrolytes. Although semicircles are not noticeable at a medium frequency in acidic aqueous electrolytes, they are visible in both concentrations of alkaline aqueous electrolytes. The diameter of the semicircle observed in KOH 2 mol L^{-1} is 0.38 ± 0.04 Ω, whereas in KOH 1 mol L^{-1} is 0.53 ± 0.05 Ω. It is arguable whether the semicircles recorded in the Nyquist plots were caused by interfacial contact resistance at the current collector / active material or by charge transfer resistance (R$_{ct}$) due to the presence of functional groups on the surface of the carbon materials. A previous study [114], proposed carrying out the EIS test at multiple potentials to confirm the presence of charge transfer resistance. R$_{ct}$ is said to vary with potential, whereas interfacial impedance at the current collector / active material remains constant across all potentials [114]. In this work, EIS measurements were carried out without the variation of potential.

In acidic aqueous electrolytes, the 45° line observed on the curve of H$_2$SO$_4$ 2 mol L^{-1} has a steep incline, whereas the curve of H$_2$SO$_4$ 1 mol L^{-1} has a more gradual incline. In alkaline aqueous electrolytes, the 45° line observed on the curve of KOH 2 mol L^{-1} has a steep incline, whereas the curve of KOH 1 mol L^{-1} has a gentle incline. The resistance associated with the intra-particle pores was deduced using the 45° line. The lowest resistance of pores 0.09 ± 0.01 Ω was found in H$_2$SO$_4$ 2 mol L^{-1}, whereas the highest resistance of pores 0.72 ± 0.07 Ω was found in KOH 1 mol L^{-1}. It can be deduced that the ion diffusion into the pores and the development of the EDL occur rapidly in H$_2$SO$_4$ 2 mol L^{-1}, followed by KOH 2 mol L^{-1} and H$_2$SO$_4$ 1 mol L^{-1}.

In an ideal EDLC, capacitance is constant over the applied frequency range, thus the electrode surface is entirely impregnated [125,121,116]. The more the vertical line leans towards the y-axis, the better the capacitive behavior [126]. A nearly vertical line, which is typical for porous electrodes [114], parallel or close to parallel to the y-axis can be observed in the low-frequency region of the Nyquist plot for all aqueous electrolytes (Figs. 51 and 52), confirming their capacitive behavior.

Figure 51 - Zoom-in view of Nyquist plot of an ACFF-based EDLC at room temperature and an applied potential of 0 V in acidic aqueous electrolytes
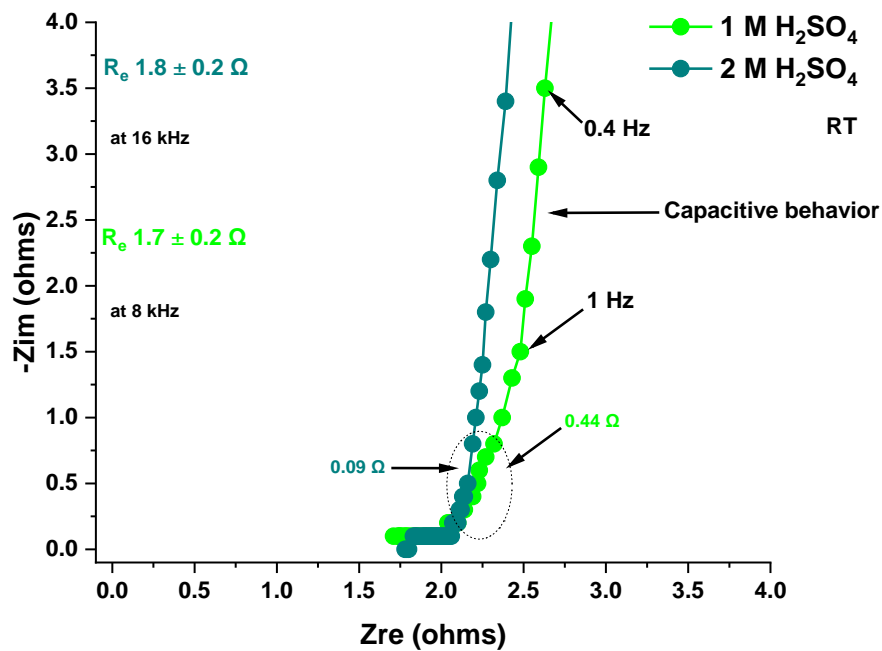
Source: author (2021-2022)

Figure 52 - Zoom-in view of Nyquist plot of an ACFF-based EDLC at room temperature and an applied potential of 0 V in alkaline aqueous electrolytes
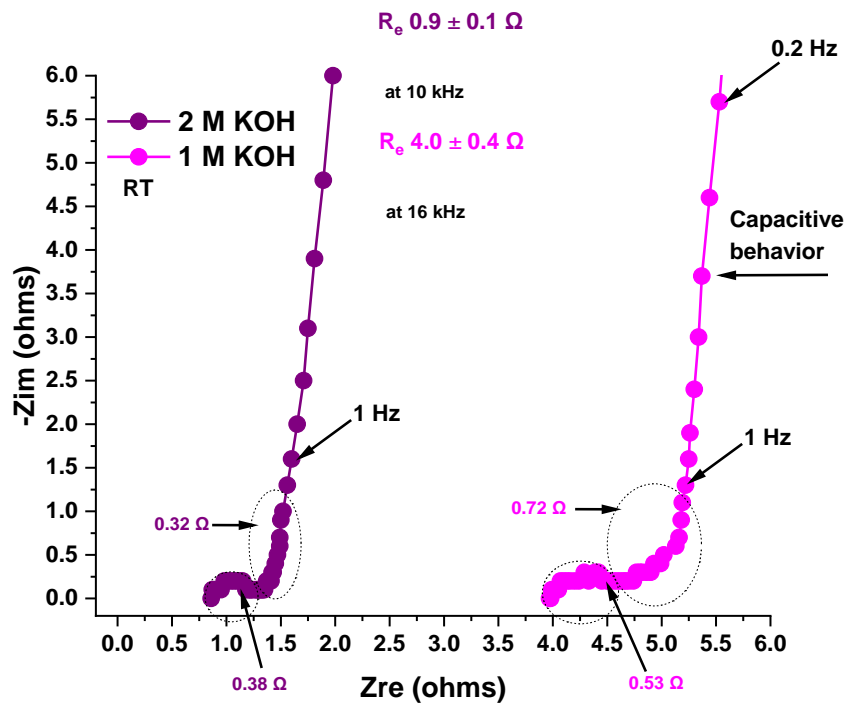
Source: author (2021-2022)

In comparison to aqueous-based electrolytes, glycerol-based electrolytes have high bulk electrolyte resistance. Among KOH:GLYs (Figures 53 - 55), the lowest bulk electrolyte resistance (R_e) of 35 ± 4 Ω was found in KOH:GLY (3:1), which coincides well with the nearly rectangular-shaped CV curves shown previously in Figure 45. On the other hand, the R_e of KOH:GLYs at molar ratios of 2:1, 1:1, 1:2, and 1:3 exceeded 100 Ω. The Nyquist plots of KOH:GLYs at molar ratios of 1:2 and 1:3 deviate from the profile expected from an ideal EDLC as they have a more resistive behavior than capacitive. The salt-to-solvent ratio in KOH:GLYs not only influenced the bulk electrolyte resistance but also the ion diffusion into the pores and the development of the EDL. The slope (45°) in the curve of KOH:GLY (3:1) is less gradual than those of KOH:GLYs at molar ratios of 2:1, 1:1, 1:2, and 1:3, suggesting less resistance of pores. Moreover, among KOH:GLYs, the nearly vertical line close to parallel to the y-axis can be observed in the low-frequency region of the Nyquist plot for KOH:GLY (3:1), confirming a better capacitive behavior (Figure 53).

Figure 53 - Zoom-in view of Nyquist plot of an ACFF-based EDLC at room temperature and an applied potential of 0 V in glycerol-based electrolyte: KOH:GLY (3:1)

Source: author (2022)

Figure 54 - Zoom-in view of Nyquist plot of an ACFF-based EDLC at room temperature and an applied
potential of 0 V in glycerol-based electrolyte: KOH:GLY (2:1) and KOH:GLY (1:1)

Source: author (2022)

Figure 55 - Zoom-in view of Nyquist plot of an ACFF-based EDLC at room temperature and an applied
potential of 0 V in glycerol-based electrolyte: KOH:GLY (1:2) and KOH:GLY (1:3)

Source: author (2022)

As can be seen in Figure 56, the bulk electrolyte resistance (R_e) of 22 ± 2 Ω found in K_2CO_3:GLY (3:1) is about 1.5 times lower than the R_e found in KOH:GLY at a molar ratio of 3:1. Despite the fact that K_2CO_3:GLY (3:1) outperforms KOH:GLY (3:1) in terms of bulk electrolyte resistance, K_2CO_3:GLY (3:1) has a higher resistance of pores. The 45° line observed on the curve of K_2CO_3:GLY (3:1) has the most gradual incline among glycerol-based electrolytes, suggesting that the ion diffusion into the pores and the development of the EDL occur laboriously.

Figure 56 - Zoom-in view of Nyquist plot of an ACFF-based EDLC at room temperature and an applied potential of 0 V in glycerol-based electrolyte: K_2CO_3:GLY (3:1)

Source: author (2023)

As can be seen in Figure 57, among all glycerol-based electrolytes, the lowest bulk electrolyte resistance (R_e) of 5.0 ± 0.5 Ω was found in ChCl:GLY (3:1). The result is analogous to that found in KOH 1 mol L^{-1}. The slope (45°) in the curve of ChCl:GLY (3:1) is shorter and less gradual than those of KOH:GLYs and K_2CO_3:GLY (3:1), suggesting less resistance of pores. The nearly vertical line close to parallel to the y-axis seen in the low-frequency region of the Nyquist plot confirms its capacitive behavior. The

performance of ACFF-based EDLC in ChCl:GLY (3:1) is, among glycerol-based electrolytes, the most comparable to aqueous electrolytes. Due to a less resistive behavior, ion diffusion into the pores and the development of the EDL occurs rapidly in ChCl:GLY (3:1).

Figure 57 - Zoom-in view of Nyquist plot of an ACFF-based EDLC at room temperature and an applied potential of 0 V in glycerol-based electrolyte: ChCl:GLY (3:1)

Source: author (2023)

Figures 58 and 59 show the variation of gravimetric capacitance as a function of frequency. In aqueous electrolytes, H_2SO_4 2 mol L^{-1} had the highest gravimetric capacitance over the whole frequency range, whereas KOH 1 mol L^{-1} had the lowest gravimetric capacitance. At low frequencies ranging from 0.006 Hz to 1 Hz, the lowest gravimetric capacitance deviation was found in H_2SO_4 2 mol L^{-1} (19%), and the highest gravimetric capacitance deviation was found in KOH 1 mol L^{-1} (29%). Among all glycerol-based electrolytes, ChCl:GLY (3:1) had the highest gravimetric capacitance over the whole frequency range. At a low frequency of 1 Hz, the gravimetric capacitance of ChCl:GLY (3:1) is about ten times greater than that of KOH:GLY (3:1). At low frequencies ranging from 0.006 Hz to 1 Hz, the gravimetric capacitance deviation of

ChCl:GLY (3:1) is 48%, while KOH:GLY (3:1) has a gravimetric capacitance deviation of 94%. The results are in agreement with the Nyquist plots discussed in this section as ion diffusion and the development of the EDL occur rapidly in ChCl:GLY (3:1).

Figure 58 - Variation of gravimetric capacitance in acidic and alkaline aqueous electrolytes as a function of frequency
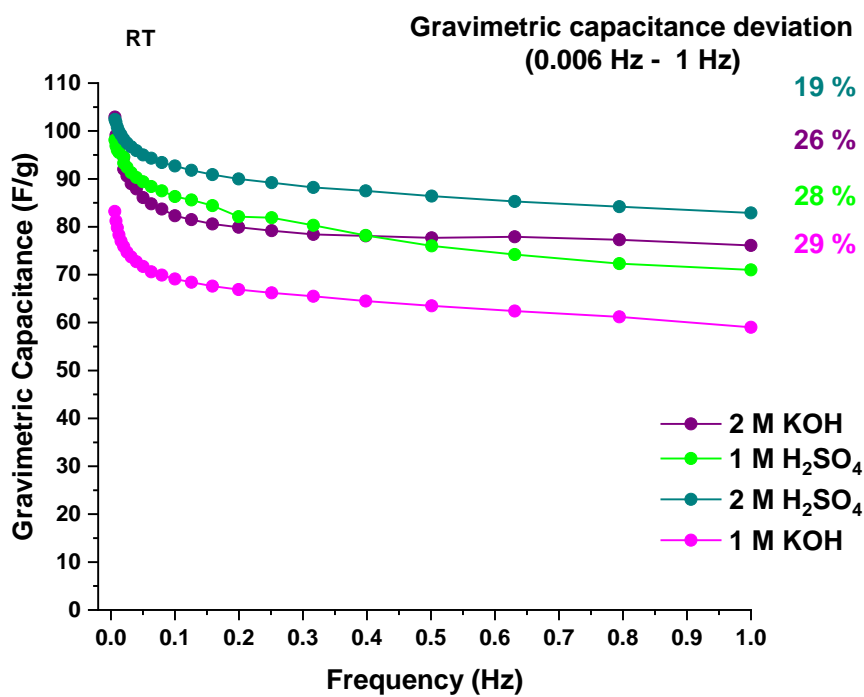
Source: author (2021-2022)

Figure 59 - Variation of gravimetric capacitance in glycerol-based electrolytes as a function of frequency
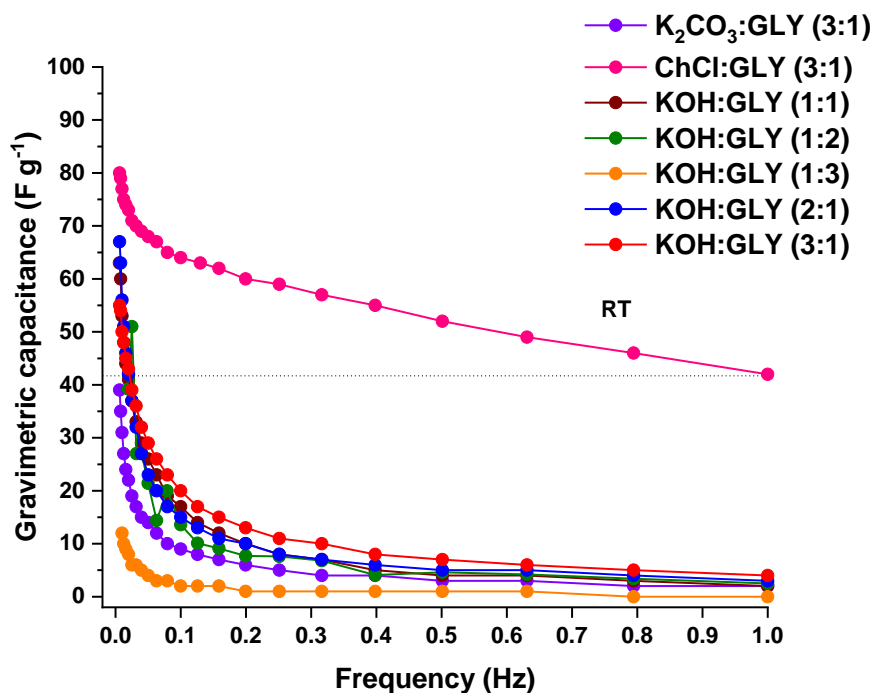
Source: author (2022-2023)

An overview of the Nyquist plots of aqueous electrolytes and glycerol-based electrolytes is shown in Figures 60 – 62. A nearly vertical line parallel or close to parallel to the y-axis can be observed in the following electrolytes: in all acidic and alkaline aqueous electrolytes, and in glycerol-based electrolytes such as KOH:GLY (3:1) and ChCl:GLY (3:1). Capacitance seems to be more consistent throughout the whole frequency window in H_2SO_4 2 mol L^{-1}, among aqueous electrolytes, and in ChCl:GLY (3:1), among glycerol-based electrolytes as the nearly vertical line of said electrolytes leans more towards the y-axis. At a low frequency of 0.006 Hz, the highest gravimetric capacitance of 102 ± 10 F g^{-1}, in acidic aqueous electrolytes, was found in H_2SO_4 2 mol L^{-1}. In alkaline aqueous electrolytes, the highest gravimetric capacitance of 103 ± 10 F g^{-1} was found in KOH 2 mol L^{-1}. Among glycerol-based electrolytes, the highest gravimetric capacitance of 80 ± 8 F g^{-1} was found in ChCl:GLY (3:1). Although high gravimetric capacitance was found in KOH:GLY (2:1) and KOH:GLY (1:1), these electrolytes have bulk electrolyte resistance exceeding 100 Ω and a higher possibility of

electrolyte degradation (see Figure 45), which are drawbacks. Among KOH:GLYs, a balance between capacitive and resistive behavior was found in KOH:GLY (3:1).

Figure 60 - Nyquist plot of ACFF-based EDLCs at room temperature and an applied potential of 0 V in acidic and alkaline aqueous electrolytes
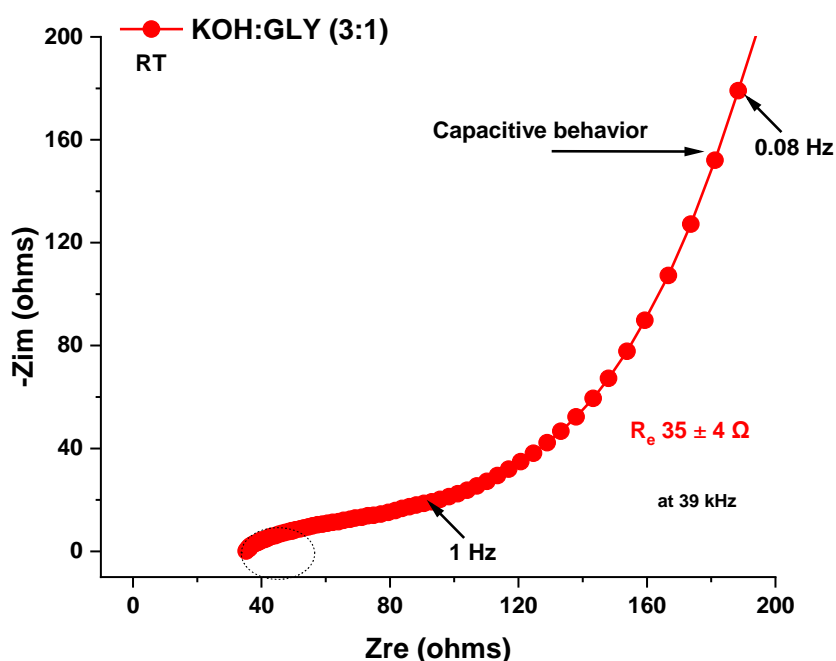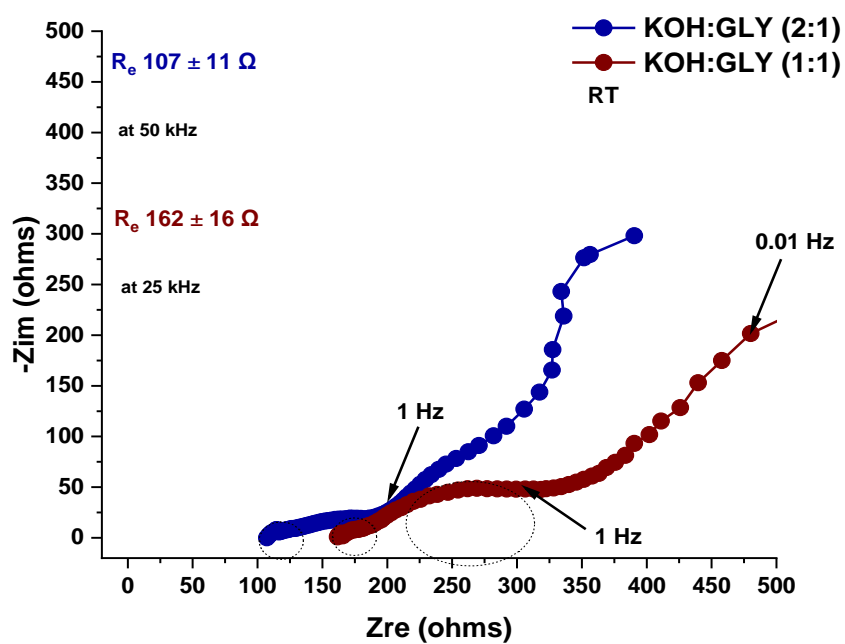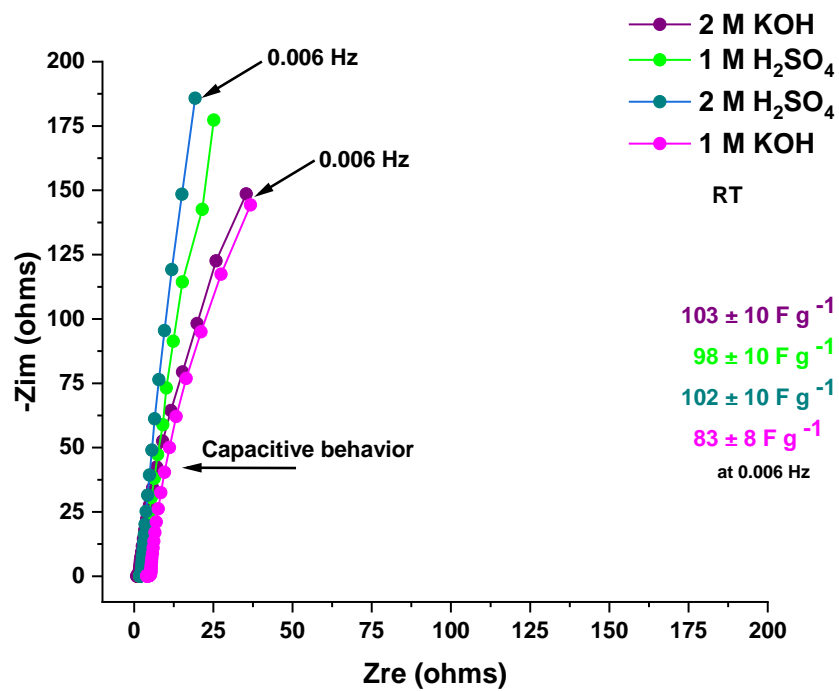

Source: author (2021-2022)

Figure 61 - Nyquist plot of ACFF-based EDLCs at room temperature and an applied potential of 0 V in glycerol-based electrolytes: KOH:GLYs with variations of molar ratios
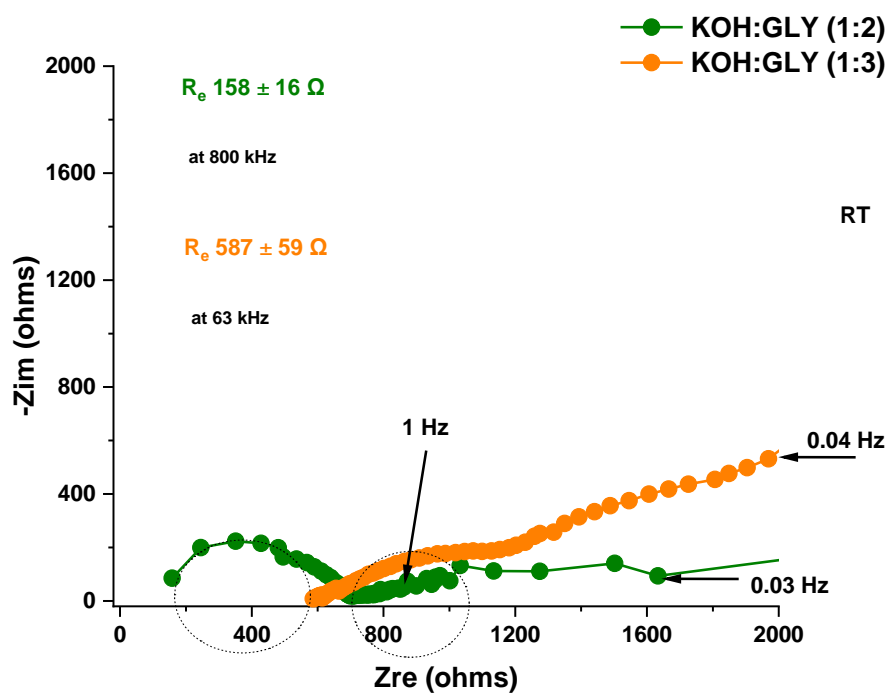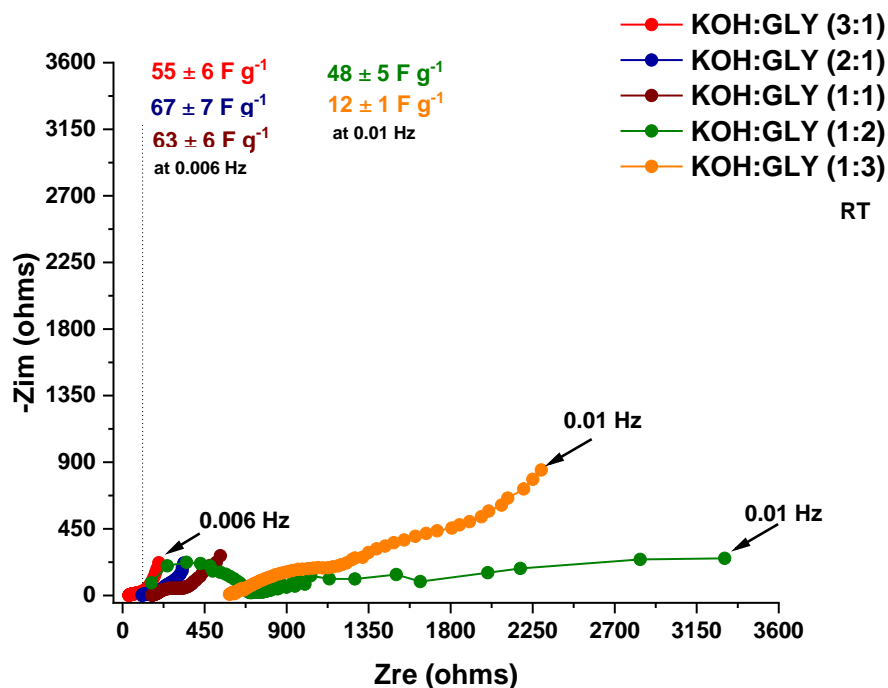

Source: author (2022)

Figure 62 - Nyquist plot of ACFF-based EDLCs at room temperature and an applied potential of 0 V in glycerol-based electrolytes: K_2CO_3:GLY (3:1) and ChCl:GLY (3:1)
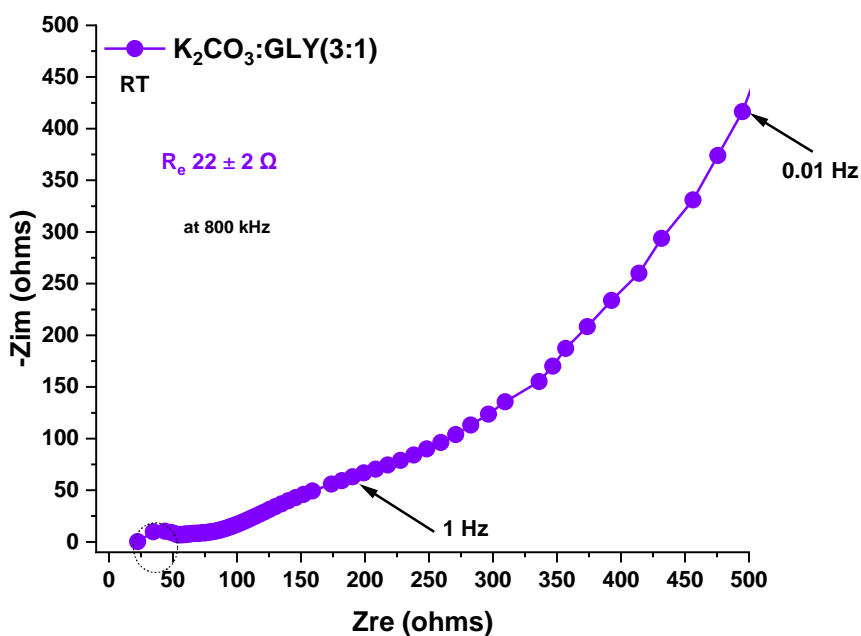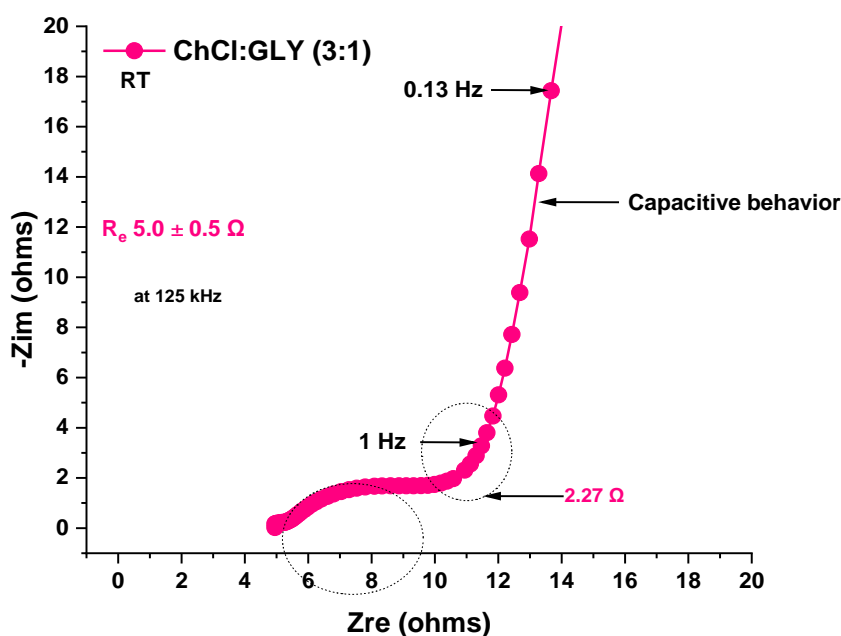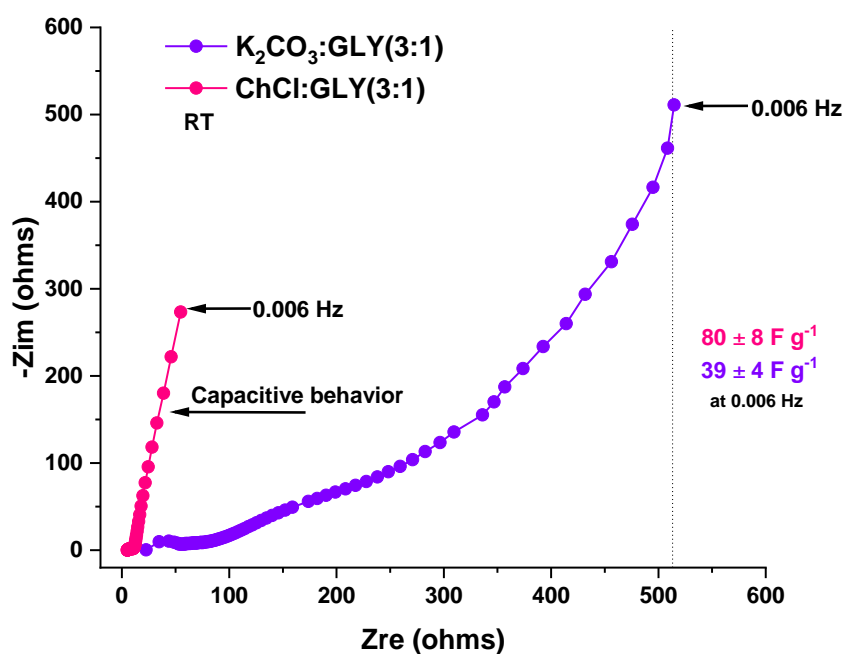

Source: author (2023)

The use of glycerol as an alternative electrolyte in supercapacitors is still very limited, and there have not been many studies in this regard, which makes it difficult to find sufficient data to compare.

The bulk electrolyte resistance (R_e) of acidic aqueous electrolytes, found in this work, outperformed the R_e of a previous study [15] about activated carbon-based electrodes derived from textile PAN-based fiber. Nevertheless, it did not outperform the R_e found in a previous study [64] about a binary composite (PPy/ACFF) and an earlier study [65] about porous carbon electrodes. The R_e found in this work is analogous to that of a study about PAN-based electrodes with enhanced surface chemistry by N-doping [63].

5.8. Electrochemical performance of ACFF-based EDLC cells: GCD plots

The GCD plots for ACFF-based EDLCs in glycerol-based electrolytes at a current density of 0.15 ± 0.02 A g^{-1} can be seen in Figures 63 - 69. The GCD plots for ACFF-based EDLCs in glycerol-based electrolytes and aqueous electrolytes at a current density of 1.0 ± 0.1 A g^{-1} can be seen in Figures 70 – 74. In addition, the parameters of the electrochemical performance of the ACFF-based EDLCs at a current density of $.15 \pm 0.02$ A g^{-1} can be seen in Tables 16 and 17, whereas at a current density of 1.0 ± 0.1 A g^{-1} can be seen in Table 18.

A linear voltage vs. time response during constant charging-discharging current is expected for carbon-based EDLCs. This linear response results in an isosceles or quasi-isosceles triangular-shaped profile and indicates a charge storage mechanism that is predominantly electrostatic (non-faradaic) [148,114]. A linear response and a triangular-shaped profile can be seen in all acidic and alkaline aqueous electrolytes (Figures 70 – 73), whereas in glycerol-based electrolytes, a linear response can be seen in KOH:GLY and ChCl:GLY both at a molar ratio of 3:1 (Figures 63, 69, and 74).

At a current density of 0.15 ± 0.02 A g^{-1} (Figure 63), the charging curve of KOH:GLY (3:1) is asymmetrical to its corresponding discharge curve due to a noticeable IR$_{drop}$ (resistance), resulting in quasi-isosceles triangular-shaped curves. At said current density, ACFF-based EDLC cell in KOH:GLY (3:1) had a Coulombic efficiency of 90%

(after 4 cycles), a capacitance of 0.13 ± 0.01 F, a gravimetric capacitance of 64 ± 6 F g^{-1}, and an internal resistance (ESR) of 70 ± 7 Ω (35 ± 3.5 Ω cm^2). As electrolyte conductivity can be affected by the salt-to-solvent ratio, glycerol-based KOH:GLY at a molar ratio of 3:1 exhibited the lowest ESR value and the highest capacitance value among KOH:GLYs (Table 16).

Figure 63 - GCD curves of ACFF-based EDLCs at room temperature and at a current density of 0.15 ± 0.02 A g^{-1} in a glycerol-based electrolyte: KOH:GLY (3:1)
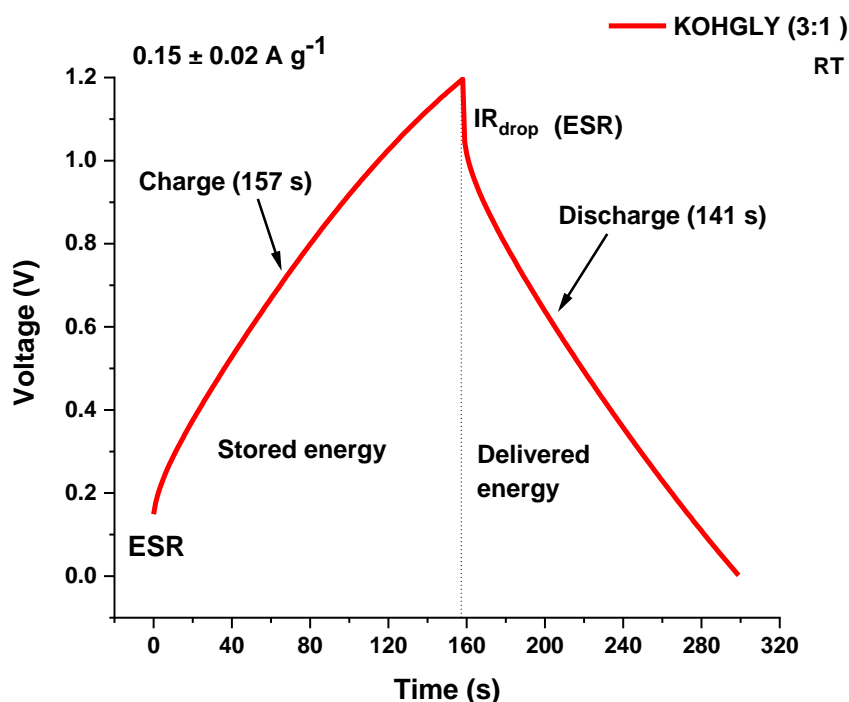
Source: author (2022)

Due to a non-linear response and a resistive rather than a capacitive behavior, the GCD curves of KOH:GLYs at molar ratios of 2:1 and 1:1 deviate from the profile expected from an ideal EDLC (Figures 64 and 65, respectively). At a current density of 0.15 ± 0.02 A g^{-1}, the charging curves of KOH:GLY (2:1) and KOH:GLY (1:1) exhibited a non-linear response reaching a plateau at high potentials possibly due to overcharge and electrolyte decomposition [149]. At molar ratios of 2:1 and 1:1, the internal resistance of both cells exceeded 150 Ω (> 75 Ω cm^2), resulting in low capacitance (< 0.1 F) and, consequently, low gravimetric capacitance (< 45 F g^{-1}). Previous studies stated that GCD provides a more consistent and reliable result for capacitance in comparison to CV [130,127].

Even though several attempts were made after reassembling the cells or acquiring a new set of electrodes, the electrochemical performance of KOH:GLY at molar ratios of 1:2 and 1:3 was found to be ineffective (Figures 66 and 67). Based on the voltammograms and on the Nyquist plots presented in the preceding sections, such behavior was expected.

Figure 64 - GCD curves of ACFF-based EDLCs at room temperature and at a current density of 0.15 ± 0.02 A g^{-1} in a glycerol-based electrolyte: KOH:GLY (2:1)

Source: author (2022)

Figure 65 - GCD curves of ACFF-based EDLCs at room temperature and at a current density of 0.15 ± 0.02 A g^{-1} in a glycerol-based electrolyte: KOH:GLY (1:1)
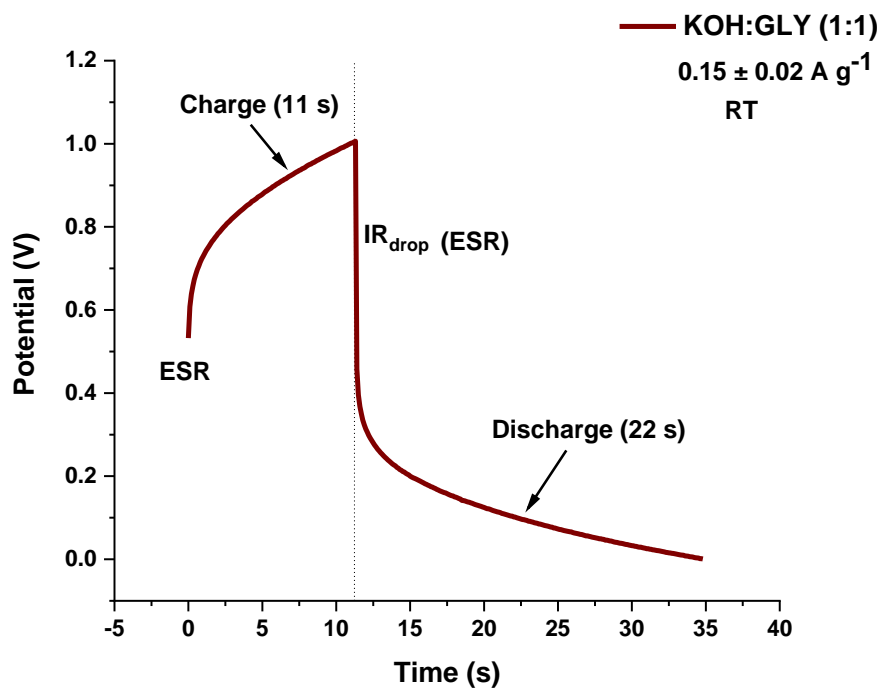
Source: author (2022)

Figure 66 - GCD curves of ACFF-based EDLCs at room temperature and at a current density of 0.15 ± 0.02 A g^{-1} in a glycerol-based electrolyte: KOH:GLY (1:2)

Source: author (2022)

Figure 67 - GCD curves of ACFF-based EDLCs at room temperature and at a current density of 0.15 ± 0.02 A g^{-1} in a glycerol-based electrolyte: KOH:GLY (1:3)

Source: author (2022)

Table 16 - Electrochemical performance of ACFF-based EDLCs in KOH:GLYs, with variation in molar ratio, at room temperature and at a current density of 0.15 ± 0.02 A g^{-1}

ACFF-based EDLCs	KOH:GLY (3:1)	KOH:GLY (2:1)	KOH:GLY (1:1)	KOH:GLY (1:2)	KOH:GLY (1:3)
ESR (Ω)	70	184	276	357	718
ESR (Ω cm^2)	35	92	138	179	359
Capacitance (F)	0.13	0.07	0.05	0.00	0.00
Gravimetric capacitance (F g^{-1})	64	42	32	0	0
Time constant (s)	9.4	13.5	13.4	0.0	0.0

Source: author (2023)

The GCD curves of K₂CO₃:GLY (3:1) exhibited a non-linear response reaching a plateau at high potentials that deviate from the profile expected from an ideal EDLC (Figure 68). At a current density of 0.15 ± 0.02 A g^{-1}, ACFF-based EDLC cell in K₂CO₃:GLY (3:1) had a Coulombic efficiency of 89% (after 4 cycles), a low gravimetric capacitance of 22 ± 2 F g^{-1}, a high internal resistance of 147 ± 15 Ω (74 ± 7 Ω cm^2), and it did not outperform KOH:GLY (3:1). According to the literature, the resistance of intra-particle pores and the bulk solution resistance of the electrolyte, as well as the resistance of the internal components of the cell have to be taken into account when referring to ESR [57,27,58]. As discussed in the preceding section, the ion diffusion into the pores and the development of the EDL in K₂CO₃:GLY (3:1) occur laboriously, resulting in high internal resistance.

Figure 68 - GCD curves of ACFF-based EDLCs at room temperature and at a current density of 0.15 ± 0.02 A g^{-1} in a glycerol-based electrolyte: K₂CO₃:GLY (3:1)
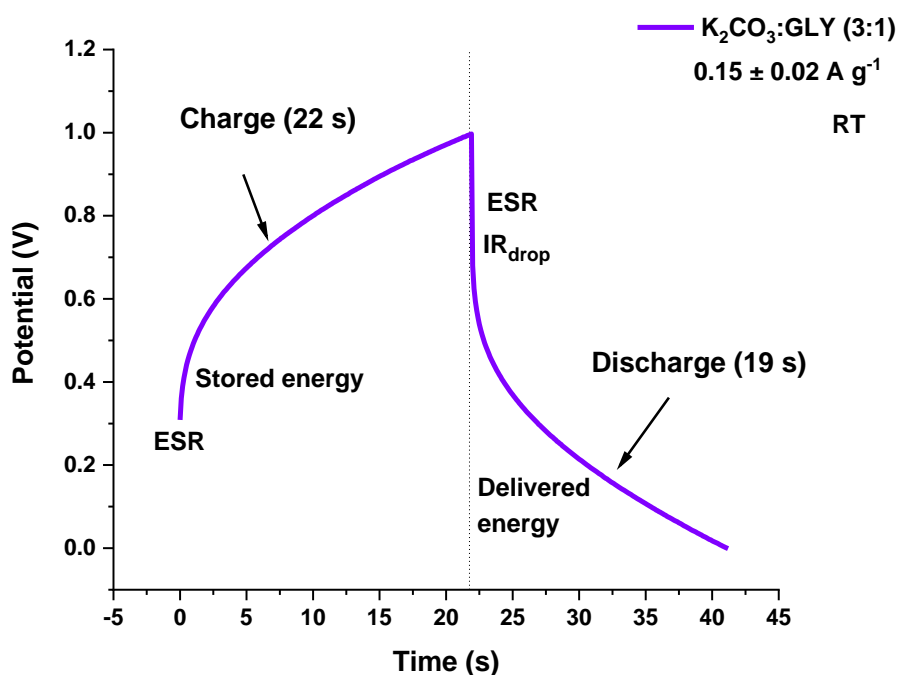
Source: author (2023)

At a current density of 0.15 ± 0.02 A g^{-1}, the GCD curves of ACFF-based EDLC in ChCl:GLY (3:1) exhibited a linear response resulting in quasi-isosceles triangular-

shaped curves (Figure 69). The discharging curve drops linearly due to a charge storage mechanism that is predominantly electrostatic. Therefore, there is no considerable contribution of pseudocapacitance [126]. At said current density, a capacitance of 0.10 ± 0.01 F, a high gravimetric capacitance of 87 ± 8 F g^{-1}, and an internal resistance of 14 ± 1 Ω (7 ± 1 Ω cm^2) were found. Among all glycerol-based electrolytes, ChCl:GLY (3:1) had the highest gravimetric capacitance value and the lowest ESR value. The results agree with the Nyquist plot present in the preceding section. Not only ChCl:GLY (3:1) had the lowest internal resistance, but also had the lowest bulk electrolyte resistance among all glycerol-based electrolytes.

Figure 69 - GCD curves of ACFF-based EDLCs at room temperature and at a current density of 0.15 ± 0.02 A g^{-1} in a glycerol-based electrolyte: ChCl:GLY (3:1)
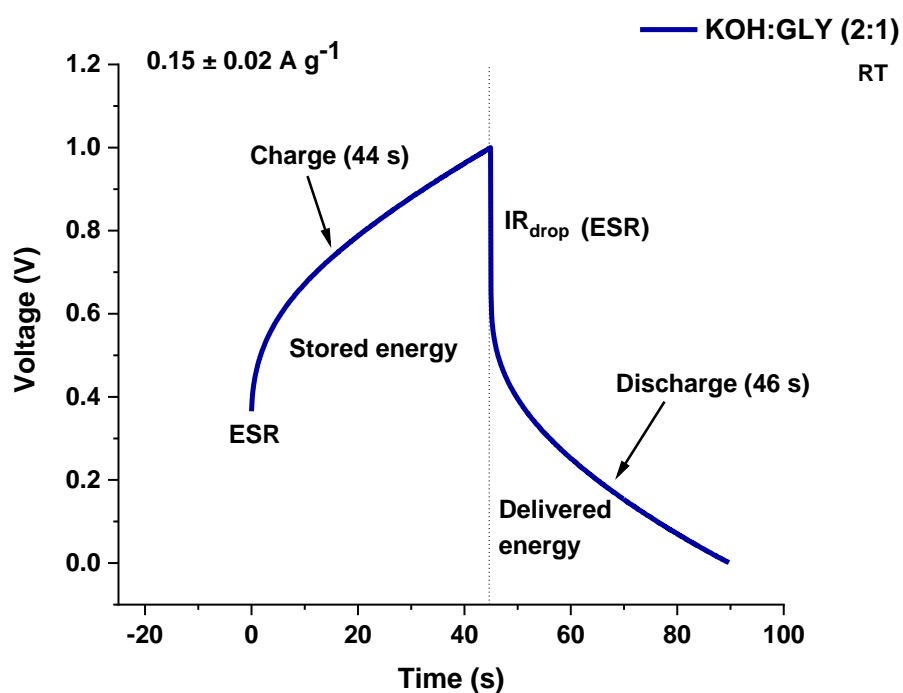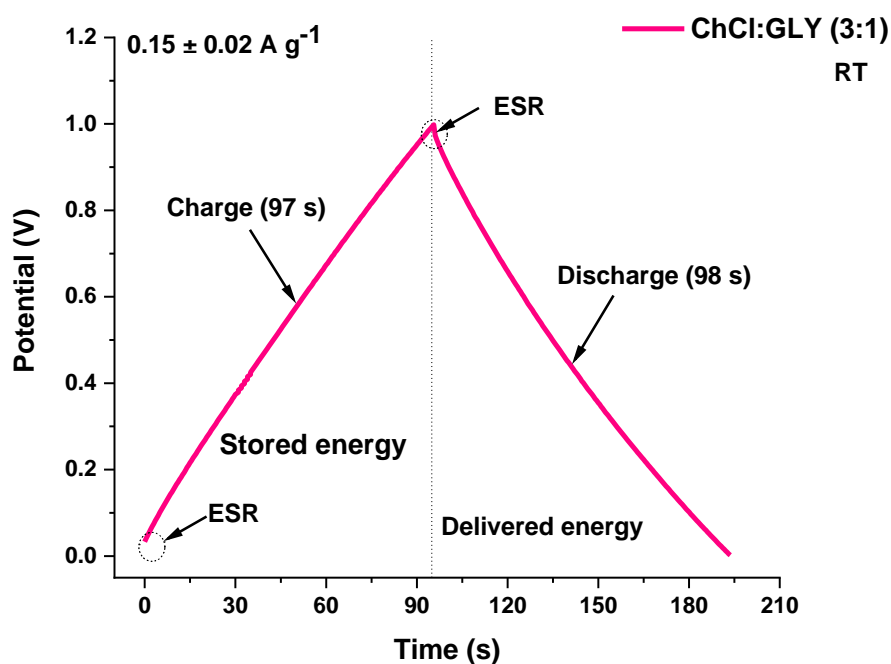

Source: author (2023)

Table 17 - Electrochemical performance of ACFF-based EDLCs in glycerol-based electrolytes (K_2CO_3:GLY and ChCl:GLY) at room temperature and at a current density of 0.15 ± 0.02 A g^{-1})

ACFF-based EDLCs	K_2CO_3:GLY (3:1)	ChCl:GLY (3:1)
ESR (Ω)	147	14
ESR (Ω cm^2)	74	7
Capacitance (F)	0.03	0.10
Gravimetric capacitance (F g^{-1})	22	87
Time constant (s)	4.0	1.4

Source: author (2023)

The internal resistance of KOH:GLY (3:1) and ChCl:GLY (3:1), investigated in this work, is lower than the internal resistance found in a study [10] about activated carbon-based electrodes in a solid polymer electrolyte plasticized with glycerol. Nevertheless, the internal resistance of glycerol-based electrolytes found in a prior study [74] on liquid-based electrolytes is much lower than the findings of this work. It should be noted that the current density (10 mA g^{-1}) used in the said study was fifteen times lower than the current density (150 mA g^{-1}) used in this work. Another study [90] carried out in anhydrous glycerol-KOH gel electrolytes for supercapacitors applications reported a gravimetric capacitance of 75 F g^{-1} at 1 A g^{-1}. Among the KOH:GLYs investigated in this work, the highest gravimetric capacitance of 64 F g^{-1} was found in KOH:GLY (3:1) at 0.15 A g^{-1}.

The occurrence of IR-drop in aqueous electrolytes is not noticeable in small current densities, such as the current density of 0.15 A g^{-1} applied in glycerol-based electrolytes. Due to the nature of aqueous electrolytes, such as high conductivity and low viscosity, larger current densities are required. As can be seen in Figures 70 -73, all aqueous-based electrolytes had a linear voltage vs. time response during the constant charging-discharging current, resulting in an isosceles or quasi-isosceles triangular-shaped profile.

At a current density of 1.0 ± 0.1 A g^{-1}, ACFF-based EDLCs in acidic aqueous electrolytes had a Coulombic efficiency of 99 – 100% (after 4 cycles), whereas, in alkaline aqueous electrolytes, a Coulombic efficiency of 96 – 98% was found. The results agree with the data presented in the preceding sections (Figures 47 and 58) since acidic aqueous electrolytes exhibited better capacitance stability. The highest capacitance of

0.18 ± 0.02 F was found in KOH 1 mol L^{-1} and the lowest capacitance of 0.15 ± 0.02 F was found in H$_2$SO$_4$ 1 mol L^{-1}. After capacitance was normalized by the active mass of both electrodes, the highest gravimetric capacitance of 117 ± 12 F g^{-1} was found in H$_2$SO$_4$ 2 mol L^{-1}, whereas the lowest gravimetric capacitance of 87 ± 8 F g^{-1} was found in KOH 1 mol L^{-1}.

The gravimetric capacitance values of 103 F g^{-1} and 87 F g^{-1} found in H$_2$SO$_4$ 1 mol L^{-1} and KOH 1 mol L^{-1}, respectively, are analogous to those of a study [70] about activated carbon-carbon nanotubes in acidic and alkaline aqueous electrolytes. The gravimetric capacitance of 117 F g^{-1} found in H$_2$SO$_4$ 2 mol L^{-1} is higher than that of a study [64] about activated carbon fiber-felt electrodes, and lower than that of a study [62] carried out in activated carbon-felt electrodes with deposition of silver nanoparticles.

A low internal resistance of 1.7 ± 0.2 Ω (0.9 ± 0.1 Ω cm^2) was found in ACFF-based EDLC in KOH 2 mol L^{-1}. The internal resistance values found in acidic aqueous electrolytes are interchangeable (Table 18). Based on the data acquired from the Nyquist plot, it was expected that KOH 1 mol L^{-1} would have inferior performance in comparison to other aqueous-based electrolytes. The charging curve of KOH 1 mol L^{-1} is asymmetrical to its corresponding discharging curve due to a noticeable ESR, resulting in an internal resistance of 9.1 ± 0.9 Ω (4.5 ± 0.5 Ω cm^2).

The internal resistance of 9.1 Ω found in KOH 1 mol L^{-1} is comparable to that of a previous study about activated carbon-based electrodes with vacuum heat treatment at 400°C and KOH 1 mol L^{-1}, although the current density used was 0.1 A g^{-1}.

Figure 70 - GCD curves of ACFF-based EDLCs at room temperature and at a current density of 1.0 ± 0.1 A g^{-1} in an acidic aqueous electrolyte: H$_2$SO$_4$ 1 mol L^{-1}.
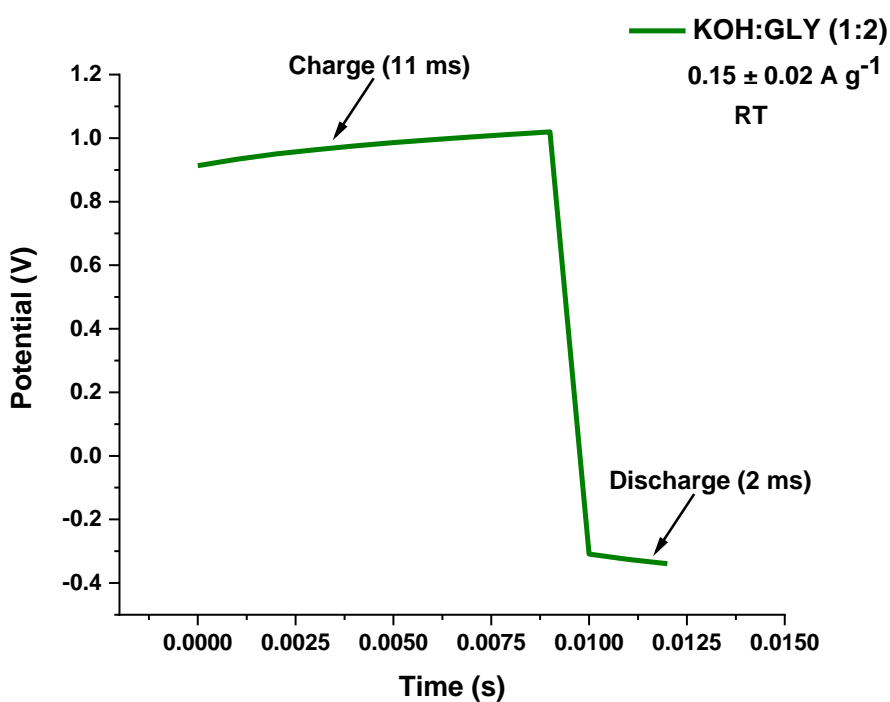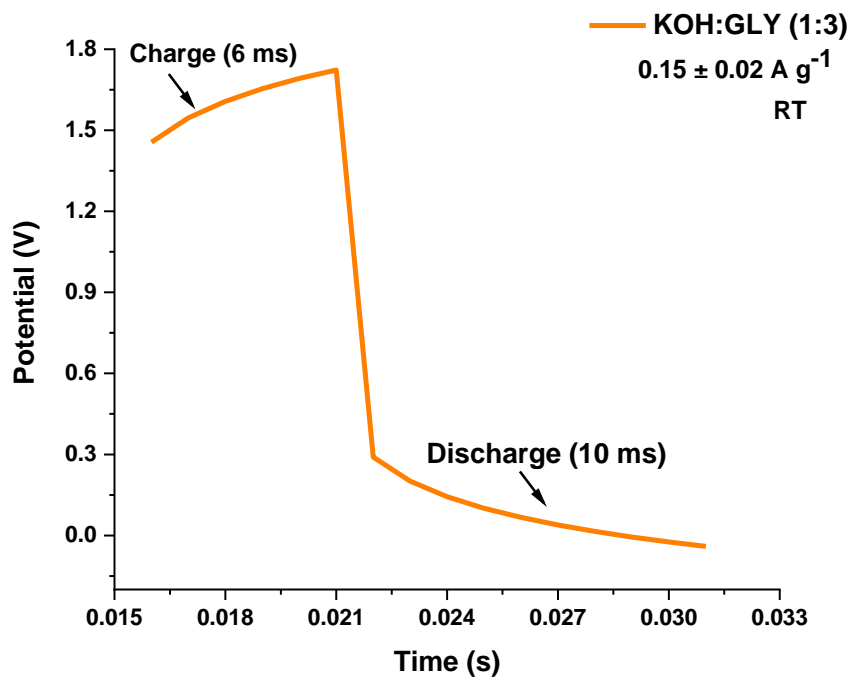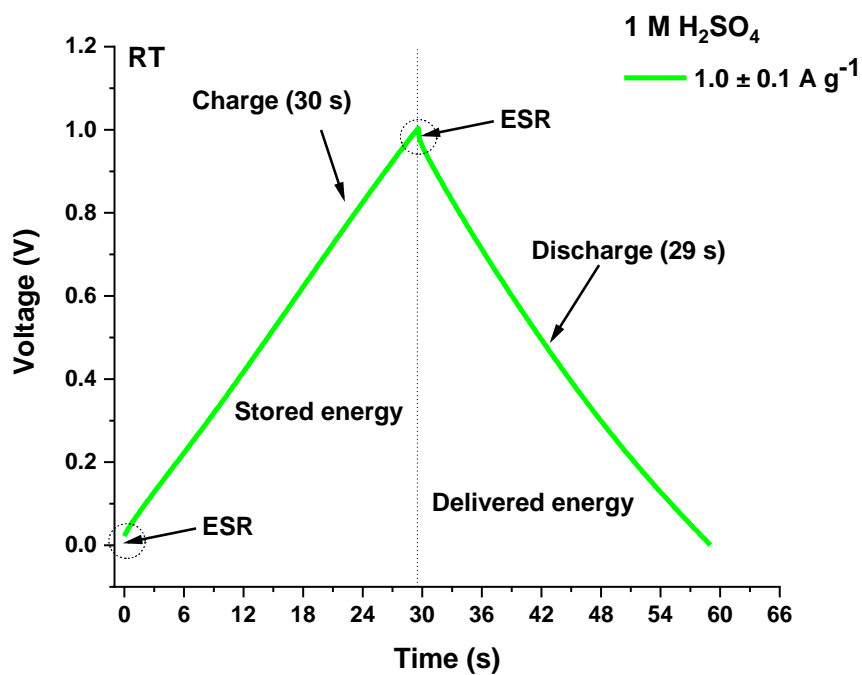

Source: author (2022)

Figure 71 - GCD curves of ACFF-based EDLCs at room temperature and at a current density of 1.0 ± 0.1 A g^{-1} in an acidic aqueous electrolyte: H$_2$SO$_4$ 2 mol L^{-1}.
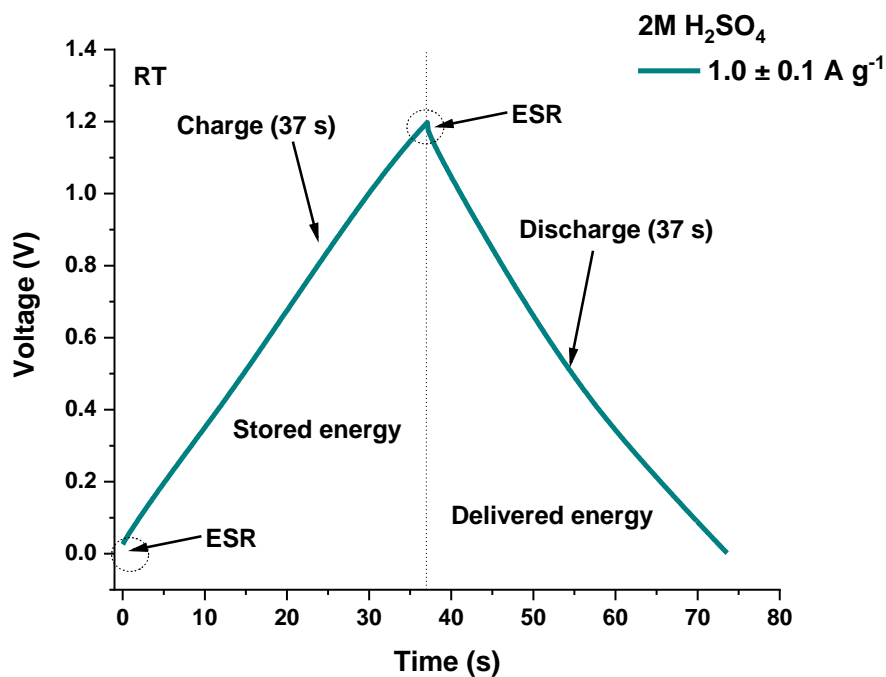
Source: author (2021)

Figure 72 - GCD curves of ACFF-based EDLCs at room temperature and at a current density of 1.0 ± 0.1 A g⁻¹ in an alkaline aqueous electrolyte: KOH 1 mol L⁻¹.
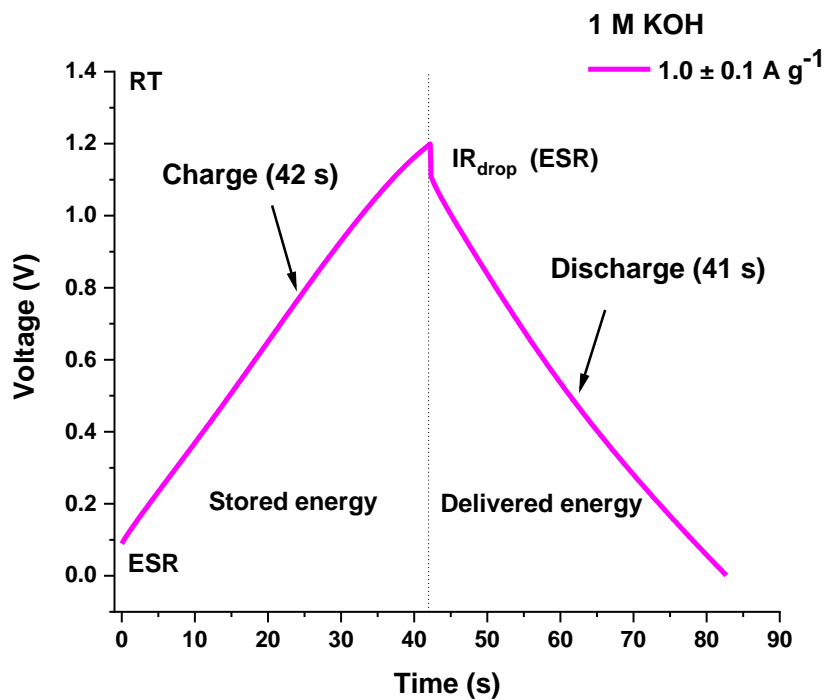
Source: author (2021)

Figure 73 - GCD curves of ACFF-based EDLCs at room temperature and at a current density of 1.0 ± 0.1 A g⁻¹ in an alkaline aqueous electrolyte: KOH 2 mol L⁻¹.
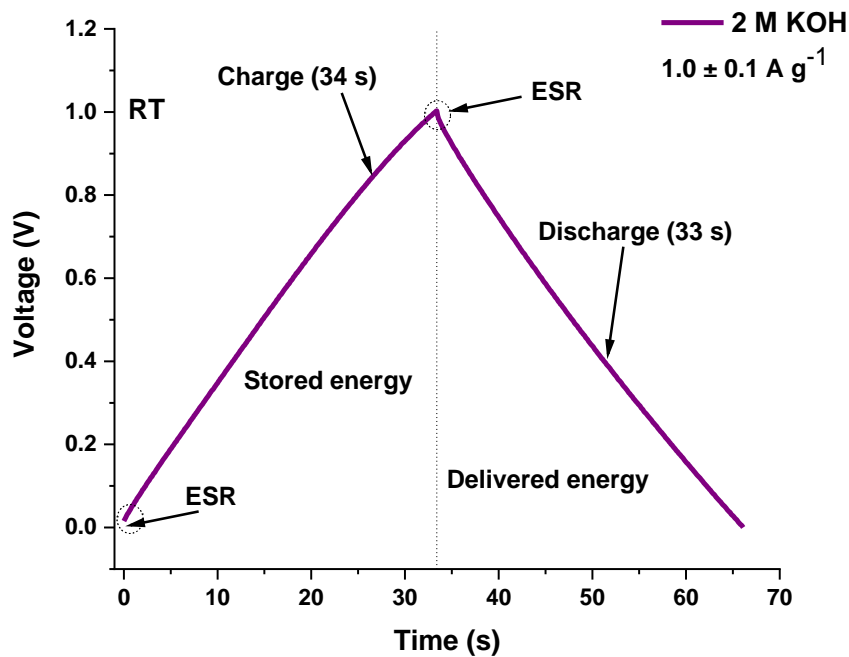
Source: author (2022)

In comparison to other glycerol-based electrolytes, ChCl:GLY (3:1) exhibited a superior electrochemical performance supporting a current density almost 7 times greater. At a current density of 1.0 ± 0.1 A g^{-1}, ACFF-based EDLCs in ChCl:GLY (3:1) had a linear response and a quasi-isosceles triangular-shaped profile (Fig 74). An internal resistance of 10.6 ± 1.1 Ω (5.3 ± 0.5 Ω cm^2), a capacitance of 0.09 ± 0.01 F, a gravimetric capacitance of 74 ± 7 F g^{-1}, and a Coulombic efficiency of 99% (after 4 cycles) were found. In comparison to KOH 1 Mol L^{-1}, the capacitance, and the gravimetric capacitance of ChCl:GLY (3:1) are 50% and 15% smaller, respectively. In terms of internal resistance, the ESR of ChCl:GLY (3:1) is higher by 16% than that of KOH 1 Mol L^{-1}.

Figure 74 - GCD curves of ACFF-based EDLCs at room temperature and at a current density of 1.0 ± 0.1 A g^{-1} in a glycerol-based electrolyte: ChCl:GLY (3:1)
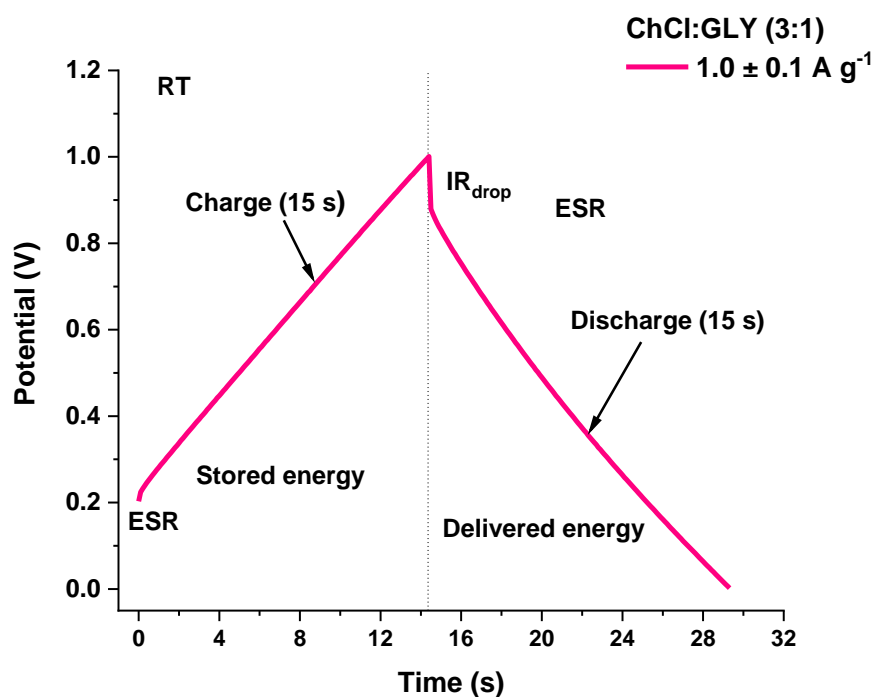
Source: author (2023)

Table 18 - Electrochemical performance of ACFF-based EDLCs in aqueous and glycerol-based
electrolytes at room temperature and at a current density of 1.0 ± 0.1 A g^{-1}

ACFF-based EDLCs	H_2SO_4 1 Mol L^{-1}	H_2SO_4 2 Mol L^{-1}	KOH 1 Mol L^{-1}	KOH 2 Mol L^{-1}	ChCl:GLY (3:1)
ESR (Ω)	2.2	2.1	9.1	1.7	10.6
ESR (Ω cm^2)	1.1	1.1	4.5	0.9	5.3
Capacitance (F)	0.15	0.16	0.18	0.17	0.09
Gravimetric capacitance (F g^{-1})	103	117	87	100	74
Time constant (s)	0.3	0.3	1.7	0.3	0.9
Coulombic efficiency (%)	100	99	96	98	99

Source: author (2023)

The product of capacitance (C) and equivalent series resistance (ESR) results in the time constant (τ) of the supercapacitor device. The smaller the time constant, the more responsive the device is. For most commercial supercapacitors, the time constant commonly ranges from 0.5 to 3.6 seconds [127]. The time constant of the two acidic aqueous electrolytes and KOH 2 Mol L^{-1} is 0.3 seconds, whereas the time constant of KOH 1 Mol L^{-1} is 1.7 seconds due to high internal resistance. Among KOH:GLYs, the lowest time constant of 9.4 seconds was found in KOH:GLY (3:1). Due to a low capacitance, a time constant of 4 seconds was found in K_2CO_3:GLY (3:1). Time constant of 1.4 seconds and 0.9 seconds were found in ChCl:GLY (3:1) at current densities of 0.15 ± 0.02 A g^{-1} and 1.0 ± 0.1 A g^{-1}, respectively.

5.9. Electrochemical performance of ACFF-based EDLC cells: Ragone plots

Due to a non-faradaic charge storage mechanism, EDLCs have limited energy density, but high-power density [41,40]. A Ragone plot of specific power density vs. specific energy density was used to evaluate the overall performance of the ACFF-based EDLC cells (Figures 75 and 76). According to the literature [128], the power density of

carbon-based EDLCs commonly ranges from 0.5 to 10 kW kg^{-1}, whereas the energy density of carbon-based EDLCs typically ranges from 1 to 10 Wh kg^{-1}. Due to high internal resistance (ESR), the specific power densities of K_2CO_3:GLY (3:1) and KOH:GLYs at molar ratios of 2:1, 1:1, 1:2, and 1:3 are less than 0.5 kW kg^{-1}. Furthermore, aqueous electrolytes with specific power densities greater than 10 kW kg^{-1} include KOH 1 mol L^{-1}, H_2SO_4 2 mol L^{-1}, and H_2SO_4 1 mol L^{-1}. None of the electrolytes had a specific energy density greater than 10 Wh kg^{-1}. Glycerol-based electrolytes with a specific energy density lower than 1 Wh kg^{-1} include K_2CO_3:GLY (3:1) and KOH:GLYs at molar ratios of 1:2, and 1:3.

H_2SO_4 2 mol L^{-1} offers the best balance between energy and power among aqueous electrolytes, with specific energy density ranging from 5.5 to 5.8 Wh kg^{-1}, and specific power density ranging from 29 to 33 kW kg^{-1}. For glycerol-based electrolytes, the best balance between energy and power was found in ChCl:GLY (3:1), with specific energy density ranging from 2.2 to 3.0 Wh kg^{-1}, and specific power density ranging from 3.9 to 5.4 kW kg^{-1}.

The time taken by a device to discharge is related to the energy-to-power ratio [150]. Supercapacitors are suitable for short-time applications, commonly in the order of seconds or minutes, as high power is delivered in a short period of time. As expected, the energy-to-power ratio of ACFF-based EDLC cells was found to be in the order of seconds (Figure 75). Batteries are an example of a device with a large energy-to-power ratio, in the order of hours.

Figure 75 - Ragone plot illustrating the performance of ACFF-based EDLC cells in aqueous and glycerol-based electrolytes at various current densities
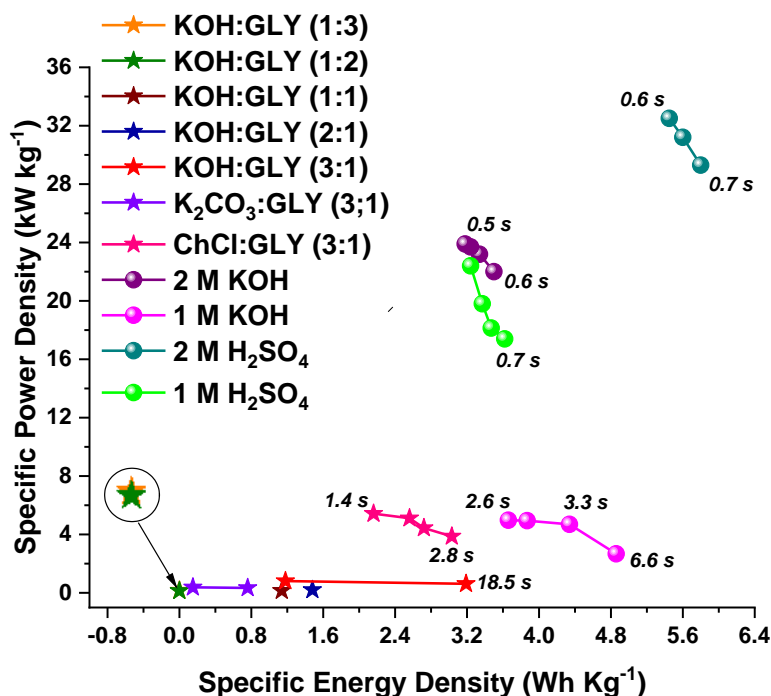
Source: author (2023)

The specific energy density and the specific power density of KOH:GLY (3:1) and ChCl:GLY (3:1), found in this work, are greater than those of a solid polymer electrolyte plasticized with glycerol for supercapacitor applications reported in an early study [10]. Another study [90] carried out in anhydrous glycerol-KOH-Mo gel electrolytes for supercapacitors applications reported a high specific energy density of 45 Wh kg^{-1}, which is significantly greater than the findings of this study. Nevertheless, anhydrous glycerol-KOH-Mo gel electrolyte provided a specific power density of 0.5 kW kg^{-1}, which was lower than the values from the glycerol-based electrolytes KOH:GLY (3:1) and ChCl:GLY (3:1).

A previous study [64] reported that the specific energy densities of ACFF-based electrodes and binary composite electrodes (PPy/ACFF) in H_2SO_4 2 Mol L^{-1} were > 15 Wh kg^{-1}, which is significantly greater than the findings of this study, whereas the specific power density found in this study is about seventy times greater.

Figure 76 - A Ragone plot illustrating the performance of ACFF-based EDLC cells and other energy storage devices.
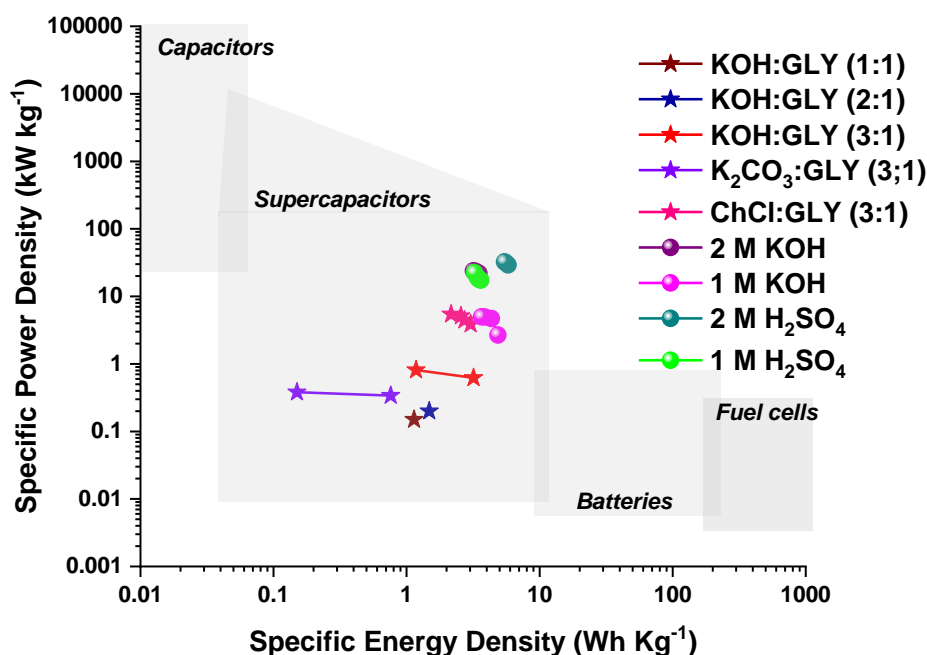
Source: author (2023)

5.10. Aqueous electrolytes and glycerol-based electrolytes: highlights

5.10.1. ACFF-based EDLC cells in acidic aqueous electrolytes

- Fast ion diffusion into the pores and fast EDL formation.
- Capacitive behavior (predominantly electrostatic).
- Absence of redox peaks.
- Low capacitance deviation in H_2SO_4 2 mol L^{-1} (CV and EIS).
- Highest gravimetric capacitance in H_2SO_4 2 mol L^{-1} (141 F g^{-1} at 1 mV s^{-1}, 102 F g^{-1} at 0.006 Hz, and 117 F g^{-1} at 1.0 A g^{-1}).
- High capacitance (0.18 - 0.19 F at 1 mV s^{-1}).
- Limited pseudocapacitance may arise from carbon-based electrodes in H_2SO_4.
- Lowest resistance of pores in H_2SO_4 2 mol L^{-1} (0.09 Ω).
- Low bulk electrolyte resistance (1.7 - 1.8 Ω).
- Low internal resistance at 1.0 A g^{-1} (2.1 - 2.2 Ω).
- Energy density is limited (< 6 Wh kg^{-1}).

- Highest specific energy density in H_2SO_4 2 mol L^{-1} (5.8 Wh kg^{-1}).
- Highest specific power density in H_2SO_4 2 mol L^{-1} (33 kW kg^{-1}).
- Best balance between energy and power in H_2SO_4 2 mol L^{-1}.
- Time constant of 0.3 seconds.
- Coulombic efficiency of 99 – 100% (after 4 cycles at 1.0 A g^{-1}).
- Cell voltage is restricted to 1.0 V due to water electrolysis.
- Low viscosity.
- High ionic conductivity.
- Hydrated ion size (< 0.38 nm).

5.10.2. ACFF-based EDLC cells in alkaline aqueous electrolytes

- Fast ion diffusion into the pores and fast EDL formation in KOH 2 mol L^{-1}.
- Capacitive behavior (predominantly electrostatic).
- Absence of redox peaks.
- Highest gravimetric capacitance in KOH 2 mol L^{-1} (129 F g^{-1} at 1 mV s^{-1}, 103 F g^{-1} at 0.006 Hz, and 100 F g^{-1} at 1.0 A g^{-1}).
- High capacitance (0.21 - 0.22 F at 1 mV s^{-1}).
- High capacitance deviation in KOH 1 mol L^{-1} (CV and EIS).
- Lowest bulk electrolyte resistance in KOH 2 mol L^{-1} (0.9 Ω).
- Highest bulk electrolyte resistance in KOH 1 mol L^{-1} (4.0 Ω).
- Highest resistance of pores in KOH 1 mol L^{-1} (0.72 Ω).
- Highest internal resistance at 1.0 A g^{-1} in KOH 1 mol L^{-1} (9.1 Ω).
- Lowest internal resistance at 1.0 A g^{-1} in KOH 2 mol L^{-1} (1.7 Ω).
- Time constant of 0.3 seconds in KOH 2 mol L^{-1}.
- Coulombic efficiency of 96 – 98% at 1.0 A g^{-1}.
- Specific energy density is limited (< 5 Wh kg^{-1}).
- Highest specific energy density in KOH 1 Mol L^{-1} (4.9 Wh kg^{-1}).
- Specific power density is limited in KOH 1 mol L^{-1} (< 5 kW kg^{-1}).
- Highest specific power density in KOH 2 mol L^{-1} (24 kW kg^{-1}).
- Cell voltage is restricted to 1.0 V due to water electrolysis.

- Electrolyte degradation occurs at 0.6 V.
- High ionic conductivity.
- Hydrated ion size (< 0.33 nm).
- Low viscosity.

5.10.3. ACFF-based EDLC cells in glycerol-based electrolytes - KOH:GLYs

- Capacitive behavior (predominantly electrostatic) at a molar ratio of 3:1.
- Faster EDL formation at a molar ratio of 3:1.
- Absence of redox peaks.
- Electrolyte degradation occurs at 1.2 V at molar ratios of 2:1 and 1:1.
- Hygroscopic.
- High viscosity (particularly at molar ratios of 3:1, 2:1, and 1;1).
- High capacitance at 1 mV s^{-1} in KOH:GLY at molar ratios of 3:1, 2:1, and 1:1 (0.17 F, 0.18 F, 0.16 F, respectively).
- Low gravimetric capacitance in KOH:GLY at molar ratios of 2:1 and 1:1 (< 45 F g^{-1} at 1.0 A g^{-1}).
- Highest gravimetric capacitance in KOH:GLY at a molar ratio of 3:1 (64 F g^{-1} at 0.15 Ag^{-1}, 82 F g^{-1} at 1 mV s^{-1}, and 55 F g^{-1} at 0.006 Hz).
- KOH:GLY at molar ratios of 1:2 and 1:3 have a more resistive behavior than capacitive.
- Lowest bulk electrolyte resistance in KOH:GLY at a molar ratio of 3:1 (35 Ω).
- Bulk electrolyte resistance in KOH:GLY at molar ratios of 2:1, 1:1, 1:2, and 1:3 exceeded 100 Ω.
- Internal resistance in KOH:GLY at molar ratios of 2:1, 1:1, 1:2, and 1:3 exceeded 150 Ω (at 0.15 A g^{-1}).
- Lowest internal resistance at 0.15 A g^{-1} in KOH:GLY at a molar ratio of 3:1 (70 Ω).
- Lowest resistance of pores in KOH:GLY at a molar ratio of 3:1.
- Best balance between energy and power in KOH:GLY at a molar ratio of 3:1.

- Best balance between capacitive and resistive behavior in KOH:GLY at a molar ratio of 3:1.

- Low specific energy density in KOH:GLY at molar ratios of 1:2 and 1:3 (< 1 Wh kg^{-1}).

- Highest specific energy density in KOH:GLY at a molar ratio of 3:1 (4.9 Wh kg^{-1}).

- Low specific power density due to high internal resistance in KOH:GLY at molar ratios of 2:1, 1:1, 1:2, and 1:3 (< 0.5 kW kg^{-1}).

- Coulombic efficiency of 90% in KOH:GLY at a molar ratio of 3:1 (after 4 cycles at 0.15 A g^{-1}).

- Lowest time constant of 9.4 seconds was found in KOH:GLY at a molar ratio of 3:1.

- Salt-to-solvent ratio influences capacitance, bulk electrolyte resistance, internal resistance, ion diffusion into the pores, and the development of the EDL.

5.10.4. ACFF-based EDLC cells in glycerol-based electrolytes - K$_2$CO$_3$:GLY at a molar ratio of 3:1

- Electrolyte degradation occurs at 1.3 V.
- Absence of redox peaks.
- Hygroscopic.
- Ion diffusion into the pores and the development of the EDL are laborious.
- Highest gravimetric capacitance (76 F g^{-1} at 1 mV s^{-1}).
- Gravimetric capacitance of 22 at 0.15 A g^{-1} and 39 at 0.006 Hz.
- Capacitance of 0.09 F at 1 mV s^{-1}.
- High resistance of pores.
- High bulk electrolyte resistance of 22 Ω (1.5 times lower than that of KOH:GLY at a molar ratio of 3:1).
- High internal resistance of 147 Ω at 0.15 A g^{-1}
- Low specific power density due to high internal resistance (< 0.5 kW kg^{-1}).

- Low specific energy density (< 1 Wh kg^{-1}).
- Coulombic efficiency of 89% (after 4 cycles at 0.15 A g^{-1}).

5.10.5. ACFF-based EDLC cells in glycerol-based electrolytes - ChCl:GLY at a molar ratio of 3:1

- Capacitive behavior (predominantly electrostatic).
- Fast ion diffusion into the pores and fast EDL formation.
- Absence of redox peaks.
- Hygroscopic.
- High gravimetric capacitance (142 F g^{-1} at 1 mV s^{-1}, 80 F g^{-1} at 0.006 Hz, 87 F g^{-1} at 0.15 A g^{-1}, and 74 F g^{-1} at 1.0 A g^{-1}).
- High capacitance (0.16 F at 1 mV s^{-1}).
- Lowest capacitance deviation among glycerol-based electrolytes (EIS).
- Lowest bulk electrolyte resistance among glycerol-based electrolytes (5.0 Ω).
- Lowest internal resistance among glycerol-based electrolytes (10.6 Ω at 1.0 A g^{-1}).
- Lowest resistance of pores among glycerol-based electrolytes.
- Time constant of 1.4 s (at 0.15 A g^{-1}) and 0.9 s (at 1.0 A g^{-1}).
- Electrolyte degradation occurs at 1.3 V.
- The most comparable performance to aqueous electrolytes among the glycerol-based electrolytes investigated in this work.
- In comparison to other glycerol-based electrolytes, it supports current density almost 7 times greater.
- Coulombic efficiency of 99% (after 4 cycles at 1.0 A g^{-1}).
- Best balance between energy and power in glycerol-based electrolytes.
- Specific energy density is limited (< 3 Wh kg^{-1}).
- Specific power density is limited (< 5.4 kW kg^{-1}).

6. CONCLUSION

This study aimed to produce and characterize binder-free electrodes derived from textile PAN-based fiber to correlate the electrode-electrolyte interface of aqueous-based and glycerol-based EDLC devices.

The production of activated carbon fiber-felt electrodes (ACFF), via physical activation with two oxidizing agents (200 sccm CO_2 + 12 ml H_2O) and 60 minutes of residence time, is relevant for supercapacitors applications as electrodes in acidic and alkaline aqueous electrolytes as well as choline chloride-glycerol hybrid electrolyte (ChCl:GLY) at a molar ratio of 3:1.

Binder-free ACFF electrodes have an average active mass and average active mass loading of 6.2 ± 0.6 mg and 12.5 ± 1.2 mg cm^{-2}, respectively. The microporosity developed particularly during the activation process contributed to a high specific surface area of 1875 m2 g^{-1}, containing 87% of the total volume of pores as micropores with a maximum pore width of 3 nm, and the size of most pores ranging from 1 to 2 nm.

Among aqueous electrolytes, H_2SO_4 2 Mol L^{-1} had the most satisfactory electrochemical performance, in terms of power and energy, followed by KOH 2 Mol L^{-1} and H_2SO_4 1 Mol L^{-1}. Although aqueous electrolytes have high conductivity and low viscosity, corrosion, and the limited cell voltage ($\sim$ 1 V) due to the narrow electrochemical stability window are drawbacks.

The process of electrolyte diffusion at room temperature developed for the cell assembly helped to decrease the viscosity and to improve the wettability of KOH:GLYs, particularly, at molar ratios of 3:1, 2:1, and 1:1. KOH:GLY at a molar ratio of 3:1 had the most acceptable performance among the other KOH:GLYs. The high bulk electrolyte resistance and high internal resistance of KOH:GLY (3:1) is a drawback since it limits power density.

It assumed that the ion diffusion into the pores and the development of the EDL in K_2CO_3:GLY (3:1) is laborious resulting in low capacitance and high internal resistance.

ChCl:GLY (3:1) has the most comparable performance to aqueous electrolytes among the glycerol-based electrolytes investigated in this work, in addition to the finest balance of power and energy among glycerol-based electrolytes. Although power density

is still limited due to high internal resistance, ChCl:GLY (3:1) is a promising glycerol-based electrolyte for supercapacitors, especially given that glycerol is a by-product of FAME biodiesel.

As glycerol-based electrolytes are non-toxic and heat-resistant, viscosity and, consequently, ion mobility and ion diffusion could be improved by heating. It is assumed that as the temperature rises, the intermolecular interactions of glycerol molecules lessen, thus decreasing viscosity and increasing conductivity.

The electrochemical performance of supercapacitors strongly relies on the electrode-electrolyte interaction and correlating the size of electrolyte ions and the pore size of carbon-based electrodes is necessary. Glycerol-based electrolytes have large molecules that are not well-fitting for the pore width of the ACFF electrode synthesized in this work. Inaccessible pores do not contribute to double-layer capacitance, and it is suggested to adapt the parameters of the physical activation process based on the size of glycerol molecules.

Although this field is still very limited and there have not been many studies in this regard, glycerol-based electrolytes are promising alternative electrolytes for supercapacitors applications.

7. SUGGESTIONS FOR FUTURE RESEARCH

Electrode materials

- For a more comprehensive quantitative analysis of surface functional groups, X-ray photoelectron spectroscopy (XPS) is recommended.
- Adjust the parameters of physical activation to acquire larger micropores.
- Pore size characterization with a CO_2 adsorption isotherm for accessing micropores smaller than 1 nm.

Electrochemical measurements

- A minor surface-redox pseudocapacitive behavior could be verified and better investigated with a three-electrode cell at a low scan rate.
- Carry out the EIS test at multiple potentials to further analyze the presence of charge transfer resistance and interfacial impedance at the current collector / active material.
- Evaluate the cycling stability of the electrode/electrolyte system, at least 10,000 cycles of charge-discharge.
- Carry out tests for glycerol-based electrolytes in a wide range of temperatures.
- Investigate another type of separator.

Electrolyte materials

- Measure the conductivity and viscosity of glycerol-based electrolytes.
- Measurements with a three-electrode setup for determining the electrochemical stability window of glycerol-based electrolytes.

REFERENCES

1. YANG, Y. et al. Application of the Supercapacitor for Energy Storage in China: Role and Strategy. **Applied Sciences**, 2021. 354-372. Disponivel em: <https://www.mdpi.com/journal/applsci>.

2. SCIBIOH, M. A.; VISWANATHAN, B. Supercapacitor: an introduction. In: M. AULICE SCIBIOH, B. V. **Materials for Supercapcitor Applications**. [S.l.]: Elsevier, 2020. Cap. 1, p. 1-13. Disponivel em: <https://doi.org/10.1016/B978-0-12-819858-2.00001-9>.

3. SHANG, W. et al. Insight into the self-discharge suppression of electrochemical capacitors: Progress and challenges. **Advanced Powder Materials**, 2, n. 1, 2023. Disponivel em: <https://doi.org/10.1016/j.apmate.2022.100075>.

4. GONZÁLEZ , A. et al. Review on supercapacitors: Technologies and materials. **Renewable and Sustainable Energy Reviews**, 58, 2016. 1190. Disponivel em: <https://doi.org/10.1016/j.rser.2015.12.249>.

5. KURZWEIL, P. Typical Applications - Electrochemical Double-layer Capacitors. In: _____ **Electrochemical Energy Storage for Renewable Sources and Grid Balancing**. [S.l.]: [s.n.], 2015. Cap. 19.1.8, p. 380-382. Disponivel em: <https://doi.org/10.1016/B978-0-444-62616-5.00019-X>.

6. REPORT LINKER. Supercapacitor Market by Type, Electrode Material, Application - Global Forecast to 2027. **Report Linker**, 2022. Disponivel em: <https://www.globenewswire.com/news-release/2022/07/08/2476465/0/en/The-global-supercapacitor-market-size-is-expected-to-grow-from-USD-472million-in-2022-to-USD-912million-by-2027-at-a-CAGR-of-14-1.html>. Acesso em: 18 mar. 2023.

7. WADHWANI, ; SAHA, P. Supercapacitor Market Size. **GMI Global Market Insights**, 2021. Disponivel em: <https://www.gminsights.com/industry-analysis/supercapacitor-market>. Acesso em: 18 mar. 2023.

8. BHAT, T. S.; PATIL, P. S.; RAKHI, R. B. Recent trends in electrolytes for supercapacitors. **Journal of Energy Storage**, 50, jun. 2022. 13.

9. VERMA, K. D. et al. Characteristics of Electrode Materials for Supercapacitors. In: _____ **Handbook of Nanocomposite Supercapacitor Materials**. Springer Series in Materials Science. ed. [S.l.]: Springer, v. 300, 2020. p. 269 -285. Disponivel em: <https://doi.org/10.1007/978-3-030-43009-2_9>.

10. SHUJAHADEEN, B. A. et al. Effect of glycerol on EDLC characteristics of chitosan:methylcellulose polymer blend electrolytes. **Journal of Materials Research and Technology**, 9, n. 4, 2020. 8355-8366.

11. MISTRY, A. et al. Quantifying Negative Effects of Carbon-binder Networks from Electrochemical Performance of Porous Li-ion Electrodes, 2021. Disponivel em: <https://www.osti.gov/pages/servlets/purl/1831722>.

12. MAMDOUH AHMED, F. et al. Overview of Different Fabric Structures. **Journal of Textiles, Coloration and Polymer Science**, 19, n. 2, 2022. 291-306. Disponivel em: <https://jtcps.journals.ekb.eg/article_253494_b839df03724d251fab28ab3add1b09a0.pdf>.

13. CHEN, J. Y. Introduction. In: CHEN, J. Y. **Activated Carbon Fiber and Textiles**. [S.l.]: [s.n.], 2017. Cap. 1, p. 4. Disponivel em: <http://dx.doi.org/10.1016/B978-0-08-100660-3.00001-8>.

14. YUE, Z.; ECONOMY,. Thermooxidative stabilization of PAN fibers. In: _____ **Activated Carbon Fiber and Textiles**. [S.l.]: [s.n.], 2017. Cap. 4.3.1, p. 64-66. Disponivel em: <http://dx.doi.org/10.1016/B978-0-08-100660-3.00004-3>.

15. MARCUZZO, J. S. et al. Microporus activated carbon fiber felt from, Brazilian textile PAN fiber: preparation, characterization and application as supercapacitor electrode. **Rev. Bras. Apl. Vac.**, Campinas, 35, n. 2, 2016. 58-63.

16. SCIBIOH, M. A.; VISWANATHAN,. Introduction - Electrolyte materials for supercapacitors. In: M. AULICE SCIBIOH, B. V. **Materials for Supercapacitor Applications**. [S.l.]: [s.n.], 2020. Cap. 4.1, p. 207-209. Disponivel em: <http://dx.doi.org/10.1016/B978-0-12-819858-2.00004-4>.

17. GONZALEZ, A. et al. Review on supercapacitors: Technologies and materials. **Renewable and Sustainable Energy Reviews**, 58, 15 jan. 2016. 1200. Disponivel em: <http://dx.doi.org/10.1016/j.rser.2015.12.249>.

18. TAER, E. et al. Investigation of H2SO4 and KOH aqueous electrolytes on the and KOH aqueous electrolytes on the from areca catechu husk. **Journal of Physics: Conference Series**, 2021. 1-2. Disponivel em: <doi:10.1088/1742-6596/1940/1/012033>.

19. LEE, J. C.; POOI, S. Electrochemical Supercapacitors: From Mechanism Understanding to Multifunctional Applications. **Advanced Energy Materials**, 11, 2021.

20. SCIBIOH, M. A.; VISWANATHAN,. Introduction - Electrolyte materials for supercapacitors. In: M. AULICE SCIBIOH, B. V. **Materials for Supercapacitor Applications**. [S.l.]: [s.n.], 2020. Cap. 4.1, p. 207 - 208. Disponivel em: <http://dx.doi.org/10.1016/B978-0-12-819858-2.00004-4>.

21. ABHIJITH, P. P. et al. Electrochemical Energy Storage Systems: The State-of-the-Art Energy Technologies. **Academic Library**, 2023. Disponivel em: <https://ebrary.net/181245/engineering/electrochemical_energy_storage_systems_state_energy_technologies#14561>. Acesso em: 2023.

22. BAGOTSKY, V. S.; SKUNDIN, A. M.; VOLFKOVICH, Y. M. EDLC ENERGY DENSITY AND POWER DENSITY. In: _____ **Electrochemical Power Sources: Batteries, Fuel Cells, and Supercapacitors**. [S.l.]: John Wiley & Sons, Inc., 2015. Cap. 27 - ELECTROCHEMICAL SUPERCAPACITORS WITH CARBON ELECTRODES, p. 267 - 271.

23. AMETA, R. K. et al. General introduction about electrochemistry and supercapacitors. In: _____ **Smart Supercapacitors:** Fundamentals, Structures, and Applications. [S.l.]: [s.n.], 2023. Cap. 1, p. 3 - 16.

24. OLABI, A. G. et al. Supercapacitors as next generation energy storage devices: Properties and applications. **Energy**, 01 mar. 2022. 8. Disponivel em: <https://doi.org/10.1016/j.energy.2022.123617>.

25. SCIBIOH, M. A.; VISWANATHAN, B. Electrolyte materials for supercapacitors. In: SCIBIOH, M. A.; VISWANATHAN, B. **Materials for Supercapacitor Applications**. [S.l.]: [s.n.], 2020. Cap. 4, p. 205-314.

26. RAJAPRIYA, A.; KEERTHANA, S.; PONPANDIAN, N. Fundamental understanding of charge storage mechanism. In: AHAMED, C. M. H. A. M. B. **Smart Supercapacitors:** Fundamentals, Structures, and Applications. [S.l.]: [s.n.], 2023. Cap. 4, p. 65-82.

27. PANDOLFO, T. et al. Capacitor Principles. In: _____ **Supercapacitors:** Materials, Systems, and Applications. 1st. ed. [S.l.]: Wiley-VCH, 2013. Cap. 2 General Properties of Electrochemical Capacitors, p. 70-71.

28. BRODD, M. W.; RALPH, J. What Are Batteries, Fuel Cells, and Supercapacitors? **Chemical Reviews**, 104, n. 10, 2004. 4245−4269.

29. PORE, O. C. et al. Review on recent progress in hydrothermally synthesized MCo2O4/rGO composite for energy storage devices. **Chemical Engineering Journal**, 2021. Disponivel em: <ttps://doi.org/10.1016/j.cej.2021.131544 >.

30. SAGADEVAN,. Charge storage mechanism in electrical dual layer condensers - Fundamental electrochemical energy storage systems. In: _____ **Advances in Supercapacitor and Supercapattery**. [S.l.]: [s.n.], 2021. Cap. 2.5, p. 31-32. Disponivel em: <https://doi.org/10.1016/B978-0-12-819897-1.00001-X>.

31. JINITHA, C. G. et al. Classification of supercapacitors. In: _____ **Smart Supercapacitors**. [S.l.]: [s.n.], 2023. Cap. 5, p. 87 - 91.

32. YU, A.; CHABOT, V.; ZHANG, J. Introduction - Fundamentals of Electrochemical Pseudocapacitors. In: AIPING YU, V. C. A. J. Z. **Electrochemical Supercapacitors for Energy Storage and Delivery - FUNDAMENTALS AND APPLICATIONS**. [S.l.]: CRS Press, 2013. Cap. 3.1, p. 99-102.

33. YANG, Y. et al. Application of the Supercapacitor for Energy Storage in China: Role and Strategy, Yanmei Xu, and Ayman Mahmoud Ahmed. **Applied Sciences**, 12, n. 1, 2022. 5. Disponivel em: <https://doi.org/10.3390/app12010354>.

34. SCIBIOH, M. A.; VISWANATHAN, B. Electrochemical double layer capacitors (EDLCs) - Fundamentals and energy storage mechanisms—overview. In: M. AULICE SCIBIOH, B. V. **Materials for Supercapacitor Applications**. [S.l.]: Elsevier, 2020. p. 18-19. Disponivel em: <https://doi.org/10.1016/B978-0-12-819858-2.00002-0>.

35. SCIBIOH, M. A.; VISWANATHAN,. Electrochemical double layer capacitors (EDLCs) - Fundamentals and energy storage mechanisms—overview. In: M. AULICE SCIBIOH, B. V. **Materials for Supercapacitor Applications**. [S.l.]: Elsevier, 2020. p. 18-19. Disponivel em: <https://doi.org/10.1016/B978-0-12-819858-2.00002-0>.

36. YU, A.; CHABOT, V.; ZHANG,. Carbon Particles and Their Associated Electrode Layers - Fundamentals of Electrochemical Double-Layer Supercapacitors. In: AIPING YU, V. C. A. J. Z. **Electrochemical Supercapacitors for Energy Storage and Delivery:** Fundamentals and Application. [S.l.]: [s.n.], 2013. Cap. 2.4.1, p. 59-60.

37. FERNANDO, J. Modeling and equivalent circuit - Electrical double-layer capacitors: Fundamentals, characteristics, and equivalent circuits. In: KULARATNA, N. **Energy Storage Devices for Electronic Systems**. [S.l.]: [s.n.], 2015. Cap. 5.6, p. 168. Disponivel em: <https://doi.org/10.1016/B978-0-12-407947-2.00005-5>.

38. BAGOTSKY, V. S.; SKUNDIN, A. M.; VOLFKOVICH, Y. M. MAIN PROPERTIES OF ELECTRIC DOUBLE-LAYER CAPACITORS (EDLC). In: BAGOTSKY, . V. S.; SKUNDIN, A. M.; VOLFKOVICH, Y. M. **Electrochemical Power Sources:** Batteries, Fuel Cells, and Supercapacitors. [S.l.]: John Wiley & Sons, Inc., 2015. p. 264 - 267.

39. OBERKLEIN, D. BACKGROUND AND THEORY OF THE ELECTRIC DOUBLE LAYER. In: OBERKLEIN, D. **Charging Kinetics of Micropores in Supercapacitors**. [S.l.]: [s.n.], 2012. Cap. 2, p. 5-10.

40. SIMON, P.; TABERNA, . P.-L.; BEGUIN, F. Electrical Double-Layer Capacitors and Carbons for EDLCs. In: _____ **Supercapacitors:** Materials, Systems, and Applications. [S.l.]: Wiley-VCH Verlag GmbH & Co., 2013. Cap. 4, p. 131 - 163.

41. SCIBIOH, M. A.; VISWANATHAN, B. Fundamentals and energy storage mechanisms—overview. In: VISWANATHAN, M. A. S. A. B. **Materials for Supercapacitor Applications**. [S.l.]: [s.n.], 2020. Cap. 2, p. 15-29.

42. MEHETRE, S. S. et al. Supercapacitors - new developments. In: AHAMED, C. M. H. A. M. B. **Smart Supercapacitors:** Fundamentals, Structures, and Applications. [S.l.]: Elsevier, 2023. p. 39-64.

43. TAER, E. et al. Investigation of H2SO4 and KOH aqueous electrolytes on the electrochemical performance of activated carbon derived from areca catechu husk. **Journal of Physics**, 2021. 8.

44. JIMÉNEZ, V.; SÁNCHEZ, P.; ROMERO, A. Materials for activated carbon fiber synthesis. In: CHEN, J. Y. **Activated Carbon Fiber and Textiles**. [S.l.]: Woodhead Publishing Series in Textiles, 2017. Cap. 2, p. 21-38.

45. MUZAFFARA, ; AHAMED, B.; HUSSAIN, C. M. Electrolyte materials for supercapacitors. In: _____ **Smart Supercapacitors**. [S.l.]: [s.n.], 2023. Cap. 11, p. 227 - 247.

46. THOMBERG, T. et al. Potassium Salts Based Non-Aqueous Electrolytes for Electrical Double Layer Capacitors: A Comparison with LiPF6 and NaPF6 Based Electrolytes. **Journal of The Electrochemical Society**, 165, 2018. A3862-A3870. Disponivel em: <https://iopscience.iop.org/article/10.1149/2.0661816jes/pdf>.

47. MANURUNG, R.; ARIEF, A.; HUTAURUK, G. R. Purification of red palm biodiesel by using K2CO3 based deep eutectic solvent (DES) with glycerol as hydrogen bond donor (HBD). **AIP Conference Proceedings**, 2018.

48. NASER, J. et al. Potassium Carbonate as a Salt for Deep Eutectic Solvents. **International Journal of Chemical Engineering and Applications**, 4, n. 3, 2013. 114 - 118.

49. FARAONE, A. et al. Glycerol Hydrogen-Bonding Network Dominates Structure and Collective Dynamics in a Deep Eutectic Solvent. **The Journal of Physical Chemistry**, 122, 2018. 1261 - 1267. Disponivel em: <https://doi.org/10.1021/acs.jpcb.7b11224>.

50. FARAONE, A. et al. Glycerol Hydrogen-Bonding Network Dominates Structure and Collective Dynamics in a Deep Eutectic Solvent. **The Journal of Physical Chemistry**, 122, 2018. 1261 - 1267. Disponivel em: <https://doi.org/10.1021/acs.jpcb.7b11224>.

51. NCBI NATIONAL CENTER FOR BIOTECHNOLOGY INFORMATION. PubChem Compound Summary for CID 6209, Choline chloride. Disponivel em: <https://pubchem.ncbi.nlm.nih.gov/compound/Choline-chloride.>. Acesso em: 15 Janeiro 2023.

52. NCBI NATIONAL CENTER FOR BIOTECHNOLOGY INFORMATION. PubChem Compound Summary for CID 11430, Potassium Carbonate. Disponivel em: <https://pubchem.ncbi.nlm.nih.gov/compound/Potassium-Carbonate.>. Acesso em: 15 Janeiro 2023.

53. NCBI NATIONAL CENTER FOR BIOTECHNOLOGY INFORMATION. PubChem Compound Summary for CID 753, Glycerol. Disponivel em: <https://pubchem.ncbi.nlm.nih.gov/compound/Glycerol.>. Acesso em: 16 Janeiro 2023.

54. ZHONG , M. et al. An alternative electrolyte of deep eutectic solvent by choline chloride and ethylene glycol for wide temperature range supercapacitors. **Journal of Power Sources**, 45, 2020.

55. XU, L. H.; AL, E. Deep eutectuc solventes as effective electrolyte from potassium iodide and ethylene glycol exhibiting redox behavior for supercapacitor application. **Journal of Energy Storage**, 48, 2022.

56. DING, W.; ET AL. Amino acids assisted to improve the voltage window of deep eutectic electrolyte formed by ethylene glycol and tetra methyl ammonium chloride. **Chemical Engineering Journal**, 457, 2023.

57. SCIBIOH, M. A.; VISWANATHAN, B. Characterization methods for supercapacitors. In: M. AULICE SCIBIOH, B. V. **Materials for Supercapacitor**

Applications. [S.l.]: [s.n.], 2020. Cap. 5, p. 338. Disponivel em: <https://doi.org/10.1016/B978-0-12-819858-2.00005-6>.

58. SCIBIOH, M. A.; VISWANATHAN, B. 2.4.8 Electric double layer in supercapacitor - Fundamentals and energy storage mechanisms—overview. In: VISWANATHAN, M. A. S. A. B. **Materials for Supercapacitor Applications**. [S.l.]: [s.n.], 2020. Cap. 2, p. 27-29.

59. ASHRITHA, ; HAREESH,. Electrode materials for EDLC and pseudocapacitors. [S.l.]: [s.n.], 2023. p. 179.

60. JIN, X. et al. On the structural evolution of textile grade polyacrylonitrile fibers during stabilization and carbonization: Towards the manufacture of low-cost carbon fiber. **Polymer Degradation and Stability**, 186, 2021. 109536.

61. MARCUZZO, J. S. et al. Microporus activated carbon fiber felt from Brazilian textile PAN fiber: preparation, characterization and application as supercapacitor electrode. **Rev. Bras. Apl. Vac**, Campinas, 35, 2016. 60.

62. RODRIGUES, A. C. et al. Ag@Activated Carbon Felt Composite as Electrode for Supercapacitors and a Study of Three Different Aqueous Electrolytes. **Materials Research**, 22, n. 1, 2019. 9.

63. RODRIGUES, A. C. et al. N-activated carbon fiber produced by oxidation process design and its application as supercapacitor electrode. **Journal of Porous Materials**, 27, 2020. 141-149.

64. MATSUSHIMA, J. T. et al. 3D-interconnected framework binary composite based on polypyrrole/textile polyacrylonitrile-derived activated carbon fiber felt as supercapacitor electrode. **Journal of Materials Science: Materials in Electronics**, 31, 2020. 10225–10233.

65. WANG, K.-P.; TENG, H. The performance of electric double layer capacitors using particulate porous carbons derived from PAN fiber and phenol-formaldehyde resin. **Carbon**, 44, 2006. 3218-3225.

66. FRANK, E.; INGILDEEV, D.; BUCHMEISER, M. R. High-performance PAN-based carbon fibers and their performance requirements. In: _____ **Structure and Properties of High-Performance Fibers**. [S.l.]: [s.n.], 2017. Cap. 2, p. 7-30.

67. ZHONG, C. et al. **Electrolytes for Electrochemical Supercapacitors**. [S.l.]: CRC Press Taylor & Francis Group, 2016.

68. SONEDA, Y. et al. Electrochemical behavior of exfoliated carbon fibers in H2SO4 electrolyte with different concentrations. **Journal of Physics and Chemistry of Solids**, 65, 2004. 219 - 222.

69. PERIASAMY, P. et al. Preparation and comparison of hybridized WO3–V2O5 nanocomposites electrochemical supercapacitor performance in KOH and H2SO4 electrolyte. **Materials Letters**, 2019. 702 - 705.

70. IBUKUN, O.; OLANIYAN, H. K. Effects of Aqueous Electrolytes in Supercapacitors. **New Physics: Sae Mulli**, 69, 2019. 154 - 158.

71. NCBI NATIONAL CENTER FOR BIOTECHNOLOGY INFORMATION. PubChem Compound Summary for CID 1118, Sulfuric Acid. Disponivel em: <https://pubchem.ncbi.nlm.nih.gov/compound/Sulfuric-Acid>. Acesso em: 15 Janeiro 2023.

72. DEPARTMENT OF CLIMATE CHANGE, ENERGY, THE ENVIRONMENT AND WATER. Sulfuric acid. **Department of Climate Change, Energy, the Environment and Water**, 2022. Disponivel em: <https://www.dcceew.gov.au/environment/protection/npi/substances/fact-sheets/sulfuric-acid>. Acesso em: 2023.

73. CRUZ, P. V. D. D. **EFEITO DO TRATAMENTO TÉRMICO A VÁCUO E DO PROCESSO HDDR NAS PROPRIEDADES ELETROQUÍMICAS DE SUPERCAPACITORES À BASE DE CARBONO ATIVADO E ÓXIDO DE GRAFENO REDUZIDO**. [S.l.]: [s.n.], 2019. 54-131 p.

74. TATEI, T. Y. **Estudo das características eletroquímicas de supercapacitores preparados com eletrólitos à base de líquido iônico (LIs) de baixo impacto ambiental**. INSTITUTO DE PESQUISAS ENERGÉTICAS E NUCLEARES IPEN-CNEN/SP. São Paulo, p. 128. 2020.

75. MEHDI, R. et al. Biomass derived activated carbon by chemical surface modification as a source of clean energy for supercapacitor application. **Fuel**, 348, 2023. 128529.

76. APPIAH, E. S. et al. Performance evaluation of waste tyre-activated carbon as a hybrid supercapacitor electrode. **supercapacitor electrode**, 89, 2022. 126476.

77. BARZEGAR, et al. Investigation of different aqueous electrolytes on he electrochemical performance of activated carbon-based supercapacitors. **RSC Advances**, 2015. 107482. Disponivel em: <www.rsc.org/advances>.

78. NCBI NATIONAL CENTER FOR BIOTECHNOLOGY INFORMATION. PubChem Compound Summary for CID 14797, Potassium Hydroxide. Disponivel em: <https://pubchem.ncbi.nlm.nih.gov/compound/Potassium-Hydroxide.>. Acesso em: 16 Janeiro 2023.

79. AMERICAN ELEMENTS. Potassium Hydroxide, 2023. Disponivel em: <https://www.americanelements.com/potassium-hydroxide-1310-58-3>. Acesso em: 2023.

80. PAGLIARO, M. Properties, Applications, History, and Market. In: PAGLIARO, M. **Glycerol - The Renewable Platform Chemical**. [S.l.]: [s.n.], 2017. Cap. Chapter 1, p. 1 - 21.

81. PNO BASED ON THE EU PROJECT GLAMOUR. **GLYCEROL TO BIOFUEL: MARKET, TECHNOLOGIES AND PLAYERS**. [S.l.], p. 1 - 46. 2020.

82. MITREA, et al. Utilization of biodiesel derived-glycerol for 1,3-PD and citric acid production. **Microbial Cell Factories**, 2017.

83. QADARIYAH, et al. Degradation of glycerol using hydrothermal process. **Bioresource Technology**, 102, n. 19, 2011. 9267-9271.

84. INTERNATIONAL LABOUR ORGANIZATION (ILO). GLYCEROL. **International Chemical Safety Cards (ICSCs)**, 2006. Disponivel em: <https://www.ilo.org/dyn/icsc/showcard.display?p_lang=en&p_card_id=0624&p_version=2>. Acesso em: 2023.

85. COJOCARU, A. et al. Electrochemical preparation of Ag nanoparticles involving choline chloride – glycerol deep eutectic solvents. **Bulgarian Chemical Communications**, 49, n. Special Issue C, 2017. 194 - 204.

86. GHAEDI, H. et al. Densities and Refractive Indices of Potassium Carbonate -Based Deep Eutectic Solvents with Dual Hydrogen Bond Donors at Several Temperatures (293.15 to 343.15 K), 2017.

87. ALBA E. DÍAZ-ÁLVAREZ, A. V. C. Glycerol: A promising Green Solvent and Reducing Agent for Glycerol: A promising Green Solvent and Reducing Agent for Nanoparticles Formation. **Applied Sciences**, 3, 2013. 55 - 69.

88. LENARDÃO, E. J. et al. Glicerol como Solvente em Síntese Orgânica. **Rev. Virtual Quim.**, 9, 2017. 192-237.

89. ADDULWAHID, R. T. E. A. Environmentally friendly plasticized electrolyte based on chitosan (CS): Potato starch (PS) polymers for EDLC applicationn: Step toward the greener energy storage devices derives from biopolymers. **Journal of Energy Storage**, 67, 2023.

90. CEVIK, et al. Bio-inspired redox mediated electrolyte for high performance flexible supercapacitor applications over broad temperature domain. **Journal of Power Sources**, 474, 2020. 228544.

91. GAJARDO-PARRA, N. F. et al. Viscosity of Choline Chloride-Based Deep Eutectic Solvents: Experiments and Modeling. **Journal of Chemical & Engineering Data**, 65, 2020. 5581--5592.

92. MAHTO, A. et al. Sustainable Water Reclamation from Different Feed Streams by Forward Osmosis Process Using Deep Eutectic Solvents as Reusable Draw Solution. **Ind. Eng. Chem. Res.**, 2017. 14623–14632.

93. INTERNATIONAL LABOUR ORGANIZATION (ILO). POTASSIUM CARBONATE (ANHYDROUS). **International Chemical Safety Cards (ICSCs)**, 2005. Disponivel em: <https://www.ilo.org/dyn/icsc/showcard.display?p_lang=en&p_card_id=1588&p_version=2>. Acesso em: 2023.

94. WEI LUN, L. et al. Alkaline deep eutectic solvent: a novel green solvent for lignocellulose pulping. **Cellulose**, 26, 2019.

95. MARCUZZO, J. S. et al. Microporus activated carbon fiber felt from Brazilian textile PAN fiber: preparation, characterization and application as supercapacitor electrode. **Rev. Bras. Apl. Vac**, Campinas, 35, 2016. 58-63.

96. AMARAL JUNIOR, M. A. et al. Production and Characterization of Activated Carbon Fiber from Textile PAN Fiber. **J. Aerosp. Technol. Manag.**, São José dos Campos, 9, n. 4, 2017. 423-430.

97. ZHANG, X. H.; LI, Q. W. Carbon fiber spinning. In: CHEN, J. Y. **Activated Carbon Fiber and Textiles**. [S.l.]: Woodhead Publishing Series in Textiles, 2017. Cap. 3, p. 39-60.

98. Z. YUE, J. E. 4.4 Carbonization process - Carbonization and activation for production of activated carbon fibers. In: CHEN, J. Y. **Activated Carbon Fiber and Textiles**. [S.l.]: [s.n.], 2017. Cap. 4, p. 78.

99. ASTM INTERNATIONAL. ASTM D2867-17 Standard Test Methods for Moisture in Activated Carbon. In: _____ **ASTM Volume 15.01:** Refractories, Activated Carbon; Advanced Ceramics. West Conshohocken: [s.n.], p. 3.

100. JOSHI, S. et al. High Surface Area Nanoporous Activated Carbons Materials from Areca catechu Nut with Excellent Iodine and Methylene Blue Adsorption. **Journal of Carbon Research**, 8, n. 1, 2022. 17.

101. NUNES, C. A.; GUERREIRO, M. C. ESTIMATION OF SURFACE AREA AND PORE VOLUME OF ACTIVATED CARBONS BY METHYLENE BLUE. **Quim. Nova**, 34, 2011. 472-476.

102. ISO INTERNATIONAL ORGANIZATION FOR STANDARDIZATION. ISO 10119:2020 Carbon fibre — Determination of density. In: _____ **59.100.20 Carbon materials**. 3. ed. [S.l.]: [s.n.], 2020. p. 13.

103. MICROMERITICS INSTRUMENT CORPORATION. **Gas Displacement Pycnometer - operator manual**. [S.l.]: [s.n.], 2016.

104. ASTM INTERNATIONAL. ASTM D3838-05(2017) Standard Test Method for pH of Activated Carbon. In: _____ **ASTM Volume 15.01:** Refractories, Activated Carbon; Advanced Ceramics. West Conshohocken: [s.n.], 2017. p. 3.

105. SPREADBURY, C.; RODRIGUEZ, R.; MAZYCK, D. Comparison Between FTIR and Boehm Titration for Activated. **Journal of Undergraduate Research**, 18, 2017. 7.

106. SCHÖNHERR, J. et al. Boehm Titration Revisited (Part I): Practical Aspects for Achieving a High Precision in Quantifying Oxygen-Containing Surface Groups on. **Journal of Carbon Research**, 4, n. 21, 06 abr. 2018. 13.

107. REN, H. et al. Surface functionality analysis by Boehm titration of graphene nanoplatelets functionalized via a solvent-free cycloaddition reaction. **Nanoscale Advances**, 18 Jan 2019.

108. GOLDSTEIN, J. I. et al. The Visibility of Features in SEM Images. In: _____ **Scanning Electron Microscopy and X-Ray Microanalysis**. 4. ed. [S.l.]: Springer, v. 8, 2018. p. 123-131. Disponivel em: <https://link.springer.com/chapter/10.1007/978-1-4939-6676-9_8>.

109. ARBIZZANI, et al. Good practice guide for papers on supercapacitors and related hybrid capacitors for the Journal of Power Sources. **Journal of Power Sources**, 450, 2020.

110. BALDUCCI, A. et al. A Guideline for Reporting Performance Metrics with Electrochemical Capacitors: From Electrode Materials to Full Devices. **Journal of The Electrochemical Society**, 164, n. 7, 2017. A1487-A1488.

111. TABERNA, P.-L.; SIMON, P. Cyclic Voltammetry. In: BÉGUIN, F.; FRACKOWIAK, E. **Supercapacitors Materials, Systems, and Applications**. [S.l.]: WILEY-VCH, 2013. Cap. 3 Electrochemical Techniques, p. 115-117.

112. KURRA, N.; JIANG, Q. Cyclic voltammetry - Electrochemical characterization techniques for Supercapacitors. In: _____ **Storing Energy with Special Reference to Renewable Energy Sources**. 2nd ed. ed. [S.l.]: Elsevier, 2022. Cap. 18 Supercapacitors, p. 401-403.

113. AULICE SCIBIOH, ; VISWANATHAN,. Cyclic voltammetry. In: AULICE SCIBIOH, . M.; VISWANATHAN, B. **Materials for Supercapacitor Applications.** [S.l.]: [s.n.], 2020. Cap. 5 Characterization methods for supercapacitors, p. 323-327.

114. MATHIS, T. S. et al. Energy Storage Data Reporting in Perspective - Guidelines for Interpreting the Performance of Electrochemical Energy Storage Systems. **Advanced Energy Materials**, 2019. 15. Disponivel em: <https://hal.science/hal-02519795v1/document>. Acesso em: mar. 2023.

115. TEVI, T. APPLICATION OF POLY (P-PHENYLENE OXIDE) AS BLOCKING LAYER TO REDUCE SELF-DISCHARGE IN SUPERCAPACITORS1. In: TEVI, T. **Enhancement of Super Enhancement of Supercapacit capacitor Ener or Energy Storage by Leakage Reduction and Electrode Modification**. [S.l.]: [s.n.], 2016. Cap. 4, p. 29-34.

116. CASTRO-GUTIÉRREZ, J.; CELZARD, A.; FIERRO, V. Energy Storage in Supercapacitors: Focus on Tannin-Derived Carbon Electrodes. **Frontiers in Materials**, 7, 2020. 25.

117. JINITHA, C. G. et al. Structure of supercapacitor. In: _____ **Smart Supercapacitors Fundamentals, Structures, and Applications**. [S.l.]: Elsevier, 2023. Cap. 5 Fundamentals of supercapacitors, p. 85-87.

118. BROUSSE, T.; BELANGER, D.; LONG, J. W. To Be or Not To Be Pseudocapacitive? **Journal of The Electrochemical Society**, 162, n. 5, 2015. A5185-A5189.

119. BAGOTSKY, V. S.; SKUNDIN, A. M.; VOLFKOVICH, Y. M. PROCESSES OF EDLC DEGRADATION (AGING). In: BAGOTSKY, V. S.; SKUNDIN, A. M.;

VOLFKOVICH, Y. M. **Electrochemical Power Sources:** Batteries, Fuel Cells, and Supercapacitors. First Edition. ed. [S.l.]: John Wiley & Sons, Inc., 2015. Cap. 27 ELECTROCHEMICAL SUPERCAPACITORS WITH CARBON ELECTRODES, p. 311-313.

120. WANG, Y.; SONG, Y.; XIA, Y. Electrochemical capacitors: mechanism, materials, systems, characterization and applications. **Chemical Society Reviews**, 45, 2016. 5925-5950. Disponivel em: <https://pubs.rsc.org/en/content/articlelanding/2016/CS/C5CS00580A>.

121. SCIBIOH, M. A.; VISWANATHAN, B. Supercapacitor impedance. In: SCIBIOH, M. A.; VISWANATHAN, B. **Materials for Supercapacitor Applications**. [S.l.]: Elsiever, 2020. Cap. 5 Characterization methods for supercapacitors , p. 336-342. Disponivel em: <https://doi.org/10.1016/B978-0-12-819858-2.00005-6>.

122. TABERNA, P.-L.; SIMON, P. 3.4.2.2 Supercapacitor Impedance - Electrochemical Techniques. In: _____ **Supercapacitor, Materials, System, and Applications**. [S.l.]: Wiley-VCH, 2013. p. 124-129.

123. BAGOTSKY, V.; SKUNDIN, A.; VOLFKOVICH, Y. IMPEDANCE OF HIGHLY DISPERSED CARBON ELECTRODES. In: _____ **Electrochemical Power Sources:** Batteries, Fuel Cells, and Supercapacitors. 1st. ed. [S.l.]: John Wiley & Sons, 2015. Cap. 27 ELECTROCHEMICAL SUPERCAPACITORS WITH CARBON ELECTRODES, p. 283-286.

124. MEI, B.-A. et al. Physical Interpretations of Nyquist Plots for EDLC Electrodes and Devices. **The Journal of Physical Chemistry**, 2018. 194-206.

125. TABERNA, P.-L.; SIMON, P. Supercapacitor Impedance. In: _____ **Supercapacitors Materials, Systems, and Applications**. [S.l.]: WILEY-VCH, 2013. Cap. 3 Electrochemical Techniques, p. 124-129.

126. FARMA, R. et al. Physical and Electrochemical Properties of Supercapacitor Electrodes Derived from Carbon Nanotube and Biomass Carbon. **Int. J. Electrochem. Sci.**, 8, 2013. 257 - 273.

127. ZHANG, S.; PAN, N. Supercapacitors Performance Evaluation. **Adv. Energy Mater.**, 5, 2015.

128. PANDOLFO, T. et al. General Properties of Electrochemical Capacitors. In: BEGUIN, F.; FRACKOWIAK, E. **Supercapacitor:** Materials, System, and Applications. [S.l.]: WILEY-VCH, 2013. Cap. 2, p. 69 - 86.

129. SCIBIOH, M. A.; VISWANATHAN,. Galvanostatic cycling - Transient techniques. In: SCIBIOH, M. A.; VISWANATHAN, B. **Materials for Supercapacitor Applications**. [S.l.]: [s.n.], 2020. Cap. 5 Characterization methods for supercapacitors, p. 327 - 330.

130. MUZZAFFAR, A.; AHAMED, M. B.; HUSSAIN, C. M. Testing and measurement techniques for supercapacitors. In: _____ **Smart Supercapacitors Fundamentals, Structures, and Applications**. [S.l.]: [s.n.], 2023. p. 667.

131 YUE, Z.; ECONOMY, J. 4.5.1.3 Development of porosity - Carbonization and activation for production of activated carbon fibers. In: CHEN, J. Y. **Activated Carbon Fiber and Textiles**. [S.l.]: Woodhead Publishing Series in Textiles, 2017. Cap. 4, p. 89-94.

132 MARSH , H.; RODRIGUEZ-REINOSO, F. Characterization of Activated Carbon. In: MARSH, H.; RODRIGUEZ-REINOSO, F. **Activated Carbon**. [S.l.]: [s.n.], 2006. Cap. 4, p. 143 - 236.

133 ENTEGRIS POCO MATERIALS. **Graphite Properties and Characteristics For Industrial Applications**. Decatur, Texas, p. 42.

134 LEITE, B. M. **ADSORÇÃO DE PARACETAMOL E ÁCIDO ACETILSALICILICO EM FIBRAS DE CARBONO ATIVADA E CARVÕES ATIVADOS.** UNIVERSIDADE ESTADUAL DE MARINGÁ. Maringá, p. 128. 2018.

135 DONOHUE, M. D.; ARANOVICH, G. L. Classification of Gibbs adsorption isotherms. **Advances in Colloid and Interface Science**, 76-77, 01 jul. 1998. 137-152.

136 CHANG, S.-S. et al. Mesoporosity as a new parameter for understanding tension. **Journal of Experimental Botany**, 60, n. 11, 12 maio 2009. 3023–3030.

137 GLEYSTEEN, L. F.; DEITZ, V. R. HYSTERESIS IN THE PHYSICAL ADSORPTION OF NITROGEN ON BONE CHAR AND OTHER ADSORBENTS. **Journal of Research of the National Bureau of Standards**, 35, out. 1945. 23.

138 LAHRAR, E. H.; SIMON, P.; MERLET, C. Carbon-carbon supercapacitors: Beyond the average pore size or how electrolyte confinement and inaccessible pores affect the capacitance. **Journal of Chemical Physics**, 2021. Disponivel em: <https://hal.science/hal-03388764v1/file/Lahrar21b-accepted.pdf>.

139 KURZWEIL, P. 19.1.2.1.3 Pore Geometry - Electrochemical Double-layer Capacitors. In: _____ **Electrochemical Energy Storage for Renewable Sources and Grid Balancing**. [S.l.]: Elsevier, 2015. Cap. 19, p. 352.

140 KURZWEIL, P. 19.1.2.3.4.2 Diffusion Impedance - Electrochemical Double-layer Capacitors. In: GARCHE, P. T. M. A. J. **Electrochemical Energy Storage for Renewable Sources and Grid Balancing**. [S.l.]: [s.n.], 2015. Cap. 19, p. 357.

141 EDANA, THE VOICE OF NONWOVENS. **Glossary Nonwovens Terms**. [S.l.]: [s.n.], 52 p. Disponivel em: <https://www.edana.org/docs/default-source/edana-nonwovens/glossary---nonwovens-terms.pdf?sfvrsn=897dda16_2>. Acesso em: 27 fev. 2023.

142 MICROSCOPY AUSTRALIA. Scanning Electron Microscopy. In: _____ **MYSCOPE Microscopy Training**. [S.l.]: [s.n.], p. 57. Disponivel em: <https://myscope.training/pdf/MyScope_SEM.pdf >.

143 FARNSWORTH , ; CHIRIMA, G.; YU , F. Raman Spectroscopy: A Key Technique in Investigating Carbon-Based Materials. **Spectroscopy**, 36, n. 8, ago. 2021. 9-14.

Disponivel em: <https://www.spectroscopyonline.com/view/raman-spectroscopy-a-key-technique-in-investigating-carbon-based-materials>. Acesso em: mar. 2023.

144. KURZWEIL, P. Electrolyte Solution - Electrochemical Double-layer Capacitors. In: _____ **Electrochemical Energy Storage for Renewable Sources and Grid Balancing.** [S.l.]: [s.n.], 2015. Cap. 19.1.5 , p. 372-374. Disponivel em: <http://dx.doi.org/10.1016/B978-0-444-62616-5.00019-X>.

145. SCIBIOH, M. A.; VISWANATHAN, B. Cyclic Voltammetry. In: SCIBIOH, M. A.; VISWANATHAN, B. **Materials for Supercapacitor Applications**. [S.l.]: Elsevier, 2020. Cap. 5 Characterization Methods for Supercapacitors, p. 323-327.

146. SCIBIOH, M. A.; VISWANATHAN, B. Pseudocapacitance - Fundamentals and Energy Storage Mechanisms - Overview. In: SCIBIOH, M. A.; VISWANATHAN, B. **Materials for Supercapacitors Applications**. [S.l.]: Elsevier, 2020. p. 29-30.

147. ELGRISHI, N. et al. A Practical Beginner's Guide to Cyclic Voltammetry. **Journal of chemical education**, 3 nov. 2017. 10.

148. ZAPATA-BENABITHEA, Z. et al. Activated Carbon Bio-Xerogels as Electrodes for Super Capacitors Applications. **Procedia Engineering**, 148, 2016. 18 - 24.

149. CASTRO-GUTIÉRREZ, J.; CELZARD, A.; FIERRO, V. Energy Storage in Supercapacitors: Focus on Tannin-Derived Carbon Electrodes. **Frontier in Materials**, Epinal, France, 7, 2020. Disponivel em: <https://doi.org/10.3389/fmats.2020.00217>.

150. CATENARO, E.; RIZZO , D. M.; ONORI, S. Experimental analysis and analytical modeling of Enhanced-Ragone plot. **Applied Energy**, 2021. 116473.

Journal article

1. Belineli Barbosa, I.A., Marcuzzo, J.S., Cosentino, I.C. et al. **Binder-Free Textile PAN-Based Electrodes for Aqueous and Glycerol-Based Electrochemical Supercapacitors.** Waste Biomass Valor (2023). https://doi.org/10.1007/s12649-023-02208-2.

2. Barbosa, I. A. B., Bernardi, H. H., & Menezes, W. M. M. (2018). **Characterization of a welding wire by rotating beam fatigue test.** Revista Brasileira de Aplicações de Vácuo, 37 (1), 28. https://doi.org/10.17563/rbav.v37i1.1093.

3. Santos, R. D. S., Barbosa, I. A. B., Menezes, W. M. M., & Bernardi, H. H. (2017). **Processamento e caracterização de um compósito granular obtido por reciclagem mecânica.** Revista Brasileira de Aplicações de Vácuo, 36 (1), 27. DOI: 10.17563/rbav.v36i1.1060

Book

1. Belineli Barbosa, I. A., Bernardi, H. H., & Muniz Menezes, W. M. (Eds.). (2019). **Caracterização em fadiga por flexão rotativa de fios de arame de solda** [E-book]. In As Engenharias frente à Sociedade, a Economia e o Meio Ambiente 3 (Vol. 3, pp. 71–79). Atena Editora. https://doi.org/10.22533/at.ed.3201925066.

Conference Poster

1. Belineli Barbosa, I.A., Marcuzzo, S. J., F. (2022). **Effect of carbonization tension on the properties of textile PAN-based carbon fibers.** 24° CBECIMAT - Águas de Lindóia - SP – Brasil (2022).

2. Belineli Barbosa, I.A., Marcuzzo, S. J., Faria Jr, R.N. (2022**). Influence of aqueous and glycerol-based electrolytes on the performance of activated carbon fiber-felt electrodes for supercapacitors.** 24° CBECIMAT - Águas de Lindóia - SP – Brasil (2022).

Conference Paper

1. Belineli Barbosa, I. A., Bernardi, H. H., Polidoro, H. A., Faria Jr., R. N., & Saldanha Marcuzzo, J. (Eds.). (2021). **Caracterização analítica clássica na produção de carvão ativado a partir da casca de castanha de caju**. (vol. 1). https://carbono2021.com/wp-content/uploads/2021/12/Anais-Carbono-2021.pdf

2. Santos, R.S.; Belineli Barbosa, I. A., Bernardi, H. H., & Menezes, W. M. M. (Eds.). (2018). **Avaliação mecânica e microestrutural de um cabo de aço submetido a carregamentos cíclicos rotativos** https://www.metallum.com.br/23cbecimat/.

3. Belineli Barbosa, I. A., Bernardi, H. H., & Menezes, W. M. M. (Eds.). (2017). **Caracterização em fadiga por flexão rotativa de fios de arame de solda**. http://www.cimatech.com.br/.

4. Barbosa, I. A. B., Bernardi, H. H., & Menezes, W. M. M. (Eds.). (2016). **Processamento e caracterização de um compósito granular obtido por reciclagem mecânica**. http://www.cimatech.com.br/.